Thesis presented to the Instituto Tecnológico de Aeronáutica, in partial fulfillment of the requirements for the degree of Doctor of Science in the Graduate Program of Physics, Field of Nonlinear Dynamics and Complex Systems.

Leonardo Fabrício Gomes Batista

MULTIFRACTAL ANALYSIS OF MAGNETIC FIELDS IN THE SOLAR WIND AND SOLAR PHOTOSPHERE

Thesis approved in its final version by signatories below:

Documento assinado digitalmente
ERICO LUIZ REMPEL
Data: 18/08/2023 09:54:57-0300
Verifique em https://validar.iti.gov.br

Prof. Dr. Erico Luiz Rempel

Advisor

Prof. Dr. Emília Villani

Pro-Rector of Graduate Courses

Campo Montenegro
São José dos Campos, SP - Brazil
2023

BIBLIOGRAPHIC REFERENCE

CESSION OF RIGHTS

MULTIFRACTAL ANALYSIS OF MAGNETIC FIELDS IN THE SOLAR WIND AND SOLAR PHOTOSPHERE

Leonardo Fabrício Gomes Batista

Thesis Committee Composition:

Prof. Dr.	Manuel Máximo Bastos Malheiro Oliveira	Chairperson	-	ITA
Prof. Dr.	Erico Luiz Rempel	Advisor	-	ITA
Prof. Dr.	Marco Antonio Ridenti	Internal Examiner	-	ITA
Dr.	Luis Eduardo Antunes Vieira	External Examiner	-	INPE
Dr.	Reinaldo Roberto Rosa	External Examiner	-	INPE
Dr.	Rodrigo Andrés Miranda Cerda	External Examiner	-	UNB

ITA

To my parents Batista and Regina; my wife Talita; my brother Carlos and Esu for the unconditional love and support.

Acknowledgments

First, I would like to thank God for this new opportunity to return to Physics.

I am grateful for all unconditional love and support from my father Jose Batista, my mother Regina Gomes, my wife Talita Reis and my brother Carlos Leandro.

I am deeply grateful to my supervisor, Prof. Dr. Erico Luiz Rempel for believing in my ability to work and develop this research. I am also thankful for all patience a support over these four years.

I would like to thank Prof. Dr. Silvio Gama and Dr. Tiago Gomes for the support and contribution to produce an excellent paper. I also thank the Prof. Dr. Daniel Brito de Freitas, for the first opportunity you gave me in such hard times giving me the initial background to be a scientist.

I would like to thank the members of the Nonlinear Dynamics and Complex Systems research group: Prof. Dr. Erico Luiz Rempel, Prof. Dr. Suzana de Souza, Dr. Dalton Nunes, Dr. Tiago Gomes and Prof. Dr. Francis Franco for all important contributions and suggestions to my academic development. I also thank the Dr. Breno Raphaldini, for all support and cooperation to this present and forthcoming work.

A sincere thank you to all professors of the ITA graduate program in Physics and to the graduate office. I am grateful to ITA and CAPES funding for giving me the assist and opportunity to work in an environment of excellence.

A special thanks to all my work colleagues in these four years at DCTA for all support, conversations and coffee.

At last, I would like to thank Talita for all the love, care, and support during those tough years. You always believed in me and held my hand. You are my best friend. *Te Amo.*

"Kawó-Kabiesilé"

Orí eni ní um'ni j'oba.
The spirit of a man makes him a king.
YORUBA PROVERB

Resumo

In this work, we investigate the role of coherent structures in solar wind and solar photospheric turbulence through the multifractal perspective. By using the multifractal detrended fluctuation analysis method coupled with the volatility of the time series, two solar wind magnetic field time series are investigated, one with current sheets and one without current sheets. As expected, a stronger level of multifractality is found in the volatility of the series containing currents sheets when compared to the one without current sheets. To know the origin of the multifractal behavior, the surrogate method is applied to all time series. The results for the magnetic field time series reveal a major contribution from a heavy-tail distribution to the multifractality of the series with currents sheets but a stronger influence of long-range correlations for the series without current sheets. In the context of the photosphere, we propose a new multifractal analysis methodology for intense active regions. The results confirm the rise of multifractality following the growth and evolution of the active region. In addition, Lagrangian objective vortices were also detected at the photosphere, which are directly related to twisting and energy injection in the magnetic field, leading to intense solar flares.

Abstract

In this work, we investigate the role of coherent structures in solar wind and solar photospheric turbulence through the multifractal perspective. By using the multifractal detrended fluctuation analysis method coupled with the volatility of the time series, two solar wind magnetic field time series are investigated, one with current sheets and one without current sheets. As expected, a stronger level of multifractality is found in the volatility of the series containing currents sheets when compared to the one without current sheets. To know the origin of the multifractal behavior, the surrogate method is applied to all time series. The results for the magnetic field time series reveal a major contribution from a heavy-tail distribution to the multifractality of the series with currents sheets but a stronger influence of long-range correlations for the series without current sheets. In the context of the photosphere, we propose a new multifractal analysis methodology for intense active regions. The results confirm the rise of multifractality following the growth and evolution of the active region. In addition, Lagrangian objective vortices were also detected at the photosphere, which are directly related to twisting and energy injection in the magnetic field, leading to intense solar flares.

List of Figures

List of Tables

List of Abbreviations and Acronyms

AR	Active Region
BDMA	Backward Movinf Average
CDMA	Centered Moving Average
CME	Coronal Mass Ejections
CS	Current Sheet
DFA	Detrended Fluctuation Analysis
DMA	Detrended Moving Average
EFR	Emerging Flux Region
fBm	fractional Brownian motion
fGn	fractional Gaussian noise
FDMA	Forward Moving Average
FGM	Fluxgate Magnetometer
HMI	Helioseismic and Magnetic Imager
K41	Kolmogorov 1941
IACD	Integrated Average Current Deviation
IK	Iroshnikov-Kraichnan
LAVD	Lagrangian Averaged Vorticity Deviation
MF-DFA	Multifractal Detrended Fluctuation Analysis
MF-DMA	Multifractal Detrended Moving Average
MHD	Magnetohydrodynamics
PDF	Probability Density Function
PSD	Power Spectrum Density
SDO	Solar Dynamics Observatory
SHARP	Space-Weather Helioseismic and Magnetic Imager Active Region Patches
UTC	Coordinated Universal Time
WTMM	Wavelet Transform Modulus Maxima

Contents

1 Introduction

The Sun has a wide range of dynamical processes involving turbulence in surface convection and large scale flows, all coupled to an intense magnetic activity. This complex system of solar plasma events extends into the interplanetary medium and is far from any concept of equilibrium or stability. Turbulence is the cornerstone in this dynamical system, being associated with events like coronal mas ejections, solar flares or geomagnetic storms. So, finding a methodology to describe and quantify these events is the key to understand the phenomenology of solar plasma turbulence.

Among the most versatile methods to understand the coherent structures present in this complex system are the ones based on a fractal perspective. By considering the data obtained from these dynamical systems, e.g., solar wind magnetic field measurements, it is possible to detect the behavior of scaling laws related to possible self-similarities intrinsic to these nonlinear time series. Due to the evolution of this kind of analysis it was possible to extrapolate its application to two-dimensional observational data, e.g., spatiotemporal series of photospheric images. Developing a solid fractal methodology for both the solar wind and photospheric complex systems can strongly impact the understanding of how the solar dynamics works and, hence, how it affects the Earth's atmosphere. This is the goal of the present thesis, which is described in more details in the following sections. In particular, we focus on the study of coherent structures present in the plasma turbulence and their role on the behavior of the multifractal indices.

Fractals have been widely employed in nonlinear analysis along the past decades as a form of representing the complex topological structures produced by dynamical systems. These topological structures are subsets of the phase space that may represent chaotic attractors, stable or unstable manifolds, boundaries between basins of attraction, etc. Thus, when dynamical systems are investigated through nonlinear time series or spatiotemporal series analysis, the fractal indices computed from the data series somehow represent the complexity of the structure of an underlying set on which the solution lies. Additionally, the dynamical structure could be represented either by a monofractal or a multifractal process. A monofractal process has a scaling law for a fluctuation function which is a linear function of statistical moments with a single scaling exponent. A multifractal process has a power-law scaling which is a nonlinear function of statistical moments with a

range of scaling exponents (SALAT *et al.*, 2017). A monofractal scaling is to be expected from dynamical processes behind perfectly self-similar fractal sets, like deterministically generated Cantor sets (CANTOR, 1883), or even from white noise time series (IHLEN, 2012); multifractals, on the other hand, are observed in inhomogeneous systems, such as strongly intermittent turbulence, where the presence of strong fluctuations related to coherent structures localized in space generate a departure from Gaussianity in probability distribution functions (PDFs) of small-scale structure functions (CARBONE *et al.*, 2004b), as seen in several analyses of observational magnetohydrodynamic data (see, e.g., (MARSCH; TU, 1998), (BURLAGA, 2001), and (BRUNO, 2019) for reviews on turbulence, intermittency and multifractal scalings in the solar wind).

1.1 Multifractal Analysis of Solar Wind

A series of more recent works have confirmed the multifractal nature of the solar wind fluctuations. MACEK (2007) employed Voyager magnetic field data in the outer heliosphere and Helios plasma data in the inner heliosphere to show that multifractal spectra of intermittent solar wind fluctuations are consistent with that of the generalized two-scale weighted Cantor set. BOLZAN; ROSA (2012) analyzed magnetic field data from the ACE satellite and conjectured that the presence of large scale coherent structures during coronal mass ejections (CME) decreases the multifractality, when compared with periods after the CME events. The interaction of the solar wind with the Earth's magnetosphere also contributes for multifractality in measurements of the geomagnetic activity, such as the geomagnetic induced current WIRSING; MILI (2020) and the Dst index OGUNJO *et al.* (2021), although internal sources of multifractality must also be considered, as GOPINATH (2016) suggested that multifractality of the auroral electrojet index is fairly independent of the solar activity cycle. WAWRZASZEK *et al.* (2019) characterized multifractality in intermittent turbulence of heliospheric magnetic field fluctuations from Ulysses spacecraft, concluding that intermittency/multifractality decreases with heliospheric distance, a result that was confirmed by (KIRAN *et al.*, 2021). A recent investigation utilizing the multifractal detrended fluctuation analysis (MF-DFA) technique revealed that electron density fluctuations in the E-F valley region of the ionosphere exhibit multifractal, asymmetric, intermittent, and non-homogeneous characteristics (NEELAKSHI *et al.*, 2022).

The direct link between intermittency and multifractality of magnetic and velocity field fluctuations in the solar wind was made clear in (SALEM *et al.*, 2009). Using data from the Wind spacecraft, they applied the Haar wavelet transform to filter out intermittency from the time series and showed that the scaling exponents for the structure functions behave as a linear function of statistical moments, as in monofractal processes, therefore attributing multifractality in the solar wind to intermittency. GOMES *et al.* (2019) obtained a similar

linear scaling after filtering out the current sheets from Cluster-1 intermittent magnetic field data, suggesting that the current sheets are the coherent structures responsible for the nonlinear scaling of the structure functions in the solar wind. This was confirmed after inspection of time series of days when current sheets were absent, that also showed a linear scaling.

A question remained on whether the linear scaling found by SALEM *et al.* (2009) and GOMES *et al.* (2019) indeed implies that the filtered time series are monofractal or not, i.e., is the nonlinearity of the distribution of scaling exponents of structure functions a general measure of multifractality or is it just an indication of intermittency, one among different possible sources of multifractality? One of the goals of the current work is to answer this question. In this sense, it is important to stress that the origin of multifractality is not always related to fat-tailed PDFs, as it may also be caused by different correlations in small and large fluctuations, such as linear or nonlinear correlations (KANTELHARDT *et al.*, 2002; WU *et al.*, 2018). The source of multifractality can be investigated by producing surrogates from the original time series. Two types of surrogates are useful in this context (THEILER *et al.*, 1992; LANCASTER *et al.*, 2018). First, shuffling the amplitudes of the original signal breaks all long-range correlations, while keeping the PDF unchanged. Therefore, if the multifractality is due to fat-tailed PDFs, it cannot be removed by shuffling the series. If it is due, solely, to time correlations, the corresponding shuffled series will be monofractal. If both fat-tailed PDF and linear/nonlinear correlations are present, the multifractality of the shuffled series should be smaller than that of the original series (BARUNIK *et al.*, 2012). The second type of surrogate is produced by randomizing the phases of the Fourier modes of the original time series, producing a new series with Gaussian PDF, but preserving the linear correlations of the original series. If the random phases time series becomes monofractal, then nonlinear correlations and/or non-Gaussian PDFs are the source of multifractality. If the multifractality is preserved in the random phases time series, then linear correlations are its source.

Studies of surrogate time series have been conducted to probe the origin of multifractality in a wide range of contexts, including financial markets (BARUNIK *et al.*, 2012), gravitational waves (NEPOMUCENO, 2016), human gate diseases (DUTTA *et al.*, 2013), near-fault earthquake ground motions (YANG *et al.*, 2015), solar irradiance fluctuations (MADANCHI *et al.*, 2017), air pollutants (DONG *et al.*, 2017), meteorological time series of air pressure, air temperature and wind speed (GOS *et al.*, 2021) and rainfall records (SARKER; MALI, 2021). The surrogate method was also employed in time series of CME linear speed during solar cycle 23 to conclude that the multifractality is due to both the broad PDF and long range time correlations (CHATTOPADHYAY *et al.*, 2018). In the first section of results, we use the method to reveal the role of current sheets in the origin of multifractality in the solar wind. By analyzing two qualitatively different magnetic field

time series from Cluster-1, one filled with current sheets and another one void of current sheets, we develop a nonlinear methodology based on the multifractal detrended fluctuation analysis (MF-DFA) method coupled with the volatility and surrogate time series. Thus, the contribution of small- and large-scale magnetic fluctuations can be quantified in different types of multifractal solar wind series. It is revealed that when the multifractality is not mainly due to the PDF, the scaling exponents display an almost linear behavior as a function of the moments of the structure function, despite the presence of strong multifractality in the series. In addition, we employ the p-model (HALSEY et al., 1986; MENEVEAU; SREENIVASAN, 1987) to confirm that the multifractality in both types of solar wind time series can be attributed to a turbulent energy cascade process.

1.2 Multifractal Analysis of Active Region

Active regions (AR) are regions of the sun's surface and atmosphere where strong magnetic fields, sunspots, plages, flares and other activities occur (GOLUB; PASACHOFF, 2014). The use of a robust analysis is critical to characterize the physics behind the growing of these turbulent regions (CONLON et al., 2008). The magnetic field configuration of these structures, which are coupled with boundary perturbations, is responsible for their evolution. These perturbations and the magnetic flux ropes rising to the solar surface lead to evolving turbulent flows where the associated magnetic Reynolds number is about $\approx 10^8$ on the photosphere (PARKER, 2019). ABRAMENKO (2005) shows that this magnetic flux distribution presents self-similarity characteristics related to nonlinear processes.

As already known in the literature, the magnetic field of AR follows a power-law distribution (ABRAMENKO, 2005b), i.e., the evolution of AR is deeply related to coherent process. This means that the energy related to active regions has a self organized criticality nature; therefore a nonlinear analysis method is needed to understand the properties of this chaotic system.

Due to their complex behavior, a series of methods were applied by different authors to quantify the turbulent processes that are present in AR. As presented in this work, the scale sensitivity inherent to multifractal analysis is a powerfull tool to characterize their behavior. CADAVID et al. (1994) was the first to apply a multifractal method to an active region, comparing this structure with simulated data. Later, ABRAMENKO et al. (2002) using a two dimensional variation of the structure function (FRISCH, 1995), observed a growing multifractality following the AR evolution. In 2005, MCATEER et al. applied a fractal analysis to a large series of active region images, founding poor correlation between multifractality and flare activity. ABRAMENKO (2005) compared the structure functions of gaussian fields and active magnetograms and later ABRAMENKO (2005) calculated the

power spectrum of several flaring active regions, relating them with a Kolmogorov-type
$(-5/3)$ spectrum (KOLMOGOROV, 1941). Also in 2005, GEORGOULIS collected a series of
fractal and multifractal methods, e.g., zeta function and fractal dimension, to obtain a
tool to predict flare events. Thereafter, MCATEER *et al.* (2007) calculated the multifractal
spectra using *Wavelet Transform Modulus Maxima* (WTMM) for different bands of X-ray
emission of a X4.8 flare. Subsequently, HEWETT *et al.* (2008) observed the evolution of
the energy spectrum of two AR through the WTMM method, but with unsatisfactory
results regarding solar flare prediction. Shortly thereafter, CONLON *et al.* (2008) restored
the multifractal analysis CADAVID *et al.* (1994) using the singularity spectrum $(f(\alpha) \times \alpha)$
to investigate the variation of multifractality over time for four active regions (Fig. 1.1).
However, surprisingly, this work revealed a multifractal index reduction with the region
formation and flaring activity. Another curious point is that due to the method's limita-
tions, just a portion of the relevant multifractal parameters's space was explored.
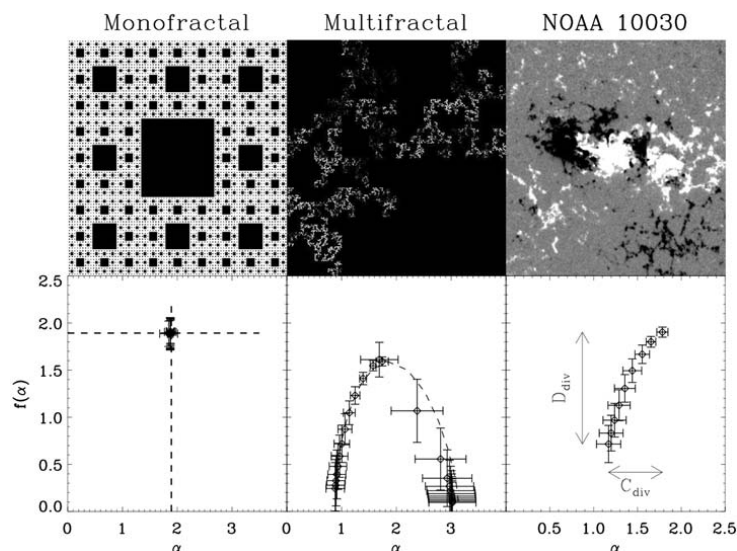
FIGURE 1.1 – Top: Representation of sample monofractal, multifractal and magnetogram images (NOAA
10030), respectively. Bottom: Singularity spectrum of each upper structure. Source: (CONLON *et al.*, 2008)

Now redirecting this analysis to AR 11158, ERMOLLI *et al.* (2014) applied the multi-
fractal method used by CONLON *et al.* (2008) to this active region, finding a sensitivity of
the parameters to the spatial resolution and also a reduction of multifractality. However,
GEORGOULIS; GEORGOULIS (2012,2013) used different methods of multiscale parameters
calculation to AR 11158 and obtained opposite results, i.e., a mutifractality growth; but
also with no possibility to predict any flaring activity for the same active region.

In the present work, we exhibit the results obtained by the two-dimensional multifrac-
tal detrended moving average (MFDMA) analysis of the AR 11158 magnetograms over 6
days of observation. An expressive growth of the multifractality is observed, in conformity
with the evolution of the active region.

1.3   Vortex Detection in Active Regions

The evolution of solar magnetic fields is strongly influenced by vorticity. BRANDT *et al.* (1988) for the first time observed through the *Swedish Solar Telescope* a photospheric vortex with 1.5 hour lifetime and about 5 Mm in a supergranular junction region. BRANDT *et al.* (1988) proposed that the process behind the coronal heating system comes from the electric currents at the base of magnetic flux tubes generated from twisted magnetic fields by vortices. In 2009, ATTIE *et al.* analyzed *Hinode* quiet Sun images and observed two vortices with lifetimes about 1 and 2 hours. Furthermore, INNES *et al.* (2009) detected small CMEs and mini-flares at supergranular cells junctions and suggested that they are caused by small portions of opposite-polarity magnetic fields twisted by rotating photospheric flows.

Concerning active regions, the evolution of vortices leads to strongly twisted magnetic fields, i.e., *non-potentiality*, where the energy is accumulated until it is released through flaring and CMEs (SCHRIJVER *et al.*, 2008; SUN *et al.*, 2012). ZHANG *et al.*; YAN *et al.* (2007,2008) analyzed the magnetic field and sunspot evolution for ARs and observed a relation between the major solar flares and the interaction of rapidly rotating sunspots. These rotating sunspots and emerging flux regions (EFRs) are associated with the increase of magnetic shear. SONG *et al.* (2013) did a thorough analysis of different areas of AR 11158 and detected vortical photospheric flows related to rotating sunspots. They also observed that vortices are responsible for the increase of magnetic field twisting and thus to major flare formation, in particular, a X2.2-class flare (SONG *et al.*, 2012) (Fig. 1.2). In 2012, SUN *et al.* applied the nonlinear force-free field (NLFFF) extrapolation to show the growth of the horizontal B component related to flare activity. JIANG *et al.* (2011) focused the research at the persistent vortex related to the X2.2 flare and found an interaction between the emerging pole P2 and rotating opposite-polarity sunspot (see Fig. 1.2). This clockwise vortex persists for about 20 hours until it collides with an opposite-polarity region, causing a flux cancellation. They suggest that the rotation and the shearing are responsible for energy and helicity contribution for the X flare and therefore, the collision and cancellation moment can be the trigger to the major flaring event. GRIMES *et al.*; GRIMES; PINTÉR (2020,2022) studied the sunspot group rotation for different ARs, observing that rotation leads to magnetic field twisting with instabilities that may conduct to an eruption and also that ARs with more rotating groups perform more flare activity.
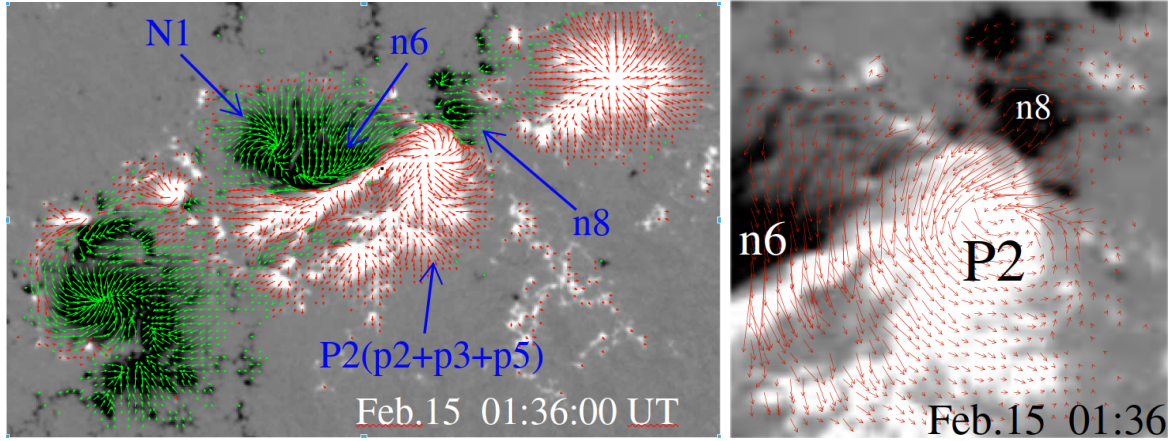
FIGURE 1.2 – Magnetograms visualization for an instant before X2.2 flare event. Green and red arrows indicate the horizontal magnetic field. 'P' and 'N' denote positive and negative polarities. Source: (SONG *et al.*, 2013)

The aforementioned works analyzed the presence of vortical structures through the visual inspection of azimuthal variations of the vector magnetic field. Over the years, however, more consistent definitions have been sought to describe and detect these coherent structures in fluids. In 2016, HALLER *et al.* proposed the *Lagrangian Averaged Vorticity Deviation* (LAVD) method to detect objective Lagrangian vortices, i.e., vortices that are invariant under continuous time-dependent changes of the reference frame or observer (see references (CHIAN *et al.*, 2019; SILVA *et al.*, 2020) for examples of its use in the context of solar physics). REMPEL *et al.* (2016) adapted the LAVD method to detect magnetic vortices in numerical simulations (REMPEL *et al.*, 2019; SILVA *et al.*, 2020) and solar atmospheric data (CHIAN *et al.*, 2023). SILVA *et al.* (2021) successfully applied this new method, called *Integrated Averaged Current Deviation* (IACD), to detect magnetic vortices in the intergranular region of the photosphere using realistic numerical simulations of magnetoconvection.

Our work employs Lagrangian objective vortex detection techniques for the first time to an active region. Two particular vortices are followed. The first one, related to an M-class flare formation, and a second one directly linked to an X-class flare formation. The results support the idea of rotating sunspots as a trigger to bigger flares formation. In addition, we applied the two-dimentional MFDMA anlysis to the vortical window related to X-flare formation to see how this coherent structure affects an area of the AR and how the parameters obtained are also affected by the morphology of the vortex.

This work is organized as follows. Chapter 2 presents the theoretical background on solar wind turbulence, photospere and fractal analysis. In Chapter 3, the Multifractal Analysis methodology is described as well as the Zeta function, *p*-model and integrated averaged current deviation (IACD), together with a methodology review of these tools. In Chapter 4, all the results of the multifractal analysis of two solar wind time series are

described, including their volatility time series, the surrogate analysis for four time series, and also the scaling exponent analysis of the original and surrogate times series with the p-model analysis (BATISTA *et al.*, 2022). In addition, the results related to multifractal and IACD methods applied to active regions are presented. Finally, Chapter 5 presents the conclusions obtained by the present research.

2 Theoretical Background

2.1 Solar Wind Turbulence

The solar wind is an ideal medium for the study of turbulence in space plasma. As known from the literature, the heliosphere is not in hydrostatic equilibrium. Due to geometrical constraints and gravitational effects in the surface of the Sun, critical regions are formed where the radial velocity equals the sounds speed (BRANDENBURG; NORDLUND, 2011). In addition, the Sun's magnetic field extends into the interplanetary medium and carries with it an energetic plasma. The existence of such environment results in a supersonic and super-Alfvénic plasma flow called *Solar Wind*, which comes from the Sun and expands into the whole heliosphere (BRUNO; CARBONE, 2005; VELTRI, 1999). This transonic flow reaches speeds around $300 - 400$ km s^{-1} at low latitudes (solar equatorial) and $750 - 800$ km s^{-1} at higher latitudes, where the flow is considered homogeneous. The origin of the high-speed solar wind comes from the open magnetic field lines in the coronal holes, while low-speed flow comes from field lines adjacent or inside the coronal streamers and active regions (VELTRI, 1999).

All this turbulent flow comes with large amplitude fluctuations on time scales that range from seconds to hundreds of hours (BRANDENBURG; NORDLUND, 2011), with associated frequencies lower than the ion-cyclotron frequency, $10^{-6} < f < 1$ Hz. The time variation of these fluctuations may be due to spatial variations advected by solar wind velocity, which leads to *Taylor's Hypothesis*, i.e., the turbulent fluctuations are advected by the mean flow (velocity U_0) as if fluctuations were frozen in the flow (VERMA, 2022). By considering the solar wind velocity $v_{sw} \sim 400$ km s^{-1} it is possible to link f with the wavelengths $l = v_{sw}/f$ and obtain the distance range of 400 km $< l <$ 1 AU.

These fluctuations follow a power law spectrum over all the frequency range

$$E(k) \propto k^{-\alpha}. \tag{2.1}$$

where α is the spectral index and has a range of values. This aspect may be considered the main characteristic of the fully developed magnetohydrodynamic (MHD) turbulence

generated by a nonlinear energy cascade process (VELTRI, 1999).

2.1.1   Kolmogorov Theory

Another inner property of fully developed MHD turbulence is how the system reaches the dynamical equilibrium between the energy inflow provided by some large-scale instability and the energy outflow caused by the small-scale dissipation (BISKAMP, 2003).

The dynamics of the spectral energy flow through a cascade process weas first idealized by Richardson (RICHARDSON, 1922). In this process turbulence is formed by a collection of eddies in different scales where the larger ones transfer part of the energy to smaller ones in a constant way through non-liner interactions (BISKAMP, 2003) 2.1 .
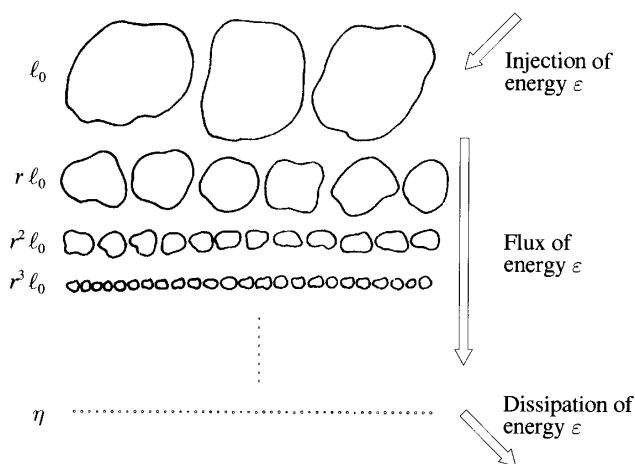
FIGURE 2.1 – Cascade model for the Kolmogorov 1941 theory. Source: (FRISCH, 1995)

To describe this phenomenology, the KOLMOGOROV (1941) theory is one of the most important models in the literature. The K41 theory assumes that turbulence follows an energy cascade process 2.1, whereby large scale structures brake into successively smaller structures until they reach a scale with molecular viscous forces. This process is divided into three scale ranges: an energy injection range, including the largest scales up to a maximum wavenumber k_{in}, an energy transferring range, or inertial range, and a dissipative range, beginning at some wavenumber k_d and going up to the smallest scales. In the inertial range turbulence is isotropic and homogeneous, which means that energy transfer through scales is constant, i.e., it is scale invariant. As a result, Kolmogorov estimated for the energy power spectrum in the inertial range a spectral index of $-5/3$ (KOLMOGOROV, 1941; FRISCH, 1995),

$$E(k) \propto k^{-\frac{5}{3}}.$$

(2.2)
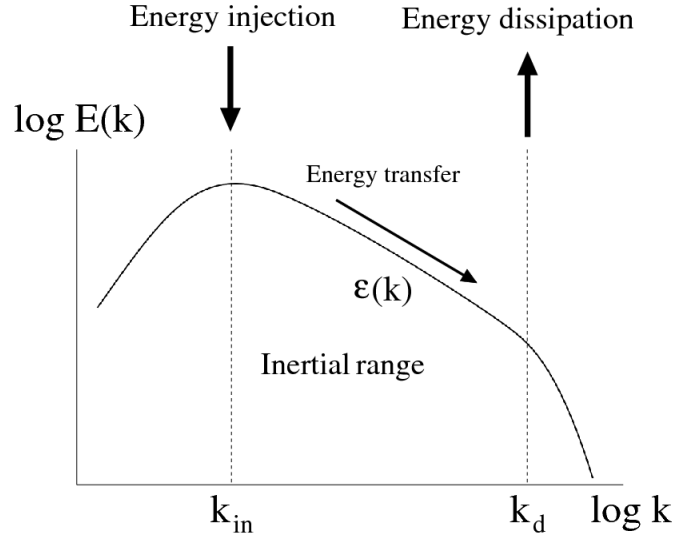
FIGURE 2.2 – Turbulent PSD indicating the energy injection, inertial and energy dissipation ranges. Source: (GUTBERLET, 2011)

2.1.2 Iroshnikov-Kraichnan Theory

The *Iroshnikov-Kraichnan* (IK) MHD turbulence model is a K41 modification with an alternative model of nonlinear energy flux. In the IK model energy is transported by Alfvén waves which propagate through the local magnetic field (BISKAMP, 2003). Analogously to K41, the IK energy spectrum inertial range is estimated to follow a power law

$$E_{K41}(k) \propto k^{-\frac{3}{2}}. \tag{2.3}$$

2.1.3 Current Sheet Detection

To understand the character of intermittent events (small-scale eddies increasingly sparsely distributed) BISKAMP (2003) in MHD it is necessary to identify the main coherent structures in the flow. These structures randomly appear and disappear in the fluid, carrying a large amount of energy and dominating the statistics of small scales (BRUNO; CARBONE, 2005). In the solar wind, these intermittent events occur on time scales of a few minutes and one of their major sources are the *current sheets* (LI *et al.*, 2011). Current sheets can be described as thin magnetic coherent structures, which are almost incompressible, located in an electric current area associated with nearly two-dimensional regions contained in a plasma (GUTBERLET, 2011).

The magnetic field direction changes abruptly in the presence of current sheets (LI *et al.*, 2011). VELTRI (1999) found that the magnetic field rotation angle across current sheets is about 120-130 degrees in the solar wind. To detect these discontinuities in a

magnetic field time series, we use Li's method (LI, 2007), which is focused in the magnetic field rotation. This technique is based on the probability density, for a given time interval τ, of finding an angle between vectors $\mathbf{B}(t)$ and $\mathbf{B}(t+\tau)$ inside the interval θ and $\theta + \Delta\theta$:

$$f(\theta, \tau)\Delta\theta = \frac{N^\tau(\theta < \theta' < \theta + \Delta\theta)}{N^\tau(0 < \theta' < \pi)} \tag{2.4}$$

where $N^\tau(\theta < \theta' < \theta + \Delta\theta)$ is the number of pairs of vectors $\mathbf{B}(t)$ and $\mathbf{B}(t+\tau)$ inside the interval θ and $\theta + \Delta\theta$ and $N^\tau(0 < \theta' < \pi)$ is the total number of measurements. So, the integrated distribution function given by

$$F(\theta, \tau) = \int_\theta^\pi d\theta' f(\theta', \tau) \tag{2.5}$$

is the frequency of occurrence of angles larger than θ. If there are current sheets in $\mathbf{B}(t)$, then $F(\theta, \tau)$ follows a linear scaling law with τ for θ larger than a critical angle θ_c

$$F(\theta, \tau) \sim F(\theta, N\tau) \quad \text{when} \quad \theta > \theta_c. \tag{2.6}$$
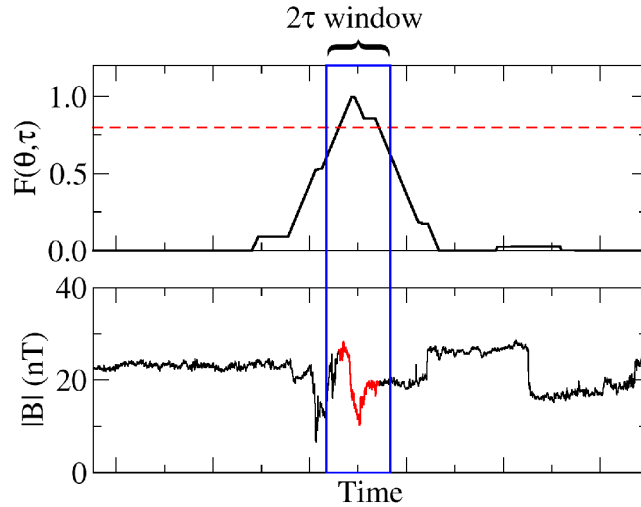
FIGURE 2.3 – Li's method to find current sheets in a magnetic field series. The upper figure shows the sliding window (blue) of size 2τ and the threshold L for the current sheet detection (red dashed lines). The lower figure shows the related region in the magnetic field where the current sheets are located (red).

If a percentage L or more of the angles formed by $\mathbf{B}(t)$ and $\mathbf{B}(t+\tau)$ in a 2τ window size, centered at time T, are larger than θ_c, then there is a current sheet centred on time T.

2.2   Photosphere

By observing the full spectrum of phenomena present in the Sun, the solar flare stands out by its intensity, diversity and frequency of occurrence in different parts of the Sun's surface and Sun's atmosphere. This solar atmosphere is composed of 3 main regions: *Photosphere*, *Chromosphere* and *Corona*, Figure 2.4, with a *Transition Region* between the Chromosphere and the Corona.

The photosphere is the lowest region of the solar atmosphere, representing the upper edge of the convection zone. The material in this region is in constant motion due to convective energy transport in the lower layer, giving it a polygonal granular characteristic. Another relevant characteristic of the photosphere is the presence of darker zones, when compared to nearby regions, caused by the temperature decrease resulting from the localized reduction in energy transport where the magnetic fields are most intense. These dark regions are known as *Sunspots* and are associated with specific areas of strong magnetic field called *Active Regions* (AR). All of these structures provide an environment that is conducive to the formation of solar flares.
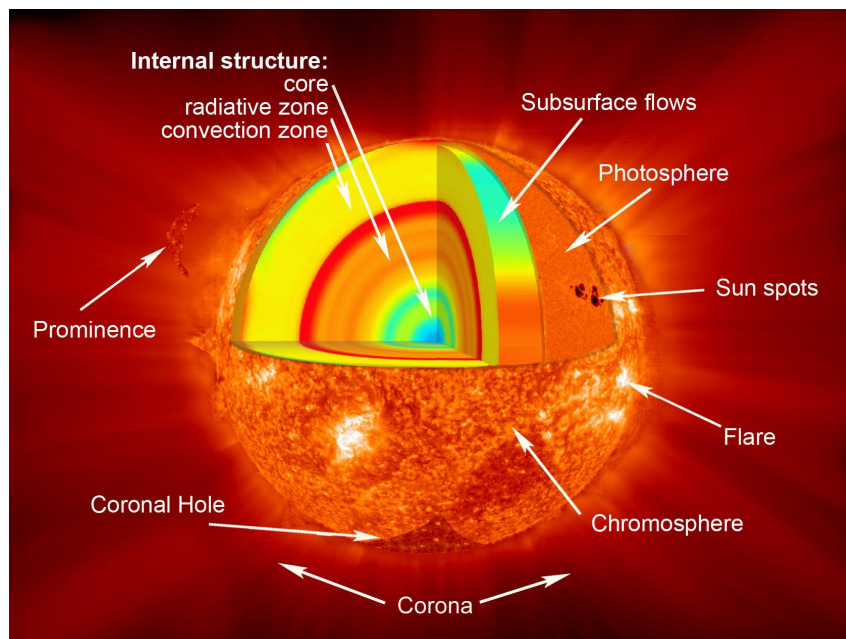
FIGURE 2.4 – Illustration of Sun's layers. Source: (SUN, 2013)

2.2.1   Solar Flare

As described by (SHIBATA; MAGARA, 2011), solar flares are explosive events observed in the solar atmosphere loaded with plasma. The energy released from a flare is $\sim 10^{21} - 10^{25}$ J, emitting radiation across different wavelengths of the electromagnetic spectrum in a time interval about $(10^3 - 10^4 s)$, Figure 2.5. The flaring loops can reach heights ranging

from 10^4 to $10^5 km$ and are located in active regions. (CARRINGTON, 1859; HODGSON, 1859) (1859) described for the first time a solar flare around a sunspot. To identify and quantify the intensity of these events, a classification method has been developed according to X-ray peak flux (W/m^2) with a $(1-8$ Å$)$ variation in a log scale (BAI; STURROCK, 1989). This flare scale is defined by increasing order of intensity A, B, C, M and X 2.1, where each class splits into 9 sub-scales (e.g., X1, ..., X9-class). Figure 2.6 shows a X-ray flux time series detected by GOES satellite of the AR 11158 on 2011 February, highlighting the M-class (M6.6, M1.0, M1.1) and the X-class flare (X2.2) events. Table 2.1 shows the flare scale according to X-Ray peak flux.
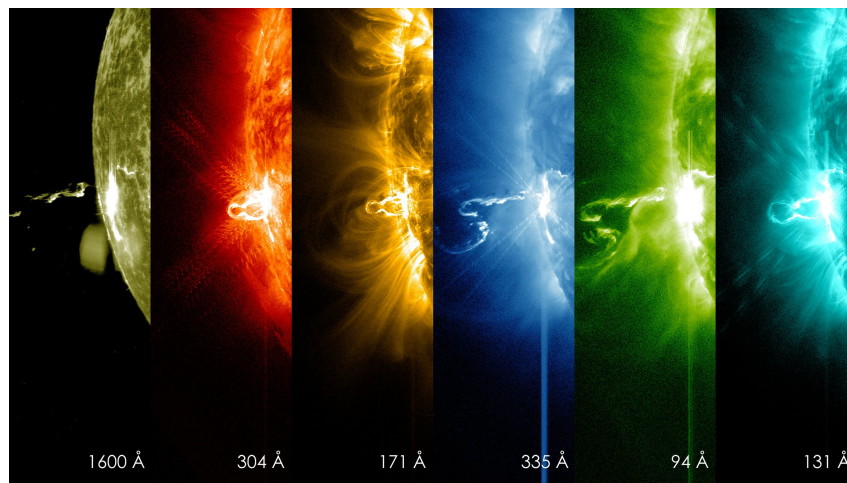
FIGURE 2.5 – X4.9-class flare image in different wavelengths. Source: (NASA'S..., 2014)
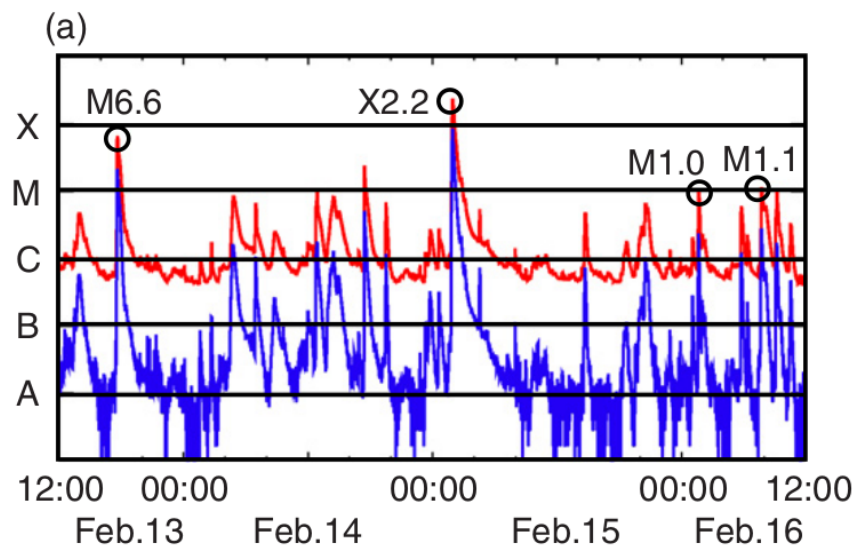
FIGURE 2.6 – X-ray flux time series of the AR 11158 on 2011 February 13-16. Source: (INOUE *et al.*, 2013)

TABLE 2.1 – Solar flare classification in terms of X-ray peak flux.

Class	Peak Flux Range (Wm^{-2})
A	$< 10^{-7}$
B	$10^{-7} - 10^{-6}$
C	$10^{-6} - 10^{-5}$
M	$10^{-5} - 10^{-4}$
X	$> 10^{-4}$

2.3 Fractal Time Series

The word "fractal" was coined from Benoit Mandelbrot from the Latin adjective *fractus* and means "irregular, fragmented" (MANDELBROT *et al.*, 1983). The related Latin verb *frangere* means "to break". Mandelbrot defines fractal structures as very irregular shapes, in either mathematics or nature, wherein each small part is very much like a reduced size image of the whole (MANDELBROT *et al.*, 2014), i. e., they are self-similar. Fractal structures are not well defined by Euclidean geometry, i. e., usually they don't have an integer value dimension, like a square or a cube and their dimension is called *fractal dimension D* or *Hausdorff-Besicovitch dimension* (MANDELBROT *et al.*, 1983). D is also called *box dimension* and is obtained by a process called *box counting*, which is based on length measurement by covering the shape with a number of boxes $N(\delta)$ with different sizes δ. This counting leads to a scaling law:

$$N(\delta) \sim \delta^{-D}.\tag{2.7}$$

One good example of fractal dimension D measurement is the triadic Koch curve. The curve starts as a line segment of size $L(1) = 1$. The following process, defined as first generation, is replacing $1/3$ of the central line by two new segments with the same length $L/3$, creating a 4 line segments curve of total length $L(1/3) = 4/3$. So, in the second generation we have a curve of $N = 4^2 = 16$ segments with lenght $\delta = 1/9$ and total length $L(1/9) = (4/3)^2 = 16$. The process is repeated until the n-th generation, resulting in a curve of length

$$L(\delta) = \left(\frac{4}{3}\right)^n\tag{2.8}$$
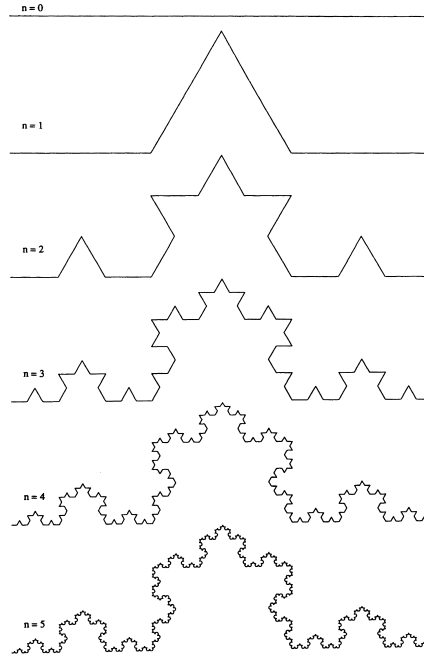
FIGURE 2.7 – Construction of the triadic Koch curve. Source: (FEDER, 1988).

with each line segment of size

$$\delta = \left(\frac{1}{3}\right)^n \quad \text{or} \quad n = -\frac{\ln \delta}{\ln 3} \tag{2.9}$$

The length may be expressed as:

$$L(\delta) = \exp\left(-\frac{\ln \delta (\ln 4 - \ln 3)}{\ln 3}\right) = \delta^{1-D} \tag{2.10}$$

with

$$D = \frac{\ln(4)}{\ln(3)} \approx 1.26 \quad \text{and} \quad N(\delta) = \delta^{-D} \tag{2.11}$$

where D is the fractal dimension and N is the number of segments (FEDER, 1988).

Besides all the contribution to image fractal characterization, Mandelbrot was also one of the first to apply fractal analysis to natural time series (MANDELBROT; NESS, 1968; MANDELBROT; WALLIS, 1969; MANDELBROT *et al.*, 2014), based on Harold Edwin Hurst's studies on hydrological systems (HURST, 1956; HURST *et al.*, 1965). In the present work, we focus in the fractal behavior present in solar wind time series, specially the self-similarity aspect.

To describe complex systems, it is necessary to understand that systems produce time series with fluctuations on a wide range of time scales and values. These natural fluctuations may follow a scaling relation with different time scales that can be interpreted as a fractal scaling behavior Fig. 2.8.
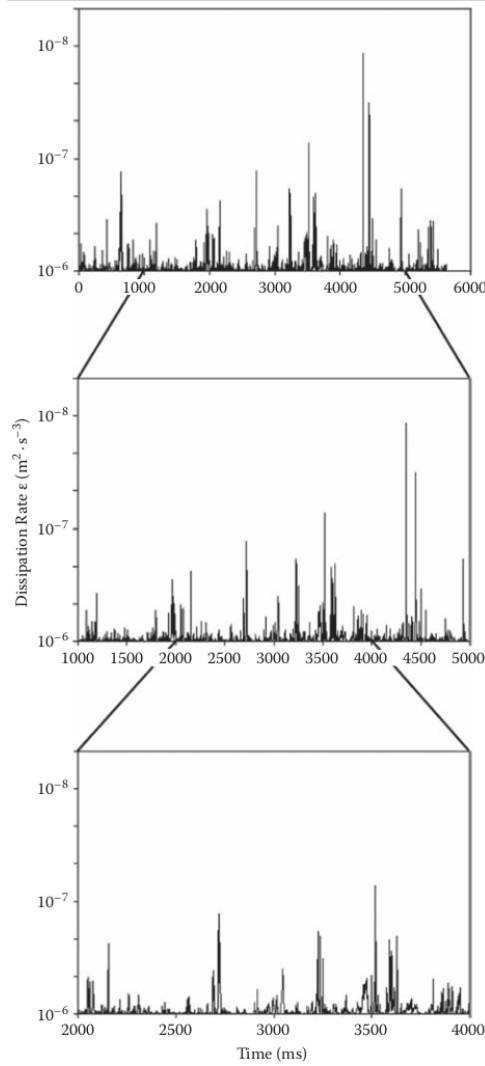
FIGURE 2.8 – Time series of microscale turbulent kinetic energy dissipation rates. At zooming in, the structures remain very similar. Source: (SEURONT, 2010).

2.3.1 Self-similarity, self-affinity and the Hurst exponent

Self-similarity and self-affinity are both characteristics of fractal structures. Fractals with identical scaling in all directions, *isotropic*, are defined as *Self-similar*. But if this scaling similarity is anisotropic, i.e., for some directions the scaling factor is different, then the fractal is *self-affine* Fig. 2.9.

Self-similarity and self-affinity are also present in the context of fractal time series, and they are linked to a parameter known as *Hurst Exponent H* (HURST *et al.*, 1965). A self-similar time series is scale-invariant and follows a power law relation between the fluctuation $F(s)$ and the time scale parameter s, given by $F(s) \approx s^H$. But for self-affine fractal time series, s is rescaled by a factor a and the fluctuation's relation with s is now defined as $F(s) \approx a^H F(as)$ (KANTELHARDT, 2008).

Harold Edwin Hurst was the first to propose a method to analyse long-term persistence
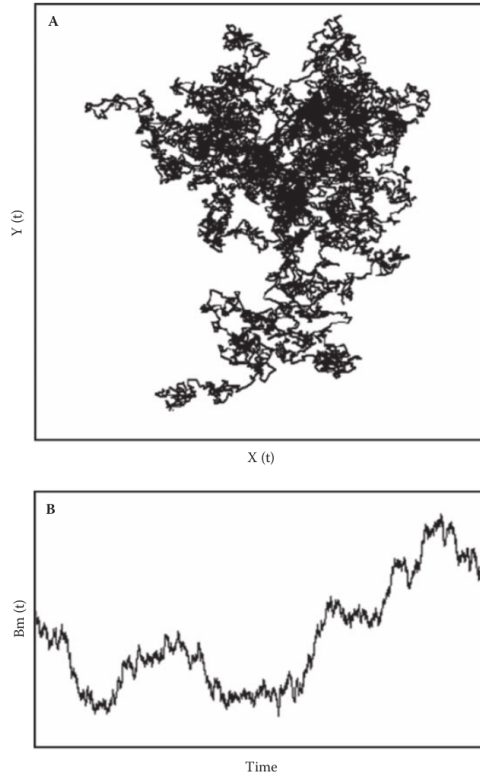
FIGURE 2.9 – Self-similar (A) and self-affine (B) fractal examples. A is the Brownian motion in two-dimensional space and B is the $x(t)$ plot of a particle coordinate. Source: (SEURONT, 2010).

in time series using random walk theory. The rescaled range analysis consists of a few steps: First, the time series $\tilde{x}_i$ is divided into non-overlapping segments ν of size s, generating $N_s = int(N/s)$ segments. In the second step, the data is integrated in each segment $\nu = 0, ..., N_s - 1$:

$$Y_\nu(j) = \sum_{i=1}^{j} (\tilde{x}_{\nu s} - \langle \tilde{x}_{\nu s+i} \rangle_s) \tag{2.12}$$

This subtracts the local averages, eliminating constant data trends. The third step is to compute the differences between minimum and maximum values $R_\nu(s)$ and the standard deviations $S_\nu(s)$ for each segment

$$R_\nu(s) = max_{j=1}^{s} Y_\nu(j) - min_{j=1}^{s} Y_\nu(j), \quad S_\nu(s) = \sqrt{\frac{1}{s} \sum_{j=1}^{s} Y_\nu^2(j)}. \tag{2.13}$$

At last, the scaled range is averaged over all segments, generating the fluctuation function:

$$F_{RS}(s) = \frac{1}{N_s} \sum_{\nu=0}^{N_s-1} \frac{R_\nu(s)}{S_\nu(s)}, \qquad F_{RS}(s) \sim s^H \quad \text{for} \quad s \gg 1, \tag{2.14}$$

where H is the *Hurst Exponent* (KANTELHARDT, 2008).

Hurst applied his method for the raining levels at Nilo River Fig. 2.10 and observed the following characteristics of the time series associated with the H index:

1. For time series with $H > 0.5$, they exhibit a long-range correlation dependence structure, i.e., long "memory", and are denominated *correlated* or *persistent* time series;

2. Time series with $H < 0.5$ show a short-range dependence structure, i.e., short "memory", and are defined as *anti-correlated* or *anti-persistent*;

3. Finally, totally random time series have no "memory" and $H \simeq 0.5$. They are called *independent* or *uncorrelated* time series.
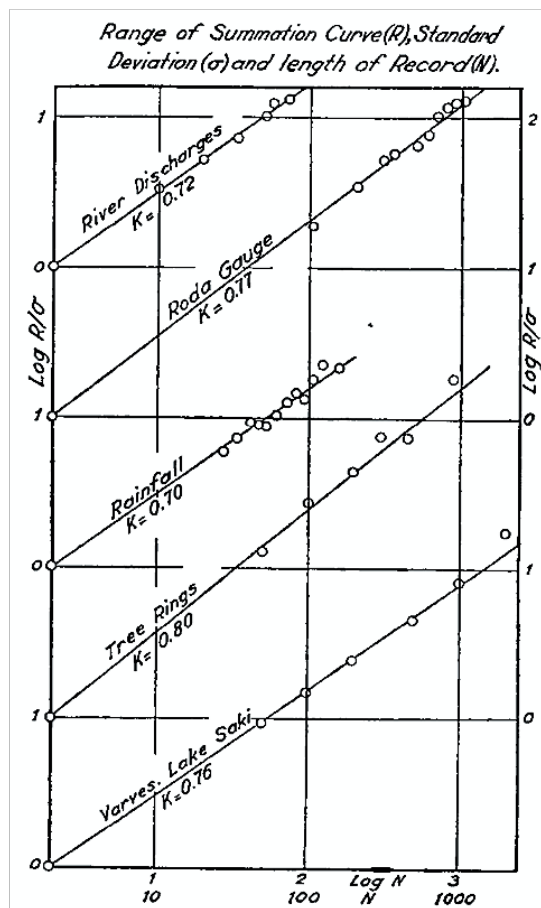
FIGURE 2.10 – Relation between range of summation curve R, standard deviation S; (a), and length of record N. Source: (HURST *et al.*, 1965)

Another interesting aspect related to the Hurst Exponent is the stationarity (or non-stationarity) of the data. Using the random walk idea, i.e, Brownian motion, Mandelbrot introduced the concept of *fractional Brownian motion* (fBm), $B_H(x)$, which is a generalization of the Brownian motion. $B_H(x)$ is formed by random functions with Gaussian

increments $B_H(x_i) - B_H(x_{i-1})$, i.e., a non-stationary signal with stationary increments, where the variance is

$$\left\langle |B_H(x_i) - B_H(x_{i-1})|^2 \right\rangle = k\,|x_i - x_{i-1}|^{2H} \tag{2.15}$$

where k is a constant and $0 < H < 1$. As we can see, this relation follows a power law where any change by a factor δ in scale t will also modify $\Delta B_H = B_H(x_i) - B_H(x_{i-1})$, by a factor δ^H:

$$\left\langle \Delta B_H(\delta x)^2 \right\rangle = k\delta^{2H} \left\langle \Delta B_H(x)^2 \right\rangle \tag{2.16}$$

This difference scaling factors in two coordinates (δ for x and δ^H for B_H) reveals a self-affinity for fBm signals (SEURONT, 2010).

The other characterization of self-affine time series is the Fractional Gaussian noise (fGn), a generalization of the white Gaussian noise defined as a series of successive increments in an fBm (SEURONT, 2010). In other words, the increments

$$y_{fGn}(i) = x_{fBm}(i) - x_{fBm}(i-1) \tag{2.17}$$

yield a stationary fGn signal and vice versa:

$$x_{fBm}(n) = \sum_{i=1}^{n} (x_{fGn}(i) - \langle x_{fGn} \rangle). \tag{2.18}$$
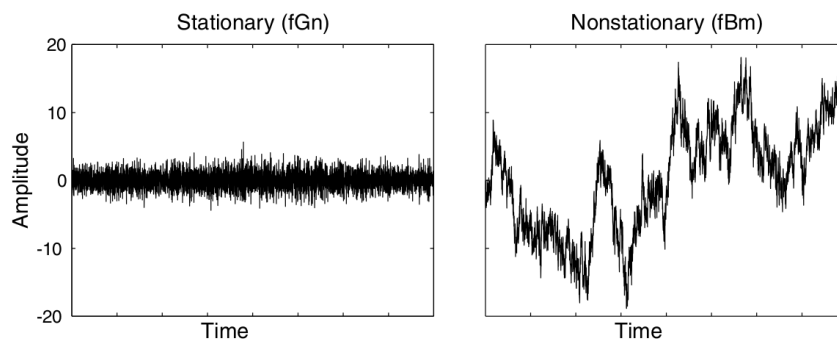
FIGURE 2.11 – Two Monofractal time series examples. Left is fractional Gaussian noise and at right the fractional Brownian motion generated by cumulative sum. Source: (EKE *et al.*, 2002)

So, the cumulative sum of a fGn results in a fBm series and when a fBm is differenced this results in a fGn Fig. 2.11. This property is extremely important to fractal analysis because it is directly linked with the Hurst Exponent. One of the methods to identify a time series profile is through H, Fig. 2.12: (i) H range is limited to $0 < H < 2$ (KANTELHARDT, 2008); (ii) fGn series are limited to $H < 1$, where for long-range correlations $0.5 < H < 1$ (EKE *et al.*, 2002). The value of H is increased or decreased by 1 if the data is

integrated (fBm) or differetiated (fGn), respectively (KANTELHARDT, 2008). In sections 3.1 and 4.2.1.1 we see the method for H estimation and the need for differentiating some of our series.
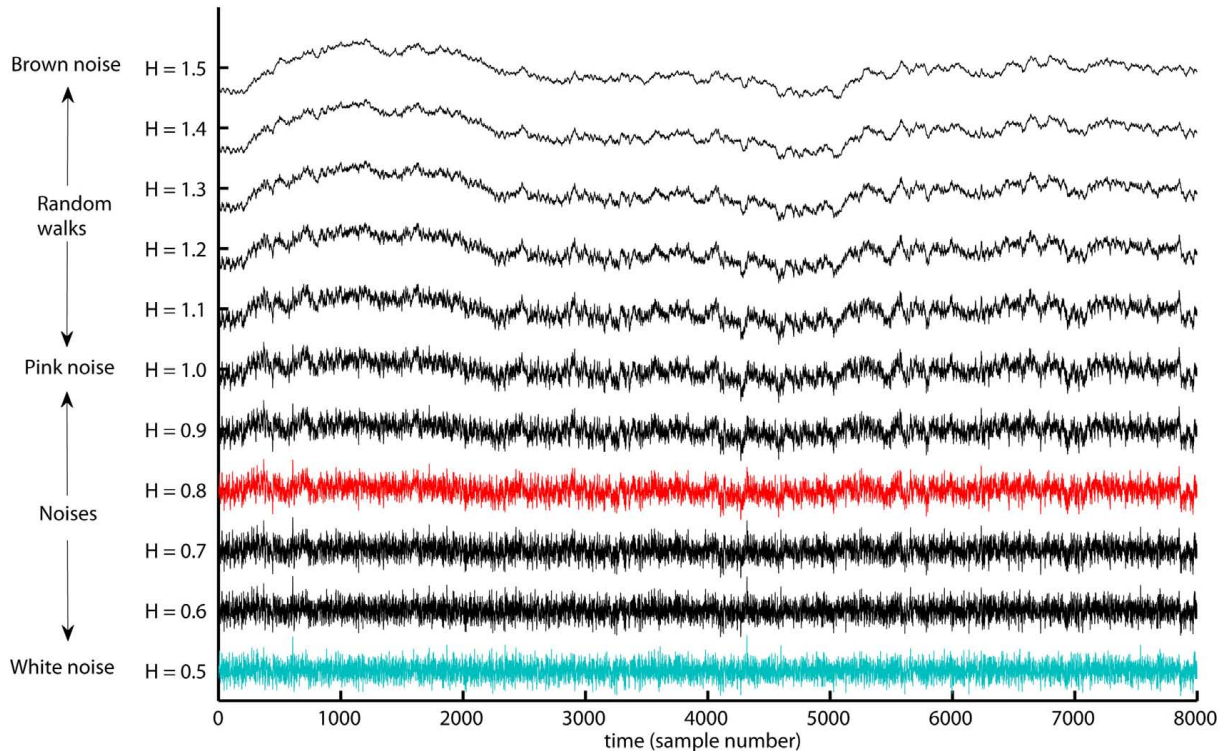
FIGURE 2.12 – Time series profile variation as function of H value. fGn (Noise) series are restricted to $H < 1$ and fBm (Random walks) series have $H > 1$. Source: (IHLEN, 2012)

2.3.2   Monofractal and Multifractal Time Series

As seen in the previous sections, the term 'fractal time series' usually refers to a single fractal or *monofractal time series* (EKE *et al.*, 2002). Monofractal signals are defined by a single power law exponent and their scale invariance is independent of time and scale (IHLEN, 2012). However, *multifractal time series* are heterogeneous, i.e., they have self-similarity only in specific ranges of the structure. This means that their fractal measure varies with time and space, which makes them to be characterized by a set of local fractal values (EKE *et al.*, 2002). So, now to describe a multifractal series, a set of multifractal power law exponents are needed. Multifractal analysis is described in more details in the next chapter.
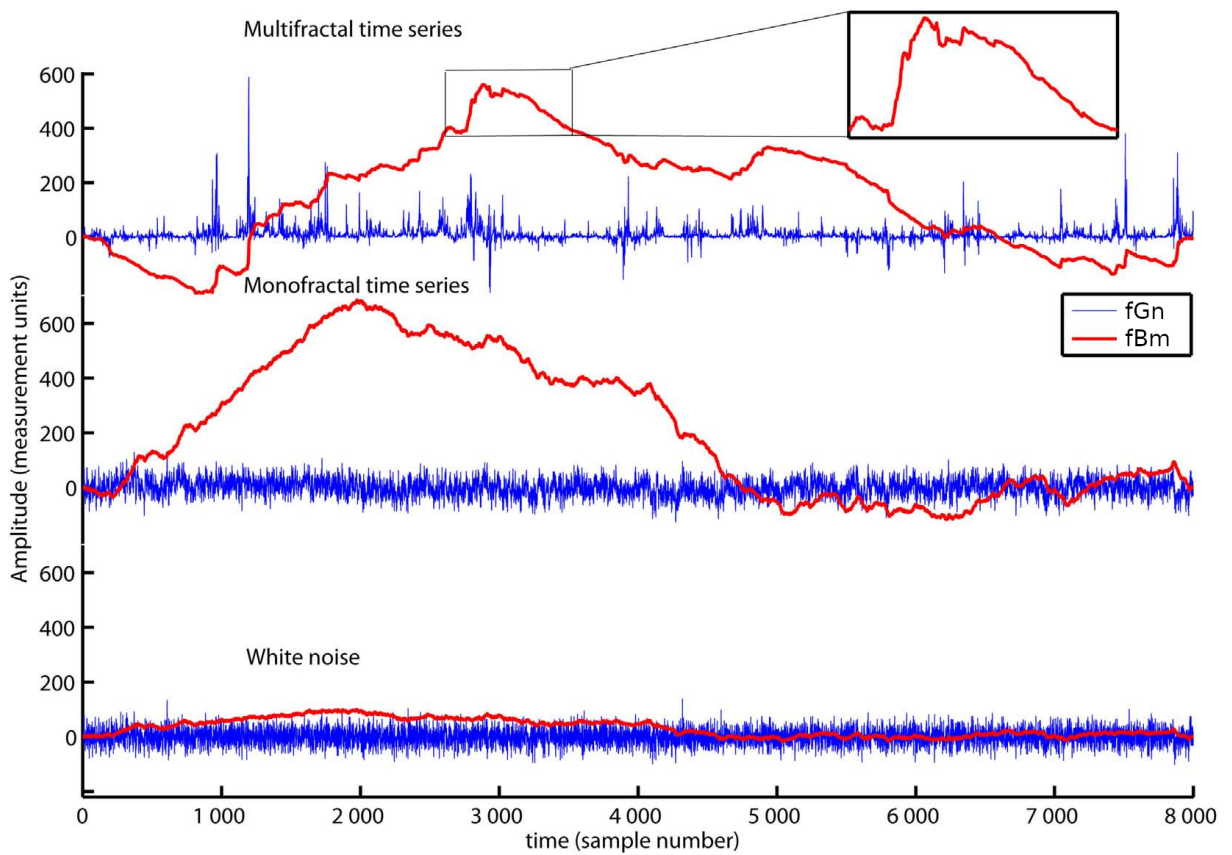
FIGURE 2.13 – fGn (blue) Time series for Multifractal (upper), Monofractal (middle) and White Noise (bottom). fBm of the respective time series. Source: (IHLEN, 2012)

3 Methodology and Research Review

3.1 Detrended Fluctuation Analysis

The *Detrended Fluctuation Analysis* (DFA) method is a technique for the determination of the monofractal scaling properties and power law for long-range correlations in non-stationary time series (PENG *et al.*, 1994; KANTELHARDT *et al.*, 2002). This method was applied for the first time by PENG *et al.* (1994) to find long-range correlations and remove nonstationary trends in DNA sequences and has been successfully used in diverse fields of science, like physics, meteorology, medicine and economy (IHLEN, 2012; EKE *et al.*, 2002; LIU *et al.*, 1997; SANTOS *et al.*, 2019). The DFA method consists of three steps:

1. The time series x_k is integrated:

$$Y(i) = \sum_{k=1}^{i} [x_k - \langle x \rangle], \qquad i = 1, ..., N \tag{3.1}$$

    where $\langle x \rangle$ is the average value.

2. The series $Y(i)$ is divided into $N_s \equiv \text{int}(N/s)$ non-overlapping segments with equal lengths s (Fig. 3.1). Since N is usually not a multiple of s, some of the data points in the time series may be left out of the last segment. To fix this, the procedure is repeated starting from the opposite end of the time series and going backwards. Consequently, $2N_s$ segments are obtained.

3. The local trend for each $2N_s$ segments is calculated. Then the variance (Fig. 3.2) is given by

$$F^2(s, \nu) = \frac{1}{s} \sum_{i=1}^{s} \{Y[(\nu - 1)s + i] - y_\nu(i)\}^2, \tag{3.2}$$

    for each segment indexed by $\nu = 1, \ldots, N_s$ and

$$F^2(s, \nu) = \frac{1}{s} \sum_{i=1}^{s} \{Y[N - (\nu - N_s)s + i] - y_\nu(i)\}^2 \tag{3.3}$$
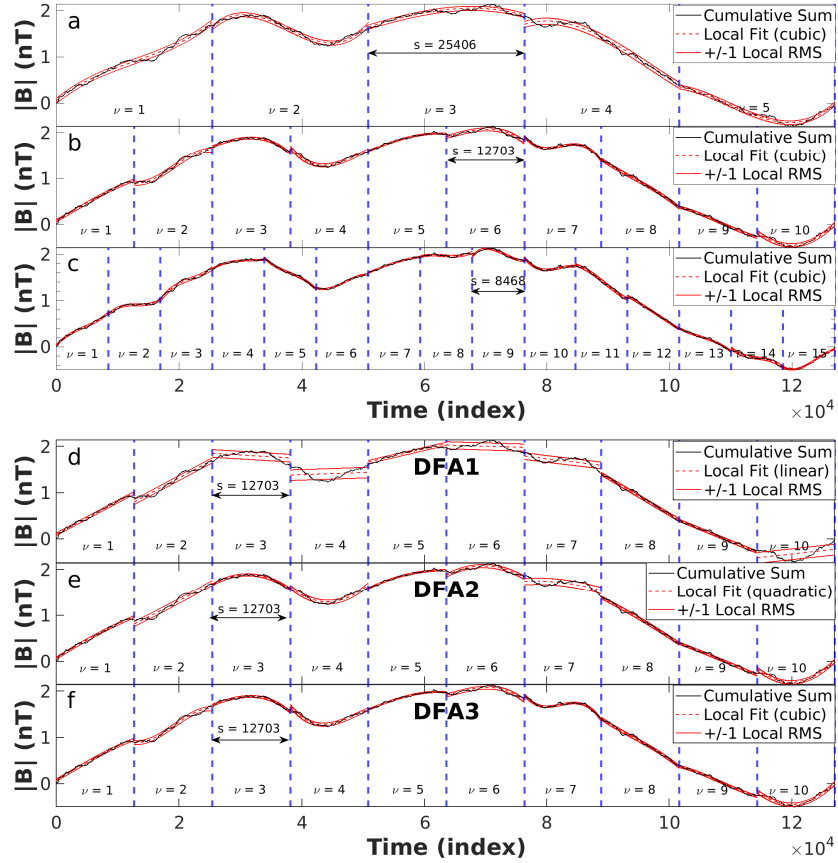
FIGURE 3.1 – Exemplification of steps 2 and 3 in DFA method for the time series of solar wind magnetic field of 2016 January 25. The upper figure (a, b, c) shows the series been divided into 5, 10 and 15 segments respectively of size s. For each ν segments, a cubic polynomial detrend is applied. The lower figure (d, e, f) shows the series been divided into 10 segments where a linear, quadratic and cubic polynomial detrend is applied at each segment. Source: produced by author.
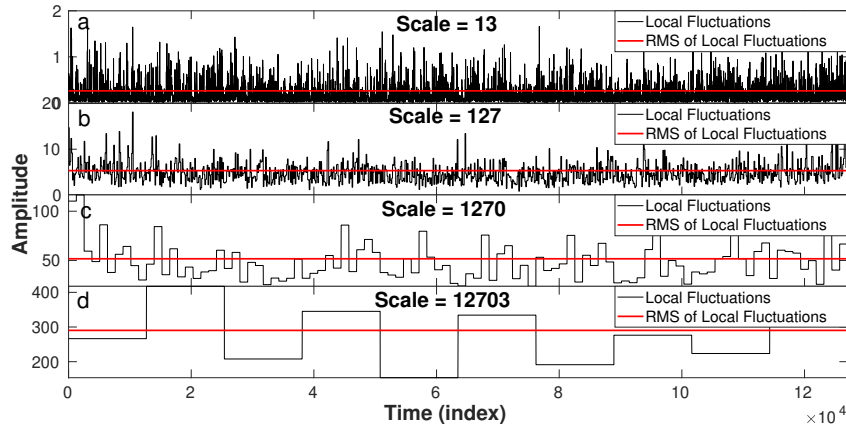
FIGURE 3.2 – Local Fluctuations for segments with scales of 13, 127,1270 and 12703 of $|B|$ 20016 January 25 time series. The red lines represent the overall RMS and are the fluctuation function of that scale. Source: produced by author.

for $\nu = N_s + 1, \ldots, 2N_s$, where y_ν is the m-th degree fitting polynomial of each segment ν (Fig. 3.1). This polynomial detrending of order m in the Y profile eliminates trends up to order $m - 1$ in the original time series and specifies the type of DFA applied.

At last, the fluctuation over all segments (Fig. 3.2) is:

$$F(s) = \left\{ \frac{1}{2N_s} \sum_{\nu=1}^{2N_s} [F^2(s,\nu)] \right\}^{\frac{1}{2}}. \tag{3.4}$$

$F(s)$ increases exponentialy and for large values of s it follows a power-law:

$$F(s) \propto s^H. \tag{3.5}$$

So, a log-log plot of fluctuation functions of the scale results in a linear fit with slope H (Fig. 3.3), the Hurst exponent (HURST *et al.*, 1965).
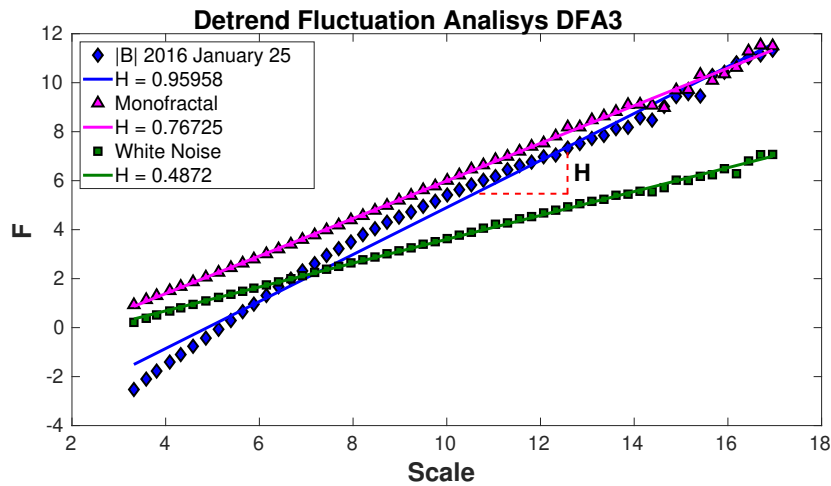
FIGURE 3.3 – Log-log plot of fluctuation functions of the scales and their corresponding regression lines for multifractal (January 25 $|B|$, blue), monofractal (magenta) and white noise (green) time series. The slope of the regression line represents the Hurst exponent. Source: produced by author.
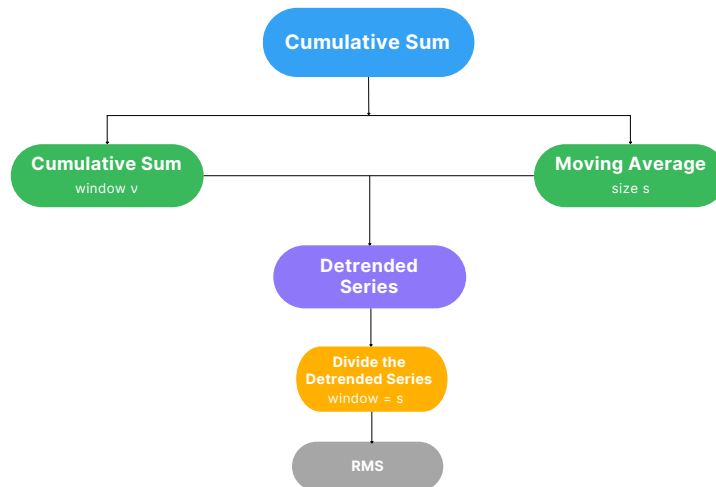
FIGURE 3.4 – Flowchart for DFA method. Source: produced by author.

3.2 Multifractal Detrended Fluctuation Analysis

The *Multifractal Detrended Fluctuation Analysis* (MF-DFA) method is a generalization of the DFA method quantifying long-range correlations at non-stationary time series (KANTELHARDT *et al.*, 2002). The method identifies the scaling of qth-order moments of the time series (NOROUZZADEH *et al.*, 2007). The MFDFA method has a wide range of applications in many different scientific fields working as a valuable tool for understanding the complexity and dynamics of various systems by studying their scaling exponents (NEELAKSHI *et al.*, 2020; NEELAKSHI *et al.*, 2022; BATISTA *et al.*, 2022). The method consists of five steps where the first three steps are the same of DFA method :

4. The average over all segments is calculated to obtain the qth-order fluctuation function (Fig. 3.5):

$$F_q(s) = \left\{ \frac{1}{2N_s} \sum_{\nu=1}^{2N_s} [F^2(s,\nu)]^{\frac{q}{2}} \right\}^{\frac{1}{q}}, \tag{3.6}$$

where, in general, the q parameter can take any real value except zero. For $q = 2$, the equation returns the DFA method. Steps 2 to 4 are repeated for different time scales s.

5. The scaling behavior of the fluctuation function is defined by the log-log plot of $F_q(s) \times s$ for each value of q (Fig. 3.6). If x_i have long-range correlations, for large values of s, $F_q(s)$ increases as a power-law,

$$F_q(s) \sim s^{H(q)}. \tag{3.7}$$

The scaling exponents $h(q)$ are the generalized Hurst exponents, defined as the slope of the $\log F_q(s) \times \log(s)$ graph (Fig. 3.6), where for $h(2)$ we have the standard Hurst Exponent (HURST *et al.*, 1965). For positive values of q, $h(q)$ describes the scaling behavior of segments with large fluctuations and for negative values of q, $h(q)$ describes the scaling behavior of segments with small fluctuations (Fig. 3.5). For monofractal series, $h(q)$ is independent of q but for multifractal series $h(q)$ depends on q (Fig. 3.6d). The generalized Hurst exponent is directly related to the Renyi exponent (RENYI, 1976), $\tau(q)$, (Fig. 3.7b) by

$$\tau(q) = qh(q) - 1. \tag{3.8}$$

Besides $h(q)$, another way to characterize the multifractality of a time series is by the
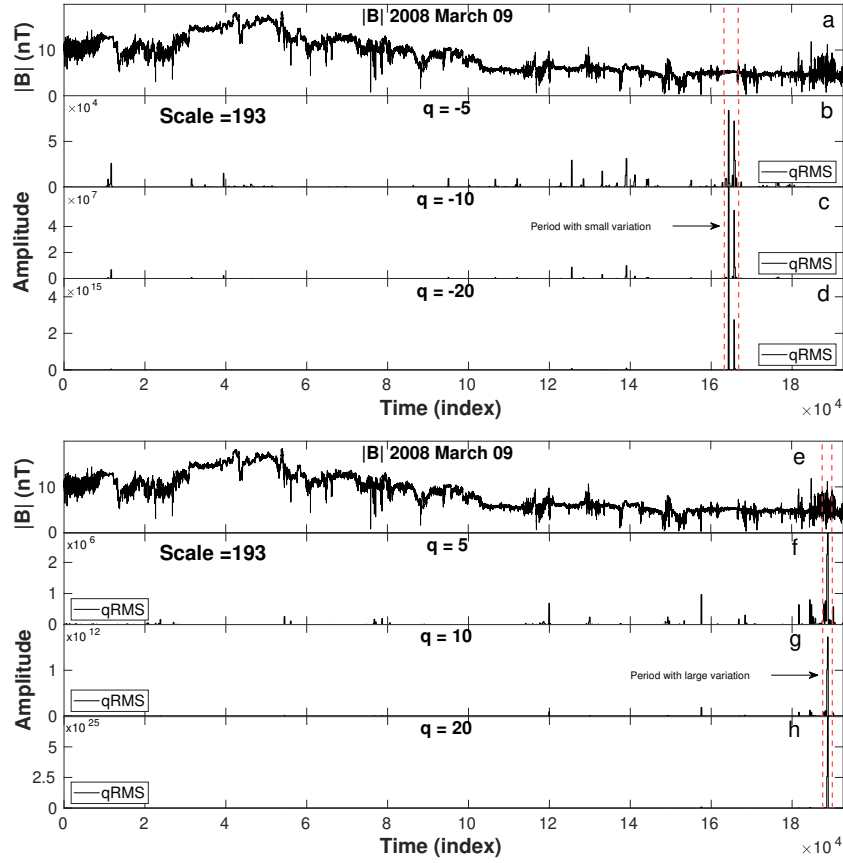
FIGURE 3.5 – Exemplification of step 4 in the MF-DFA method for the solar wind magnetic field of 2008 March 9 time series for a segment of scale size $s = 193$. The upper figure represents the q-order local fluctuations for negative q values and the lower figure shows the local fluctuations for positive q. Source: produced by author.
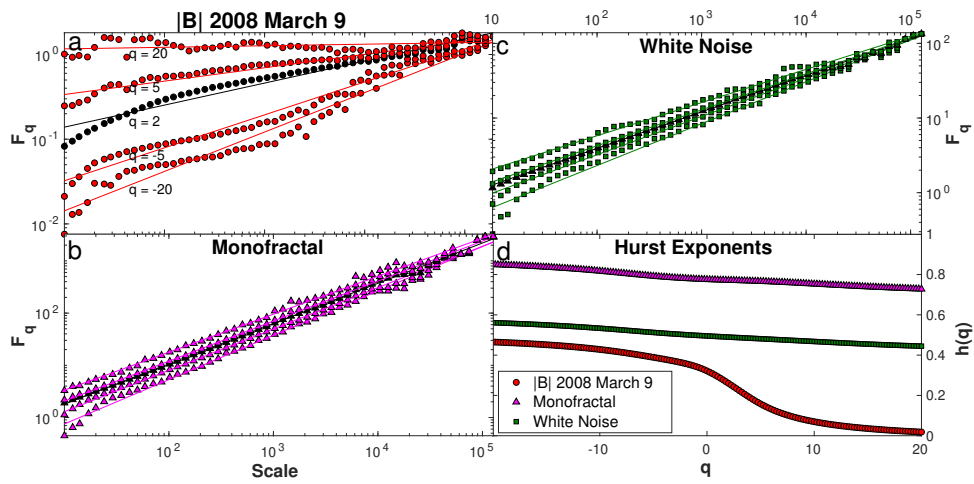
FIGURE 3.6 – (a, b, c) Fluctuation functions and their respective regressions lines for multifractal 2016 January 25 $|B|$ (blue), monofractal (magenta) and white noise (green) time series. The slopes regards to $q = -20, -5, 2(black), 5, 20$. (d) Generalized Hurst exponents for multifractal January 25 $|B|$ (blue), monofractal (magenta) and white noise (green). Source: produced by author.

singularity spectrum $f(\alpha)$, which is related to $\tau(q)$ via a Legendre transform,

$$\alpha = \tau'(q) \quad \text{and} \quad f(\alpha) = q\alpha - \tau(q), \tag{3.9}$$

where α is the singularity exponent and is related to $h(q)$ by

$$\alpha = h(q) - qh'(q) \quad \text{and} \quad f(\alpha) = q[\alpha - h(q)] + 1. \tag{3.10}$$
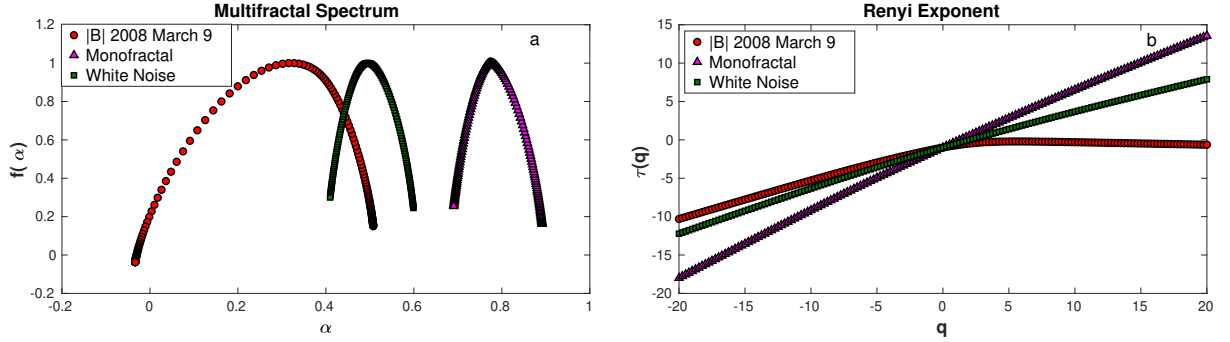
FIGURE 3.7 – (a) Multifractal spectrum for multifractal 2008 March 9 $|B|$ (blue), monofractal (magenta) and white noise (green) time series. (b) Renyi exponent for multifractal March 9 $|B|$ (blue), monofractal (magenta) and white noise (green) time series. Source: produced by author.

This $f(\alpha) \times \alpha$ relation (Fig. 3.7a) represents the multifractal spectrum and has a concave parabolic shape. The width of this downward parable in the α axis is a standard measure of multifractality and represents the multifractal strength.

From the multifractal spectrum it is possible to obtain a set of parameters to characterize each series (Fig. 3.8b): (i) the α value where $f(\alpha)$ is maximum, α_0; (ii) the α width, $\Delta\alpha = \alpha_{max} - \alpha_{min}$, where α_{min} and α_{max} are, respectively, the minimum and maximum values of α that mark the base of the concave parable in the multifractal spectrum ($\Delta\alpha$ is a measure of multifractal strength); (iii) the asymmetry parameter:

$$A = \frac{(\alpha_{max} - \alpha_0)}{(\alpha_0 - \alpha_{min})}, \tag{3.11}$$

where:

1. $A = 1$ means that the spectrum is symmetric,

2. for $A > 1$ the spectrum is right-skewed asymmetric and

3. for $A < 1$ the spectrum is left-skewed asymmetric (SHIMIZU *et al.*, 2002; FREITAS *et al.*, 2016; BATISTA *et al.*, 2022).

A multifractal spectrum with a long right tail has a greater contribution from small fluctuations. By contrast, a multifractal spectrum with left asymmetry has a greater influence by local fluctuations with large values (IHLEN, 2012) (Fig. 3.8b).

Another useful multifractal parameter can be extracted from the $\tau(q) \times q$ relation. As can be seen from Eq. (3.8), $\tau(q)$ has a linear dependence with q for monofractal series,
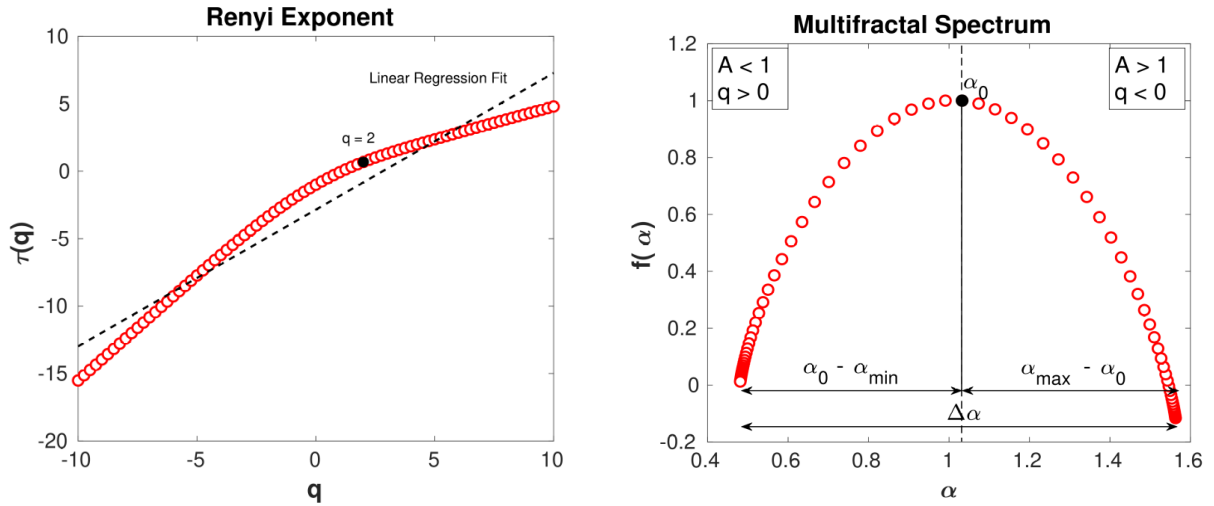
FIGURE 3.8 – (a) Renyi exponent for multifractal time series (red circles) and the linear regression (black). (d) Multifractal spectrum for multifractal time series (red circles). Source: produced by author.

where $h(q)$ is constant. In contrast, for multifractal series, this dependence is nonlinear. The q-dependency of the Renyi exponent can be quantified by the coefficient of determination, R^2 (Fig. 3.8a). R^2 measures the proportion of the variance for a dependent variable that is predictable by an independent variable in a linear regression model (BARRETT, 1974). The coefficient of determination is given by:

$$R^2 = 1 - \frac{\sum_{i=1}^{n}(y_i - \hat{y}_i)^2}{\sum_{i=1}^{n}(y_i - \bar{y}_i)^2}, \tag{3.12}$$

where y_i is the observed dependent variable, $\hat{y}_i$ is the corresponding predicted value and $\bar{y}_i$ is the mean of the observed data. R^2 varies from 0 to 1, where in our case 1 represents a perfect fit to the linear dependence model. In other words, the measure of R^2 for the $\tau(q) \times q$ relation will be closer to 0 for multifractal series and closer to 1 for monofractal series.

The MF-DFA method has best results if the time series has noise-like structure. Noise-like time series have a Hurst exponent h between 0.2 and 0.8. If the time series have random-walk structure, h has a value between 1.2 and 1.8. In the latter case, the time series must be differentiated to become noise-like (IHLEN, 2012). To identify if the time series has noise or random-walk structure, the h value can be obtained through the DFA method EKE *et al.* (2002) prior to application of MF-DFA method.

3.3   Detrended Moving Average

Beside the DFA, different methods were developed to quantify and qualify long-range correlations in nonstationary signals. VANDEWALLE; AUSLOOS (1998) proposed a new

technique based on the moving average method to detect trends in data, the so called *Detrended Moving Average* (DMA). This method follows the same points proposed by DFA but now considering the contribution coming from "past" and "future" points, according to which moving average model is applied. ALESSIO *et al.* (2002), CARBONE *et al.* (2004), XU *et al.* (2005) and ALVAREZ-RAMIREZ *et al.* (2005) first defined two possible analysing conditions based on moving average calculation:

1. *Backward Moving Average* (BDMA). Considering a window of size n, the backward moving average is given by:

$$\tilde{y}(i) = \frac{1}{n} \sum_{k=0}^{n-1} y(i - k).$$ (3.13)

This means that $\tilde{y}$ refers to the average value of y for the last n data points (VAN-DEWALLE; AUSLOOS, 1998) (see Figure 3.9).

2. *Centered Moving Average* (CDMA). Also considering a window of size n, the average of the data inside the window is located at the center of this window (Fig. 3.9) and given by:

$$\tilde{y}(i) = \frac{1}{n} \sum_{k=-[(n-1)/2]+1}^{n/2} y(i - k)$$ (3.14)

where $y(i)$ is the integrated time series:

$$y(i) = \sum_{k=1}^{i} [x_k - \langle x \rangle], \qquad i = 1, ..., N.$$ (3.15)
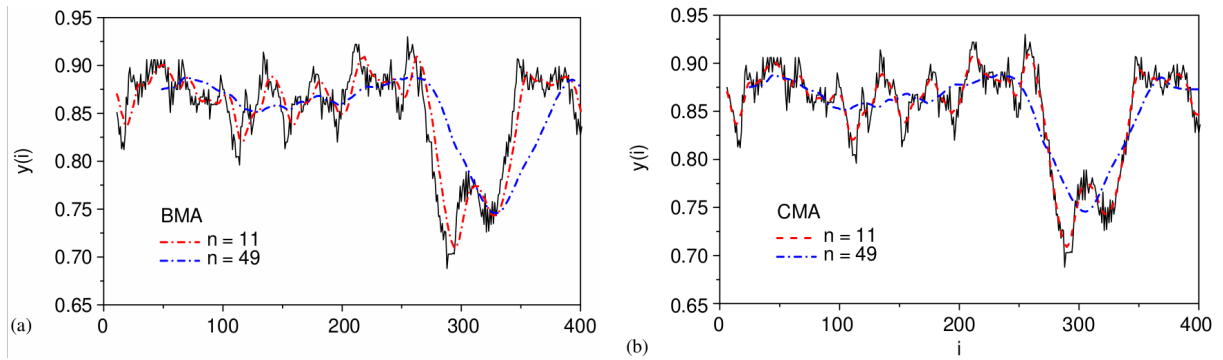
FIGURE 3.9 – Exemplification of (a) backward moving average and (c) centered moving average for two values of window size n. Source: (ALVAREZ-RAMIREZ *et al.*, 2005)

After defining the moving average method type used, the following steps are the same implemented for DFA. So, the fluctuation for n is defined as

$$F_{BDMA}(n) = \sqrt{\frac{1}{N-n+1} \sum_{i=n}^{N} [y(i) - \tilde{y}(i)]^2}, \qquad (3.16)$$

for BDMA and for CDMA:

$$F_{CDMA}(n) = \sqrt{\frac{1}{N-n+1} \sum_{i=[(n-1)/2]}^{N-[n/2]} [y(i) - \tilde{y}(i)]^2}. \qquad (3.17)$$

As well as the DFA method, $F_{DMA}(n) \times n$ relation follows a power-law:

$$F_{DMA}(n) \propto n^H. \qquad (3.18)$$
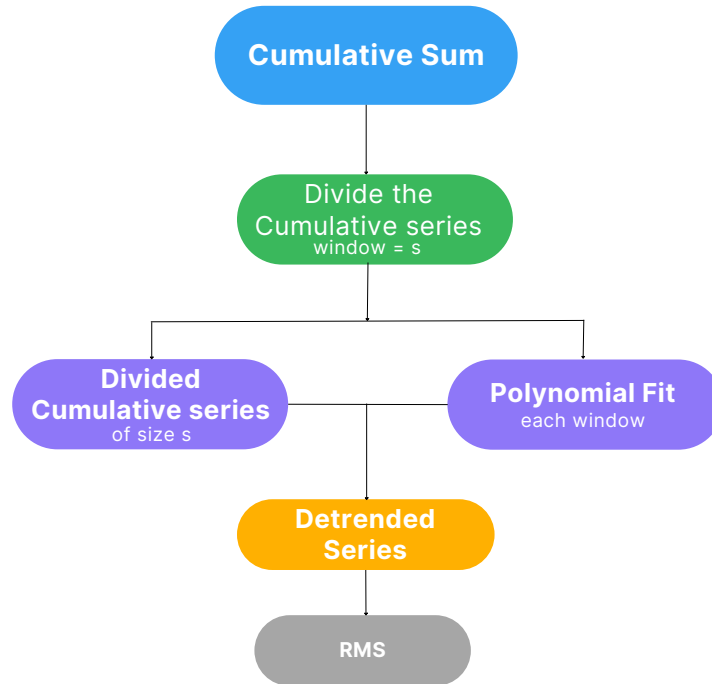
FIGURE 3.10 – Flowchart for DMA method. Source: produced by author.

3.4   Multifractal Detrended Moving Average

Following the same concept of the DFA generalization proposed by KANTELHARDT *et al.* (2002), GU; ZHOU (2010) extended the DMA method to investigate multifracal time series and multifractal surfaces. The *Multifractal Detrended Moving Average* (MF-DMA)

method is also consisted of a few steps, but first it is required to define a moving average parameter called θ.

The position parameter θ varies inside the $[0, 1]$ range, where:

1. $\theta = 0$ considers the *backward moving average* (BMA)(XU *et al.*, 2005; ALVAREZ-RAMIREZ *et al.*, 2005), i.e., $\tilde{y}$ is measured for $n - 1$ points in the "past";

2. $\theta = 0.5$ refers to the *centered moving average* (CMA), which considers past and future data points in the n window;

3. $\theta = 1$ selects the *forward moving average* (FMA) (GU; ZHOU, 2010), i.e., $\tilde{y}$ is calculated for $n - 1$ data in the "future".

So, the moving average function $\tilde{y}$ is now defined as

$$\tilde{y}(i) = \frac{1}{n} \sum_{k=-\lfloor (n-1)\theta \rfloor}^{\lceil (n-1)(1-\theta) \rceil} y(i - k), \tag{3.19}$$

with $\lceil (n - 1)(1 - \theta) \rceil$ data in the past and $\lfloor (n - 1)\theta \rfloor$ in the future, where $\lfloor (...) \rfloor$ means the largest integer not greater than $(...)$ and $\lceil (...) \rceil$ means the smallest integer not smallest than $(...)$.

After this definition, the process continues with the following steps:

1. The detrended signal $\epsilon(i)$ is obtained by removing $\tilde{y}$ from the integrated series $y(i)$

$$\epsilon(i) = y(i) - \tilde{y}(i) \tag{3.20}$$

where $n - \lfloor (n - 1)\theta \rfloor \leq i \leq N - \lfloor (n - 1)\theta \rfloor$

2. the residual $\epsilon(i)$ is divided into $N_n = \lfloor N/n - 1 \rfloor$ segments ϵ_v of size n. Thus, the root mean squared for each segment v i given by

$$F_v^2(n) = \frac{1}{n} \sum_{i=1}^{n} [\epsilon_v(i)]^2 \tag{3.21}$$

3. The average over all segments is calculated to obtain the qth-order fluctuation function:

$$F_q(n) = \left\{ \frac{1}{N_n} \sum_{v=1}^{N_n} [\epsilon_v(i)]^q \right\}^{\frac{1}{q}} \tag{3.22}$$

where for $q = 0$, as indicated by L'Hôpital rule, F_q is given by

$$\ln[F_0(n)] = \frac{1}{N_n} \sum_{v=1}^{N_n} \ln[F_v(n)] \tag{3.23}$$

4. Likewise at the MF-DFA case, the fluctuation function $F_q(n)$ increases as a power-law in relation with n

$$F_q(n) \sim n^{H(q)}. \tag{3.24}$$

3.4.1 Two-Dimensional Multifractal Detrended Moving Average

As we can apply the MF-DFA and MF-DMA methods to observe the multifractality of a time series, it is also possible to use these tools to a surface analysis (GU; ZHOU, 2010). By considering an area as a two-dimensional matrix $X(i_1, i_2)$ where $i_1 = 1, 2, ...N_1$ and $i_2 = 1, 2, ...N_2$, we apply the 2D-MFDMA by the following six steps:

1. The surface $X(i_1, i_2)$ is integrated in a sliding window of size $n_1 \times n_2$, with $n_1 \leq i_1 \leq N_1 - \lfloor (n_1 - 1)\theta_1 \rfloor$ and $n_2 \leq i_2 \leq N_2 - \lfloor (n_2 - 1)\theta_2 \rfloor$. This means, we obtain from matrix X a smaller matrix $Z(u_1, u_2)$ of size $n_1 \times n_2$, where $i_1 - n_1 \leq u_1 \leq i_1$ and $i_2 - n_2 \leq u_2 \leq i_2$. From this submatrix, the sum $Y(i_1, i_2)$ is:

$$Y(i_1, i_2) = \sum_{j_1=1}^{n_1} \sum_{j_2=1}^{n_2} Z(j_1, j_2). \tag{3.25}$$

2. The moving average function $\widetilde{Y}(i_1, i_2)$ is calculated, considering $n_1 \times n_2$, with $n_1 \leq i_1 \leq N_1 - \lfloor (n_1 - 1)\theta_1 \rfloor$ and $n_2 \leq i_2 \leq N_2 - \lfloor (n_2 - 1)\theta_2 \rfloor$. After that, we obtain from X the submatrix $W(k_1, k_2)$, where $n_1 - \lceil (n_1 - 1)\theta_1 \rceil \leq k_1 \leq k_1 + \lfloor (n_1 - 1)\theta_1 \rfloor$ and $n_2 - \lceil (n_2 - 1)\theta_2 \rceil \leq k_2 \leq k_2 + \lfloor (n_2 - 1)\theta_2 \rfloor$. The cumulative sum $\widetilde{W}(m_1, m_2)$ is

$$\widetilde{W}(m_1, m_2) = \sum_{d_1=1}^{m_1} \sum_{d_2=1}^{m_2} W(d_1, d_2) \tag{3.26}$$

where $1 \leq m_1 \leq n_1$ and $1 \leq m_2 \leq n_2$. The moving average function $\widetilde{Y}(i_1, i_2)$ is

$$\widetilde{Y}(i_1, i_2) = \frac{1}{n_1 n_2} \sum_{m_1=1}^{n_1} \sum_{m_2=1}^{n_2} \widetilde{W}(m_1, m_2) \tag{3.27}$$

3. Remove the moving average function $\widetilde{Y}(i_1, i_2)$ from $Y(i_1, i_2)$ to obtain the detrended

matrix $\epsilon(i_1, i_2)$

$$\epsilon(i_1, i_2) = Y(i_1, i_2) - \widetilde{Y}(i_1, i_2) \tag{3.28}$$

where $n_1 \leq i_1 \leq N_1 - \lfloor(n_1 - 1)\theta_1\rfloor$ and $n_2 \leq i_2 \leq N_2 - \lfloor(n_2 - 1)\theta_2\rfloor$.

4. The detrended matrix $\epsilon(i_1, i_2)$ divided into $N_{n_1} \times N_{n_1}$ matrices of size $n_1 \times n_2$, where $N_{n_1} = \lfloor(N_1 - n_1(1 + \theta_1))/n_1\rfloor$ and $N_{n_2} = \lfloor(N_2 - n_2(1 + \theta_2))/n_2\rfloor$. The submatrices are so defined as $\epsilon_{v_1,v_2}(i_1, i_2) = \epsilon(l_1 + i_1, l_2 + i_2)$ where $1 \leq i_1 \leq n_1$, $1 \leq i_2 \leq n_2$, $l_1 = (v_1 - 1)n_1$ and $l_2 = (v_2 - 1)n_2$. So, the detrended fluctuation function $F_{v_1,v_2}(n_1, n_2)$ for each segment is:

$$F_{v_1,v_2}^2(n_1, n_2) = \frac{1}{n_1 n_2} \sum_{i_1=1}^{n_1} \sum_{i_2=1}^{n_2} \epsilon^2(i_1, i_2) \tag{3.29}$$

5. We calculate the qth-order fluctuation function:

$$F_q(n_1, n_2) = \left\{ \frac{1}{N_{n_1} N_{n_2}} \sum_{v_1=1}^{N_{n_1}} \sum_{v_2=1}^{N_{n_2}} F_{v_1,v_2}^q(n_1, n_2) \right\}^{1/q} \tag{3.30}$$

where q is a non-zero real number.

6. Let $n^2 = \frac{1}{2}(n_1^2 + n_2^2)$. For different values of n, F_q increases as a power-law:

$$F_q \sim n^{h(q)}. \tag{3.31}$$

For this work, we use the same set of parameters defined in GU; ZHOU (2010) ($n = n_1 = n_2$ and $\theta = \theta_1 = \theta_2$). Applying the multifractal formalism, the following parameters are also defined: the Renyi exponent (RENYI, 1976), the singularity exponent α and the singularity spectrum $f(\alpha)$.

$$\tau(q) = q\,h(q) - D_f. \tag{3.32}$$

where D_f is the fractal dimension, e.g., for our scenario, $D_f = 2$. Subsequently, via Legendre transform, it is possible to obtain the α and $f(\alpha)$ parameters:

$$\alpha = \tau'(q) \quad \text{and} \quad f(\alpha) = q\,\alpha - \tau(q), \tag{3.33}$$

3.5   Surrogate Time Series

According to MADANCHI *et al.* (2017), there are two features in a time series that can lead to its multifractality: (i) the presence of heavy-tailed probability density functions (PDFs), and (ii) the existence of linear and non-linear correlations. In this section, we try to identify the origin of the multifractality in the solar wind by means of two surrogate time series derived from the original $|B|$ data. As mentioned in the introduction, the shuffled time series is a random permutation of the original time series in the real space that destroys all temporal correlations, while keeping the same PDF for the amplitudes of $|B|$ (Fig. 3.11). On the other hand, the random phases surrogate is generated from the Fourier Transform of the original $|B|$ series. A new Fourier series is generated by shuffling the phases of the Fourier modes while keeping their power spectrum (KOGA *et al.*, 2008; MAIWALD *et al.*, 2008). The inverse Fourier transform of this new frequency spectrum is the random phases surrogate, which keeps the power spectrum and linear autocorrelation of the original series, but has a Gaussian PDF and breaks the nonlinear correlations (Fig. 3.11). After generating these two surrogates, we repeat the multifractal analysis described in the previous section; if the shuffled surrogate has a multifractal spectrum that is considerably narrower than the spectrum of the original series, it means that time correlations are an important source of multifractality in the original time series, otherwise, fat-tailed PDFs are the main source of multifractality. If the random phases surrogate has a multifractal spectrum that is considerably narrower than the spectrum of the original series, it means that fat-tailed PDFs and/or nonlinear correlations are important for the multifractality. Note that both kinds of multifractality mentioned above can be present in a time series (NOROUZZADEH *et al.*, 2007; MADANCHI *et al.*, 2017). If both the shuffled and random phases surrogates produce monofractal spectra, then nonlinear correlations (but not fat-tailed PDFs) are the source of multifractality.
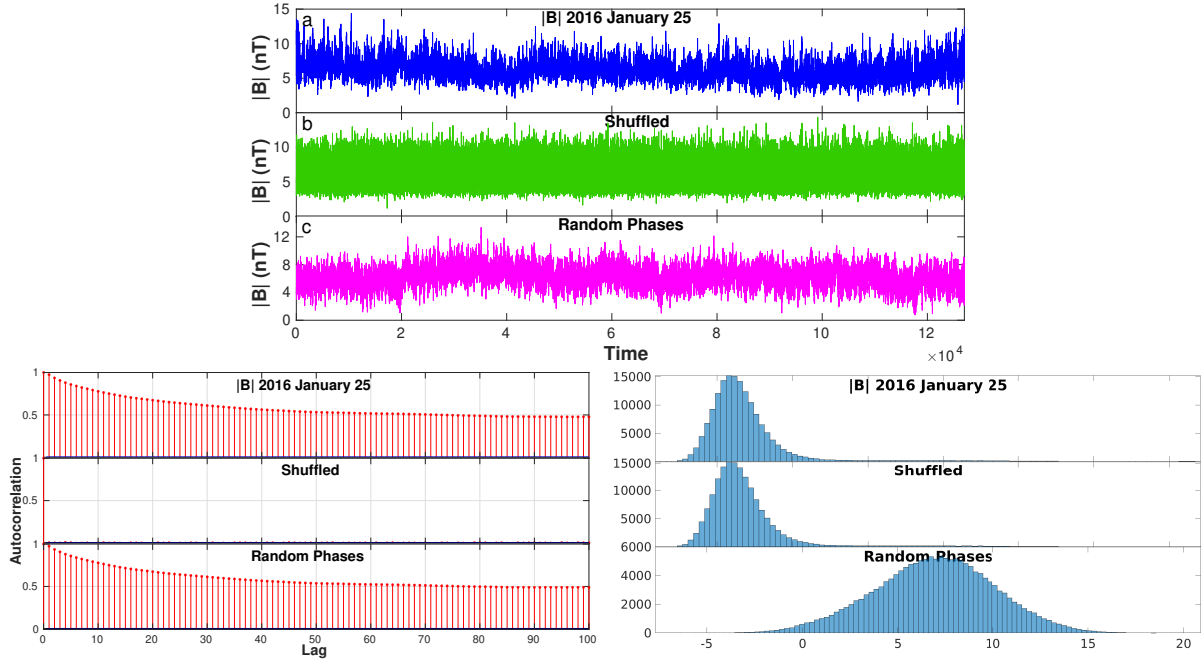
FIGURE 3.11 – Upper: Solar wind time series of |B| for 2016 January 25 (blue) and the respective surrogates: shuffled (green), and random phases (magenta). Lower-Left: Autocorrelation plot of original time series and respective surrogates. Lower-Right: Histogram of original time series and respective surrogates. Source: produced by author.

3.6   Zeta Function

Another function typically employed in multifractal analyses of time series is the zeta function. Consider the structure function for |B| (FRISCH, 1995):

$$S_p(\tau) = \langle [|B(t+\tau)| - |B(t)|]^p \rangle \tag{3.34}$$

where $\langle \cdot \rangle$ is the time average, τ is the time lag and p are the statistical moments for the time series of B. Assuming scale invariance inside the inertial range, S_p follows a power law

$$S_p(\tau) \sim \tau^{\zeta(p)} \tag{3.35}$$

where $\zeta(\cdot)$ is the zeta function or scaling exponent. So, $\zeta(p)$ is obtain by the slope of the $\log S_p(\tau) \times \log \tau$ plot. The importance of this parameter comes from the Kolmogorov's K41 theory (KOLMOGOROV, 1941) and the IK (Iroshnikov-Kraichnan) theory (IROSHNIKOV, 1964; KRAICHNAN, 1965) of self-similarity and scale invariance inside the inertial range for a homogeneous and isotropic turbulence, where the ζ function was shown to be a linear function of p, with $\zeta(p) = p/3$ for K41 and $\zeta(p) = p/4$ for IK.
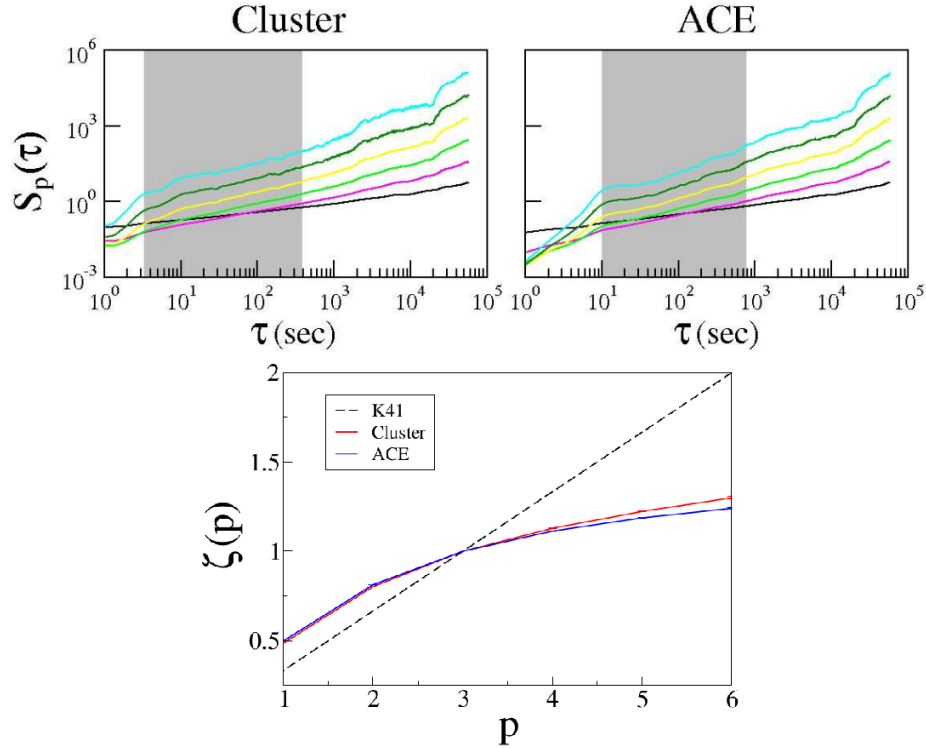
FIGURE 3.12 – Upper: Structure functions from the magnetic field fluctuations of satelittes Cluster-1 and ACE with: p=1 (black), 2 (purple), 3 (light green), 4 (yellow), 5 (dark green) and 6 (light blue). The grey interval indicates the inertial range. Lower: Zeta functions from the magnetic field fluctuations of satelittes Cluster-1 (red) and ACE (blue). The dashed lines represent the Kolmogorov K41 scaling. Source: (CHIAN; MIRANDA, 2009)

3.7 p-model

The $p-$model is a model for non-homogeneous energy-cascading process in the inertial range of fully-developed turbulence (KOLMOGOROV, 1941; FRISCH, 1995), based on the generalized Cantor set. Consider that the flux of kinetic energy from eddies of size L to smaller eddies is represented by a dissipation E_L. In the one-dimensional version of the $p-$model, L is the length of an interval. Suppose that an eddy of size L is unequally divided into two smaller eddies (i.e., two sub-intervals) of sizes $l_1 L$ and $l_2 L$, where $0 < l_1 < l_2 < 1$ are the size factors, with the flux of energy E_L being distributed unto these sub-eddies with different probabilities p_1 and p_2, i.e., the new dissipation values are $p_1 E_L$ and $p_2 E_L$. In practice, one can start the process with $L = E_L = 1$. Then, each new eddy is further sub-divided into two smaller eddies with the same size factors l_1 and l_2 and probabilities p_1 and p_2. This process may be repeated until the sub-intervals reach the Kolmogorov dissipation scale Fig. 3.13. At each cascading step n, there will be $\begin{pmatrix} n \\ m \end{pmatrix}$ segments with length $l_1^m l_2^{n-m} L$ and dissipation $p_1^m p_2^{n-m} E_L$, for $m = 0, 1, \ldots, n$.
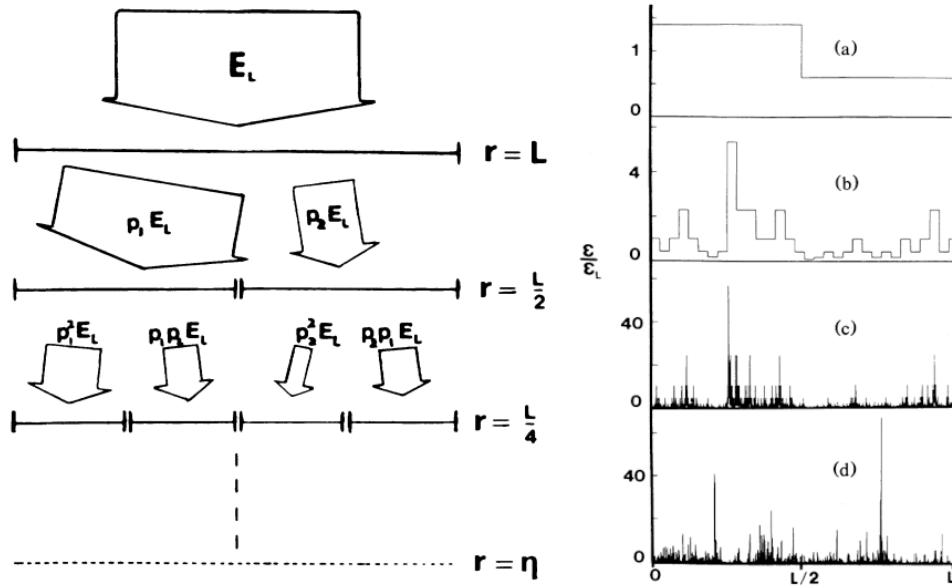
FIGURE 3.13 – Left: One-dimensional schematic of a cascade model where each eddie split into to two new ones. Right: Different stages of the p-model time series (a. first, b. fifth, c. twelfth stage and d. is an experimental signal). Source: (MENEVEAU; SREENIVASAN, 1987)

As shown by HALSEY et $al.$ (1986) for the general two-scale Cantor set, it is possible to obtain the analytic expressions for the singularity exponent α and the singularity spectrum f as:

$$\alpha = \frac{\ln p_1 + (n/m - 1)\ln p_2}{\ln l_1 + (n/m - 1)\ln l_2}, \tag{3.36}$$

$$f = \frac{(n/m - 1)\ln(n/m - 1) - (n/m)\ln(n/m)}{\ln l_1 + (n/m - 1)\ln l_2}. \tag{3.37}$$
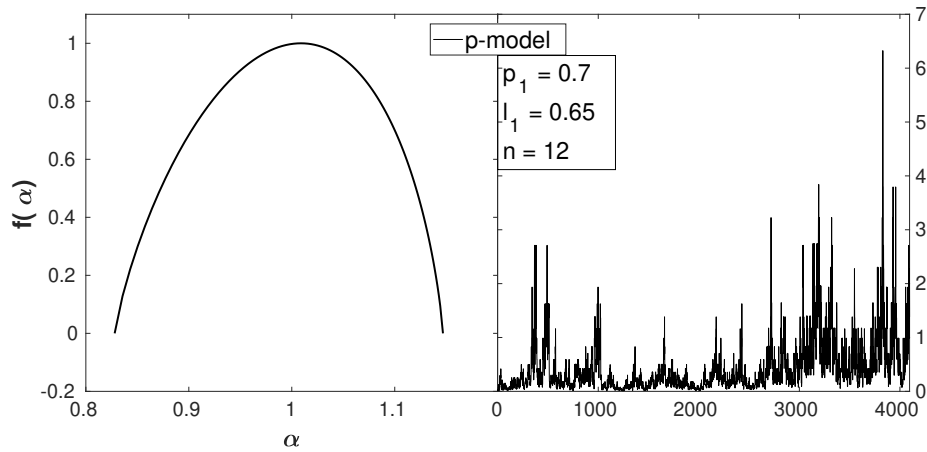
FIGURE 3.14 – Left: Analytical multifractal spectrum generated using p-model ($p_1 = 0.7$, $l_1 = 0.65$). Right: p-model time series generated from multifractal spectrum parameters by 12th iteration. Source: produced by author.

For each n and given values of l_1, l_2, p_1 and p_2, the variation of m will provide the different values of α and f for the singularity spectrum Fig. 3.14. Since $0 \leq m \leq n$ and m is an integer, larger values of n provide a better definition of the spectrum. For a cascading process with direct energy dissipation in the inertial range, we have $p_1 + p2 < 1$ (MENEVEAU; SREENIVASAN, 1987). This means that a new dp dissipation parameter must be included, where $dp = 1 - p_1 - p_2$. Thus, we define $p_2 = 1 - p_1 - dp$, as well as $l_2 = 1 - l_1$, in Eqs. (3.36) and (3.37).

By obtaining a $p-$model fit of the singularity spectrum of the time series, it is possible to define the probabilities and size factors related to the series and, from those parameters, to generate a multifractal time series (NEELAKSHI *et al.*, 2020; NEELAKSHI, 2020), Fig. 3.14.

3.8 Integrated Averaged Current Deviation

3.8.1 Vortex Detection

In two-dimensional fields, vortices are one of the typical coherent structures used to describe turbulence, and several mathematical methods have been proposed to detect them objectively. Objectivity or "*frame-indifference*" can be defined as the invariance of time-dependent variables under a change of frame or observer (TRUESDELL *et al.*, 2004). This definition of objectivity is crucial to develop methods of detecting vortex structures, which are known as area flows with observer invariance. However, most of the vortex detecting methods are not objective so, to define and identify coherent vortices objectively, HALLER *et al.* (2016) presented an efficient method called *Lagrangian Averaged Vorticity Deviation*, LAVD. This method defines a spatial domain U which contains a velocity field $\mathbf{u}$ and a fluid particle at the initial position $\mathbf{x}(t_0) = \mathbf{x}_0$ that follows a trajectory given by:

$$\frac{\mathrm{d}\mathbf{x}}{\mathrm{d}t} = \mathbf{u}(\mathbf{x}, t), \quad \mathbf{x}(t_0) = \mathbf{x}_0 \tag{3.38}$$

The LAVD of the trajectory of $\mathbf{x}_0$ is defined as

$$LAVD_{t_0}^{t_0+\tau}(\boldsymbol{x}_0) = \int_{t_0}^{t_0+\tau} |\boldsymbol{\omega}(\boldsymbol{x}(t), t) - \langle \boldsymbol{\omega}(t) \rangle| \, dt, \tag{3.39}$$

where $\boldsymbol{\omega} = \nabla \times \boldsymbol{u}$ is the vorticity, $\langle \cdot \rangle$ is the spatial average and τ is a time interval. The vorticity mean deviation $|\boldsymbol{\omega}(\boldsymbol{x}(t), t) - \langle \boldsymbol{\omega}(t) \rangle|$ is invariant under a referential change. So, a coherent lagrangian vortex is an evolving material region $\mathcal{V}_L(t)$ where $\mathcal{V}_L(t_0)$ is filled with a set of level curves of $LAVD_{t_0}^{t_0+\tau}(\boldsymbol{x})$ with outward-decreasing LAVD values (REMPEL *et al.*, 2019).

Now, with the focus on magnetic vortex detection, (REMPEL *et al.*, 2016) proposed a variation of the LAVD operator for magnetic fields. Define $\boldsymbol{x}(s)$ as the position vector on a magnetic field line at t_0, where s is a parameter related with a distance l over a field line by $dl = |\boldsymbol{B}|ds$. So, at time t_0, the field-line equation is given by (SONSRETTEE *et al.*, 2014)

$$\frac{\mathrm{d}\boldsymbol{x}}{\mathrm{d}s} = \boldsymbol{B}(\boldsymbol{x}(s), t_0), \quad \boldsymbol{x}(s_0) = \boldsymbol{x}_0. \tag{3.40}$$

Then, replacing $\boldsymbol{\omega} = \nabla \times \boldsymbol{u}$ in LAVD equation by the current density $\boldsymbol{J} = \nabla \times \boldsymbol{B}/\mu_0$, the *Integrated Averaged Current Deviation*, IACD, is defined as

$$IACD_{s_0}^{s_0+\xi}(\boldsymbol{x}_0) = \int_{s_0}^{s_0+\xi} |\boldsymbol{J}(\boldsymbol{x}(s), t_0) - \langle \boldsymbol{J}(t_0) \rangle| \, dt, \tag{3.41}$$

where $\langle \boldsymbol{J}(t_0) \rangle$ is the mean current density. From this definition, it is possible to obtain two important method aspects. First, just like the LAVD, the IACD is an objective quantity but distinctly from the original tool, the IACD calculation is done for a fixed time. This means that the parameter interval is now given by $[s_0, s_0 + \xi]$ and likewise the LAVD, the magnetic vortex is expressed as a domain $\mathcal{V}_L(t_0)$ filled with level curves of set $IACD_{s_0}^{s_0+\xi}$ with outward decreasing IACD values; the $\mathcal{V}_L(t_0)$ border is the farthest convex level curves in $\mathcal{V}_L(t_0)$. So, basically the detection of the magnetic vortices comes from the IACD field calculation on the plane, finding the initial positions of these vortex centers as IACD local peaks and then, finding vortex edges as external convex closed contours of IACD surrounding the vortex center, as illustrated in Figure 3.15.
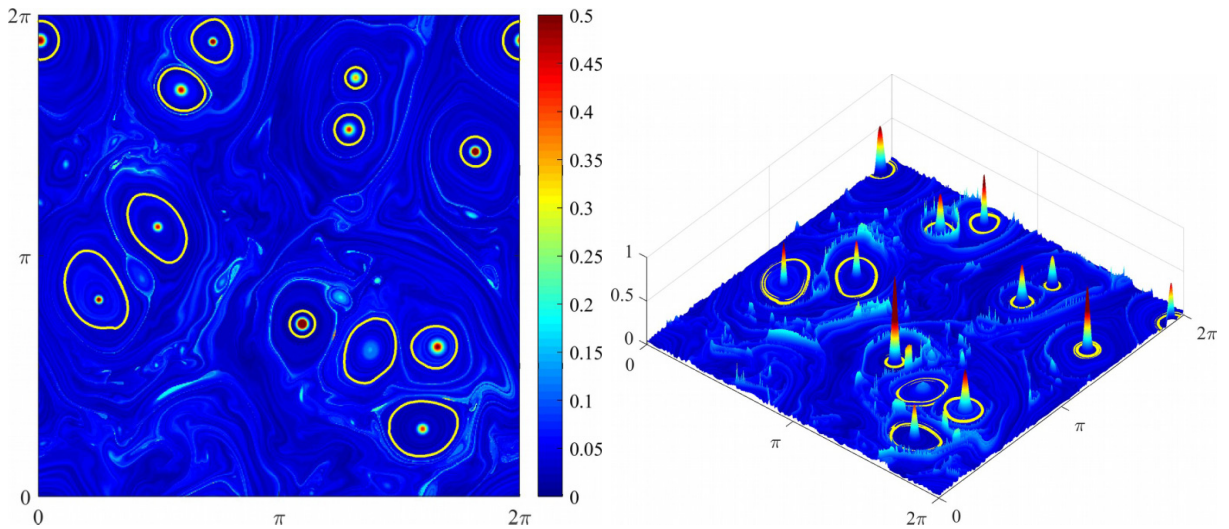
FIGURE 3.15 – Exemplification of objective magnetic vortices (IACD) using the Wu-Chang MHD model of magnetotail. Source (REMPEL *et al.*, 2019)

4 Results

In the present chapter we introduce the data that we investigated through multifractal analysis and so report the obtained results for two problems. First, we investigate the multifractality of two solar wind magnetic field time series and their respective volatilities, with the goal of understanding the origin of the multifractality. Thereafter, we apply the multifractal analysis to a series of magnetograms of an intense active region, and also apply a method of vortex detection to this AR with the purpose of confirming the influence of this kind of structure to the turbulence of the photosphere.

4.1 Solar Wind Data

We analyze solar wind magnetic field data detected with the Fluxgate Magnetometer (FGM) onboard Cluster-1. The Cluster mission is a group of four identical spacecraft placed in a tetrahedral formation launched in 2000 by the European Space Agency (ESA). During intervals when the spacecraft was near the Earth's bow shock and outside the Earth's magnetosphere, we selected several 22 Hz time series of the magnetic field magnitude[1]. In this work, two time series with 24 hours are investigated[2]), one from 2008 March 9 (Fig. 4.1a) and one from 2016 January 25 (Fig. 4.1b). Both days are at downward regions of solar activity of their respective solar cycles (SC23 for March 9 and SC24 for January 25) but with a more intense flare activity related to January 25 (4 B-Class, 2 C-Class flares, $F_{10.7} = 107.6$ stu and $V_{max} = 539$ km/s) if compared with March 9 (just 1 A-Class flare, $F_{10.7} = 69.5$ stu and $V_{max} = 691$ km/s). For illustration and completeness, Figure 4.2 provides an overview of the vector magnetic field components (B_x, B_y, B_z) and the electron velocity $V(e-)$ parameters for this interval. To reduce the computational time of the analysis, the data length has been reduced by using a decimation process[3]. The low-pass Chebychev Type I infinite impulse response filter was used with a reduction factor $M = 10$, order 8 and $0.8/M$ cut-off frequency.

---

[1] https://www.cosmos.esa.int/web/csa

[2] In addition, as supplementary material to (BATISTA et al., 2022), we also analyzed two other time series (Annex - A.2.

[3] The decimation method is described in (GOMES, 2018; GOMES et al., 2019).
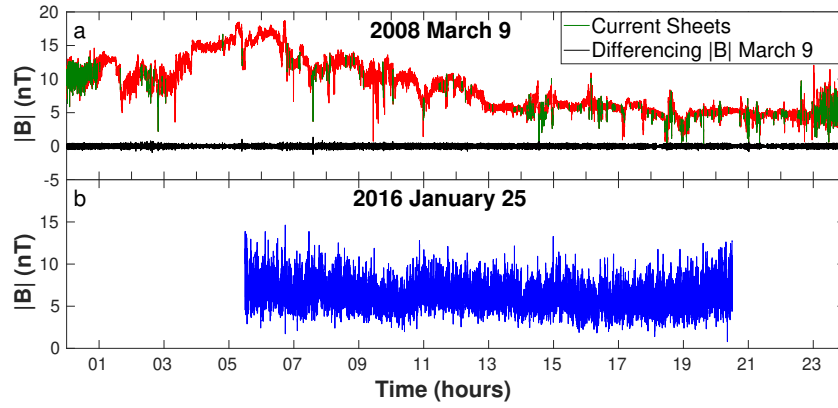
FIGURE 4.1 – Solar wind time series of $|B|$ measured by Cluster-1. (a) For 2008 March 9 (red), containing current sheets (green), and its first order differencing (black); (b) time series of $|B|$ for 2016 January 25 (blue), without current sheets. Source: (BATISTA et $al.$, 2022)
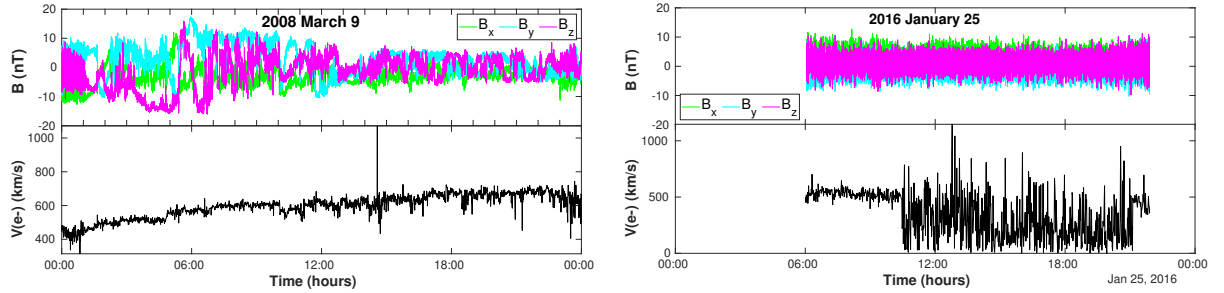
FIGURE 4.2 – Solar wind time series of the vector magnetic field (B_x, B_y, B_z) and the electron velocity measured by Cluster-1 for 2008 March 9 (left) and for 2016 January 25 (right).

After decimating the time series, we apply the MF-DFA method with four input parameters: minimum scale s_i, maximum scale s_f, order of fluctuation function q and polynomial order m. The scale refers to multiple segment sizes of the cumulative series and varies from a minimum segment size s_i to a maximum s_f. In this work, we use $s_i = 10$ and $s_f = N$, where N is the length of the time series; q varies between -20 and 20 with an increment of $\Delta q = 0.25$, and $m = 3$. This choice of parameters was supported by several tests. The recommendation for large time series is to use a polynomial trend order around $m = 3$; $s_f = N$ was chosen to avoid deformations in the shape of the multifractal spectra. Meanwhile, for the q parameter the use of values larger than 20 does not change the shape of the spectra significantly.

As it was explained in section 2.3.1, time-differencing is necessary in the case of 2008 March 9 due to the high nonstationarity of this series. Throughout the remaining of this section, only the differenced time series will be used for March 9. This time series was characterized by GOMES et $al.$ (2019) as being permeated by large-scale current sheets. The green regions in the original time series denote current sheets found with Li's method (LI, 2007) (section 2.1.3). We apply the same parameters from (GOMES et $al.$, 2019): $\theta = 60°$,

$L = 60\%$ and $\tau = 120$ s. The time series for 2016 January 25 is characterized by a higher degree of stationarity and the absence of current sheets (GOMES *et al.*, 2019). Due to its higher stationarity, there is no need to perform a differencing in this series.

4.1.1 Volatility

As mentioned in section 2.1.3, the presence of current sheets is associated with abrupt changes in the magnetic field. These abrupt changes are reflected in the time series formed by two-point differences, $\delta B(t) = |B(t + \tau)| - |B(t)|$, for a given time-scale τ (CHIAN; MIRANDA, 2009). With the objective of enhancing these bursts in the original time series, we implement a new quantity, which in econophysics is called *volatility* (POON, 2005). *Volatility* can be defined as the conditional standard deviations at specific series periods of the underlying asset return (or log return) (TSAY, 2010).
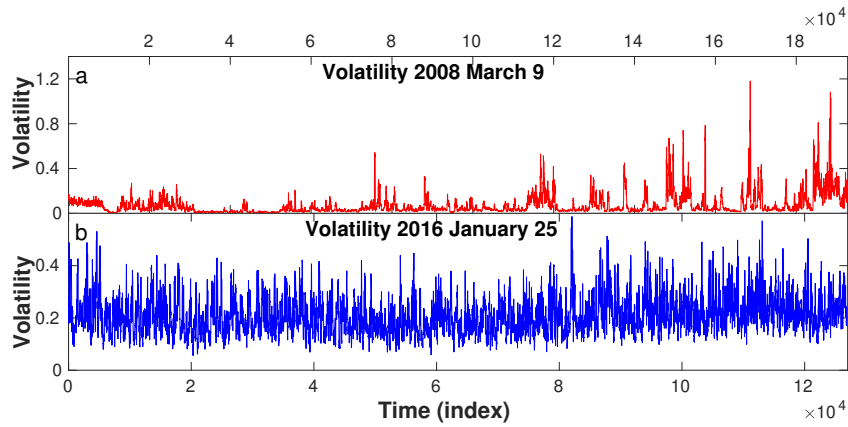
FIGURE 4.3 – Volatility of solar wind magnetic field time series for (a) 2008 March 9, and (b) 2016 January 25. Source: (BATISTA *et al.*, 2022)

For our context, the *magnetic volatility*, vol_{mag} (Fig. 4.3), can be calculated from the standard deviations of the log magnetic return $\Delta r_{\text{mag}}(t)$ in a moving window of length ω along N sample points (TSAY, 2010).

$$\Delta r_{\text{mag}}(t) = \log \left(\frac{|\mathbf{B}(t + \tau)|}{|\mathbf{B}(t)|} \right) , \tag{4.1}$$

$$\text{vol}_{\text{mag}}(j) = \sqrt{\frac{1}{\omega - 1} \sum_{i=j}^{\omega+j-1} (\Delta r_{\text{mag}}(i) - \mu(j))^2} , \tag{4.2}$$

where τ is a time-lag, $j = 1, \ldots, N - \omega + 1$ and $\mu(j)$ is the mean Δr_{mag} inside the window (GOMES *et al.*, 2019).

The ω ant τ values are estimated from the Power Spectrum Density (PSD). Figure

4.4 shows the PSD for the March 9 time series, where the inertial range is the blue region between the dashed lines. This region was chosen as the frequency interval where the slope of the fitted line is -5/3, following Kolmogorov's K41 theory for fully developed turbulence. The frequency in the middle of the inertial range marks the scale used to define both τ and ω. In this way, we define $\tau = \omega = 50s$.
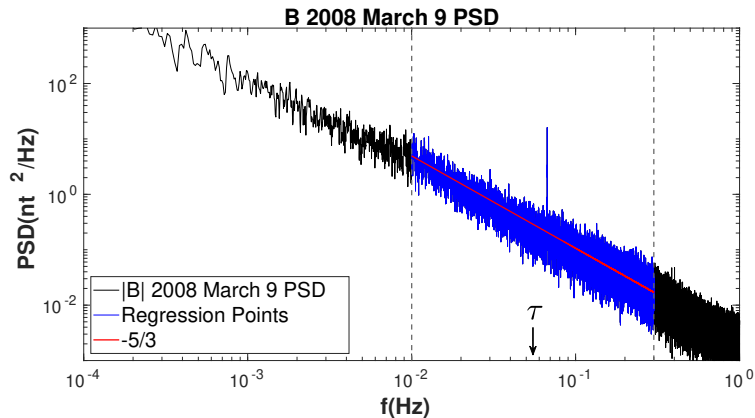
FIGURE 4.4 – Power spectral density for solar wind magnetic field of 2008 March 9. The blue region is the inertial range and the red line is the linear fit for this interval, with a slope equal to -5/3. Source: (BATISTA *et al.*, 2022)

4.2   Solar Wind Results

4.2.1   Multifractal Analysis of Solar Wind Data

4.2.1.1   MFDFA Analysis of the B Time Series

Fig. 4.5 shows different multifractal measures of the two magnetic field time series. Figure 4.5(a) shows the multifractal spectra, which reveal a left asymmetry for the March 09 time series (red) and a right asymmetry for the January 25 series (blue). The left asymmetry indicates the stronger contribution to multifractality coming from large fluctuations associated with values of $q > 0$ in the intermittent time series of the current sheet-filled times series of March 09; the right asymmetry found for the current sheet-free time series of January 25 points to the greater contribution of small fluctuations to the multifractality (IHLEN, 2012). The width of the spectrum can be used as a measure of the degree of multifractality of the series (SHIMIZU *et al.*, 2002). Comparing both spectra, it can be seen that they have almost the same width ($\Delta\alpha \approx 0.541$ for March 9 and $\Delta\alpha \approx 0.555$ for January 25), which may be surprising, since the time series of March 9 is visibly more intermittent, with strong bursts randomly interspersed in time. In this case, the difference in multifractality can be better quantified by the Renyi exponent $\tau(q)$, shown in Fig. 4.5(b). It reveals a nonlinear behavior for both series, but with $R^2 \approx 0.804$

for March 9 and $R^2 \approx 0.986$ for January 25, thus, March 9 displays higher multifractality.
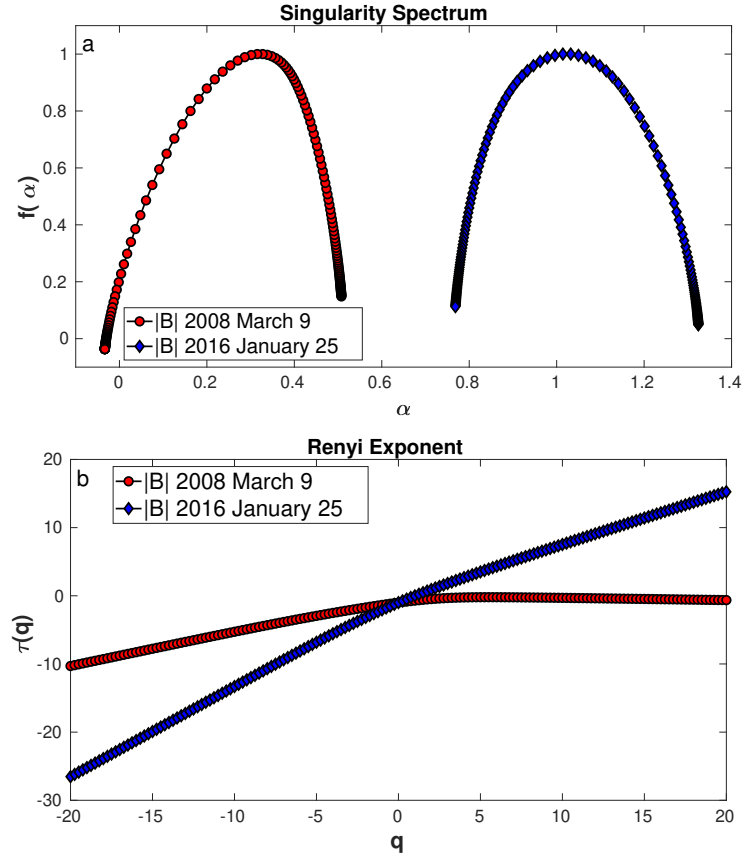
FIGURE 4.5 – (a) Multifractal spectrum for 2008 March 9 (red) and 2016 January 25 (blue). (b) Scaling exponents for 2008 March 9 (red) and 2016 January 25 (blue). Source: (BATISTA *et al.*, 2022)

4.2.1.2   MFDFA Analysis of the Volatility Time Series

Figure 4.3 exhibits the volatility time series for 2008 March 9 (upper panel, red) and for 2016 January 25 (lower panel, blue) from the decimated magnetic field data. Recall that the upper series has many current sheets while the lower one has none. Note that, unlike the January 25 series, the March 9 volatility series has several extreme events. These high peaks are due to the abrupt changes in the magnetic field that take place when the satellite crosses a current sheet in the solar wind. As a consequence, the multifractal spectra obtained from the volatility of both series are very different, as seen in Fig. 4.6. Now, the spectrum of the intermittent time series of March 9 is much broader than the one from January 25. The volatility has enhanced the contribution of the extreme events due to current sheets, thus showing the signature of coherent structures present in the solar wind that were partially hidden in the multifractal analysis of the original time series. The Renyi exponents are shown in Fig. 4.6(b); once again, the curve for March 9 is more concave than for January 25, reflecting its higher level of multifractality. It is clear that the volatility has highlighted the role of current sheets in the multifractal singularity
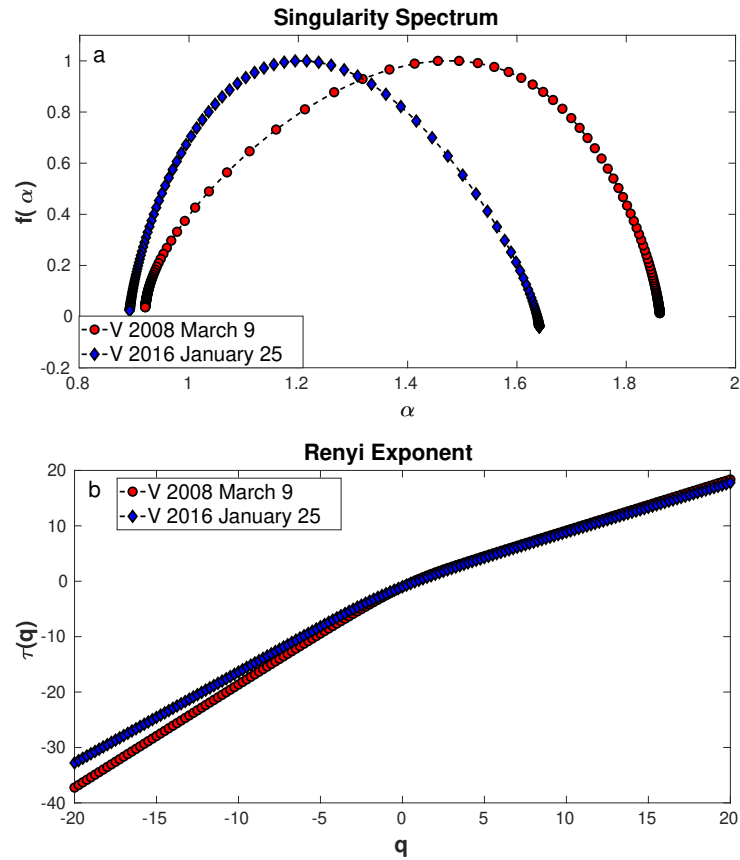
spectrum.

FIGURE 4.6 – (a) Multifractal spectra for the volatility in 2008 March 9 (red), and 2016 January 25 (blue). (b) Renyi exponents for the volatility in 2008 March 9 (red), and 2016 January 25 (blue). Source: (BATISTA *et al.*, 2022)

4.2.2   Surrogate Analysis

In the following subsections, we perform Surrogate Analysis for both the $|B|$ and volatility time series of 2008 March 9 and 2016 January 25.

4.2.2.1   Magnetic Field time series, 2008 March 9

Figure 4.7 shows the differenced time series for March 9 (red) with its shuffled (green) and random phases (magenta) surrogates. Clearly, the shuffled surrogate keeps the extreme events of the differenced $|B|$ series, but the same events are absent from the random phases surrogate.
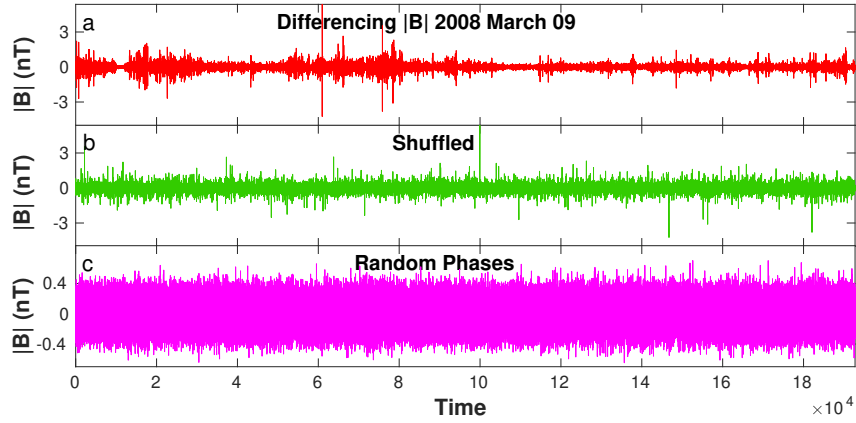
FIGURE 4.7 – Differenced time series for 2008 March 9 (red) and the respective surrogates: shuffled (green), and random phases (magenta). Source: (BATISTA *et al.*, 2022)

Figure 4.8(a) displays the multifractal spectra for the March 9 original and surrogate time series. For the shuffled spectrum (green) we see a small reduction in the width when compared with the original one (red). This means that there is a contribution from correlations to multifractality, along with the contribution of the PDF. Considering the random phases spectrum (magenta), its width reduces drastically (the $\Delta\alpha$ variation is about 0.32), which points to a significant contribution to multifractality coming from non-Gaussianity and/or nonlinear correlations. The conclusion from both spectra is that the PDF has the strongest contribution to multifractality. The contribution of the PDF is due to the presence of strong intermittent bursts (extreme events) in the March 9 time series. Since these bursts have been shown to be related to large current sheets (see (GOMES *et al.*, 2019)), the current sheets can be seen as the origin of most of the multifractality in this time series. Fig. 4.8(b) confirms this conclusion by showing the Renyi exponent as a function of q, where the random phases surrogate has a smaller concavity than the shuffled surrogate.
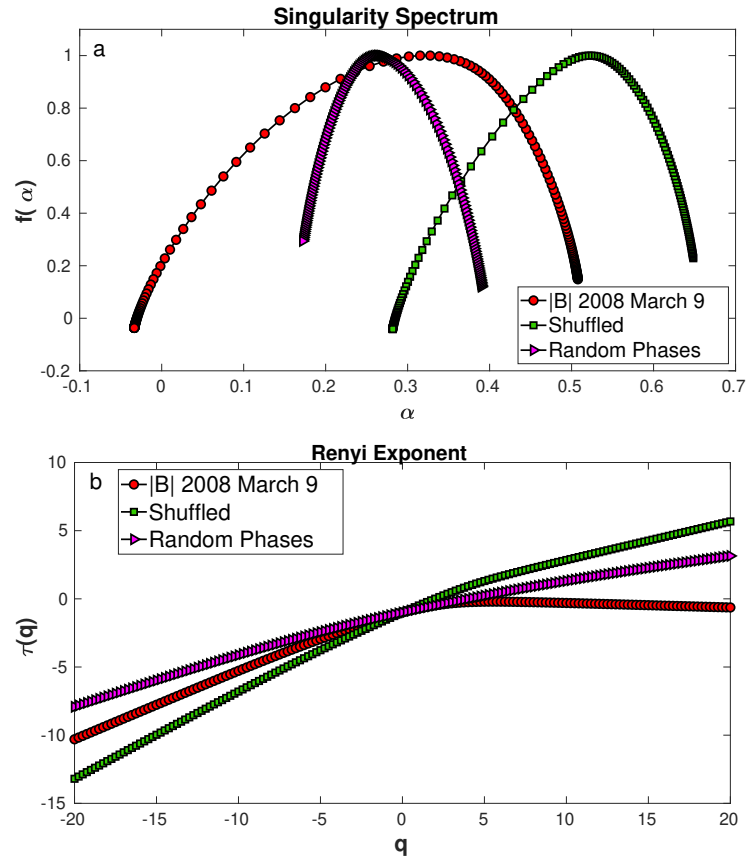
FIGURE 4.8 – (a) Multifractal spectrum of $|B|$ for 2008 March 9 (red) and the respective surrogates: shuffled (green), and random phases (magenta). (b) Renyi exponents for 2008 March 9 (red) and the respective surrogates: shuffled (green), and random phases (magenta). Source: (BATISTA *et al.*, 2022)

4.2.2.2 Magnetic Field time series, 2016 January 25

Figure 4.9 shows the time series for January 25 (black) with its shuffled (green) and random phases (blue) surrogates. Figure 4.10 shows a significant width reduction in both surrogate spectra in comparison with the original spectrum (blue). The spectrum of the shuffled series (green) has a width $\Delta\alpha = 0.194$, indicating a difference of 0.36 with the spectrum of $|B|$. Similarly, the spectrum for the random phases series has a small width, about $\Delta\alpha = 0.32$, a difference of 0.23 with the spectrum of $|B|$. So, there is strong influence from long-range correlations as well as non-gaussianity on the January 25 magnetic field multifractality, but the contribution of the correlations is preponderant, since the shuffled spectrum is considerably narrower than the random phases spectrum.
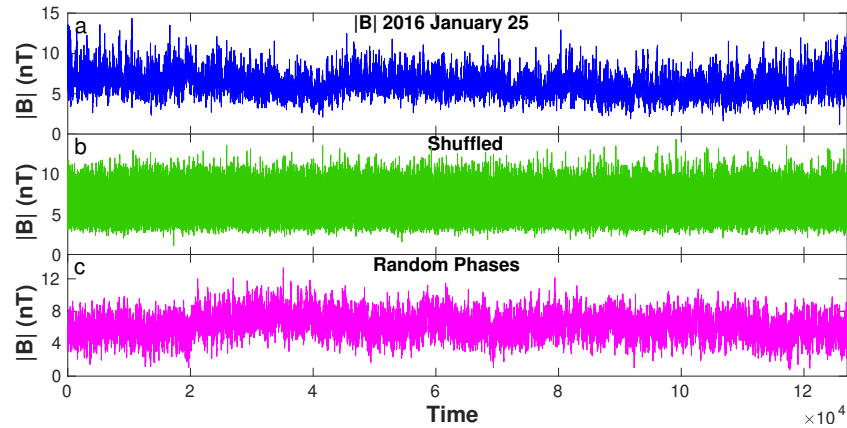
FIGURE 4.9 – Time series for 2016 January 25 (blue) and the respective surrogates: shuffled (green), and random phases (magenta).
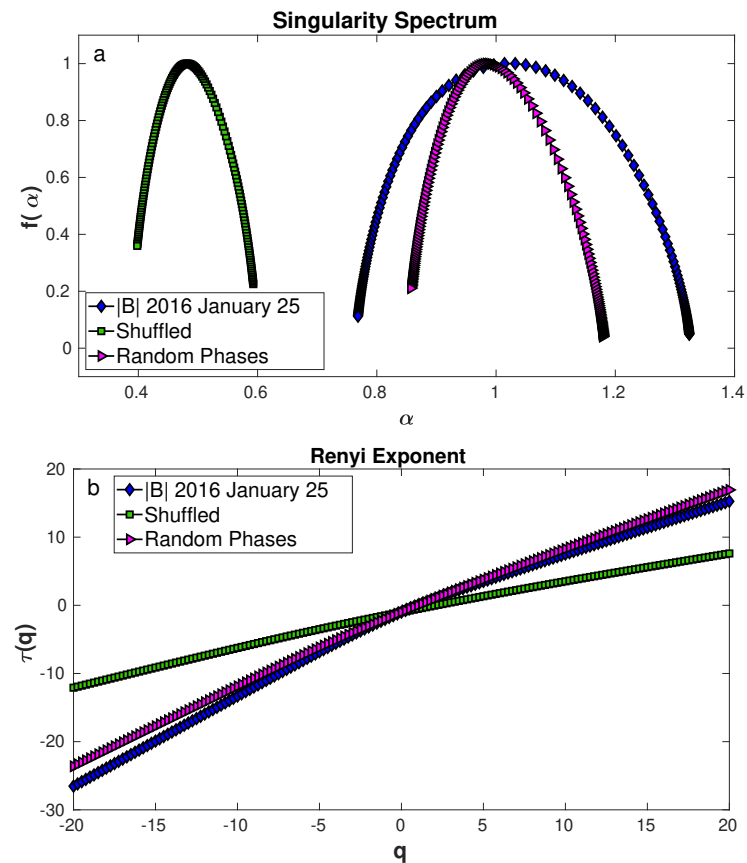
FIGURE 4.10 – (a) Multifractal spectrum for 2016 January 25 (blue) and the respective surrogates: shuffled (green), and random phases (blue). (b) Renyi exponents for 2016 January 25 (blue) and the respective surrogates: shuffled (green), and random phases (magenta). Source: (BATISTA *et al.*, 2022)

4.2.2.3   Volatility time series, 2008 March 9

We proceed with the analysis of the origin of the multifractality for March 9 using the volatility, as shown in Fig. 4.11 for the original (red), shuffled[4] (green) and random phases (magenta) time series. The corresponding multifractal spectra in Fig. 4.12 show a wide parabola for the original volatility series (red) and two narrower parabolas related to its shuffled (green) and random phases (magenta) series. The random phases spectrum has a width of about $\Delta\alpha = 0.39$ and the shuffled spectrum has a width of $\Delta\alpha = 0.35$. Since both spectra have approximately the same width, it shows an important feature that was not so clear from the multifractal spectra of the $|B|$ surrogate series (Fig. 4.11), that is, the importance of the nonlinear correlations, which play a key role, together with the non-gaussianity, in the origin of the multifractality for the March 9 series. Since the volatility is computed with a lag-time of $\tau = 50s$, it is better suited for measuring the relevance of long-range nonlinear correlations than the time-differenced $|B|$ series. Fig. 4.12 confirms that the shuffled and random phases series have almost linear Renyi exponents, thus, the series are closer to monofractal.
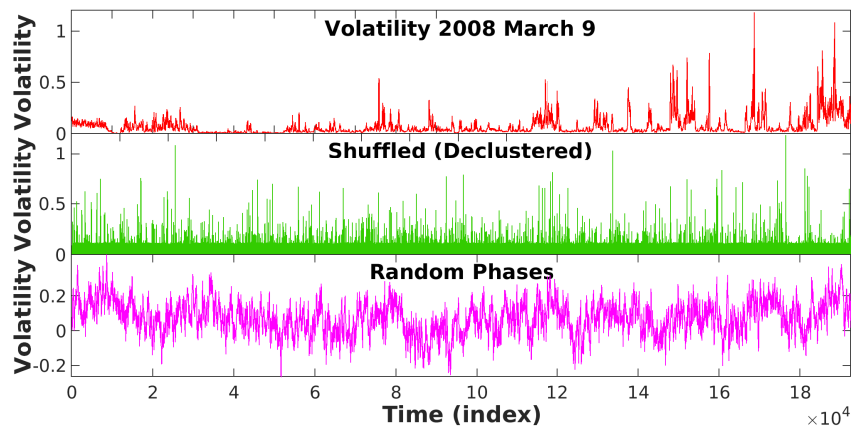
FIGURE 4.11 – Time series Volatility for 2008 March 9 (red) and the respective surrogates: shuffled (green), and random phases (blue). Source: (BATISTA et al., 2022)

---

[4]Due to the formation of *clusters* in this time series, it was necessary to use the *runs declustering* method (LEADBETTER, 1983). This declustering process is described in (GOMES, 2018; GOMES et al., 2019)
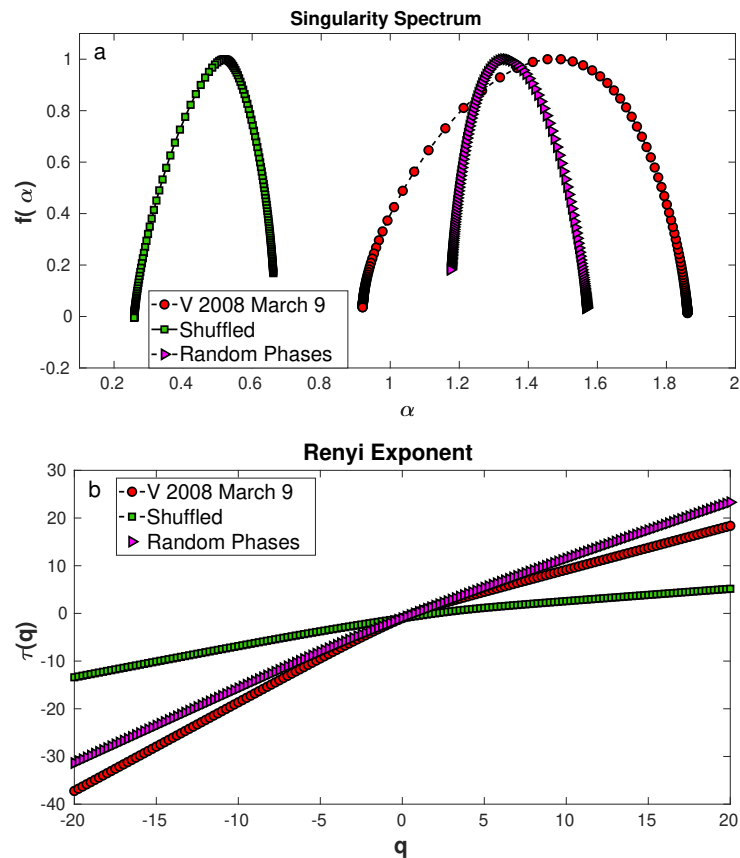
FIGURE 4.12 – (a) Multifractal spectrum for the volatility of 2008 March 9 (red) and the respective surrogates: shuffled (green), and random phases (magenta). (b) Renyi exponents for the volatility of 2008 March 9 (red) and the respective surrogates: shuffled (green), and random phases (magenta). Source: (BATISTA *et al.*, 2022)

4.2.2.4   Volatility time series, 2016 January 25

Figure 4.13 shows the volatility time series of the January 25 time series (blue) and its shuffled (green) and random phases (magenta) surrogates. Figure 4.14 shows the corresponding multifractal spectra. Once again, the reduction in the width for both surrogate spectra means that a mutual contribution to multifractality coming from long-range correlations and non-Gaussianity is present, with a clear predominance of the long-range correlations effects, since the shuffled spectrum is much narrower than the random phases spectrum.
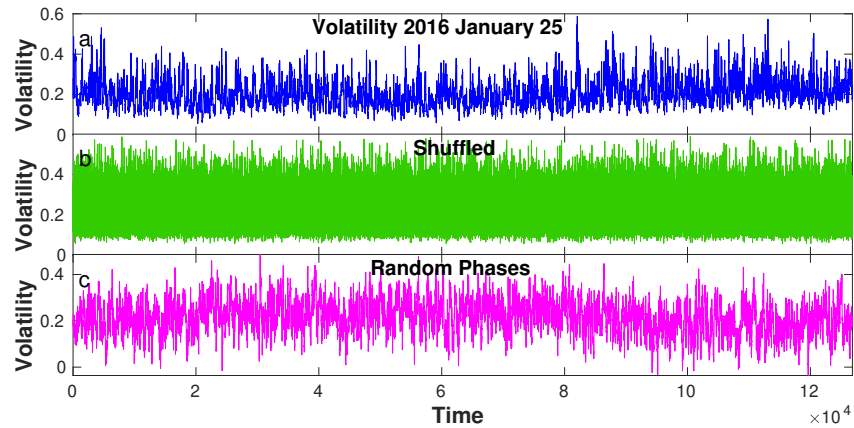
FIGURE 4.13 – Time series of the volatility for 2016 January 25 (blue) and the respective surrogates: shuffled (green), and random phases (magenta). Source: (BATISTA *et al.*, 2022)
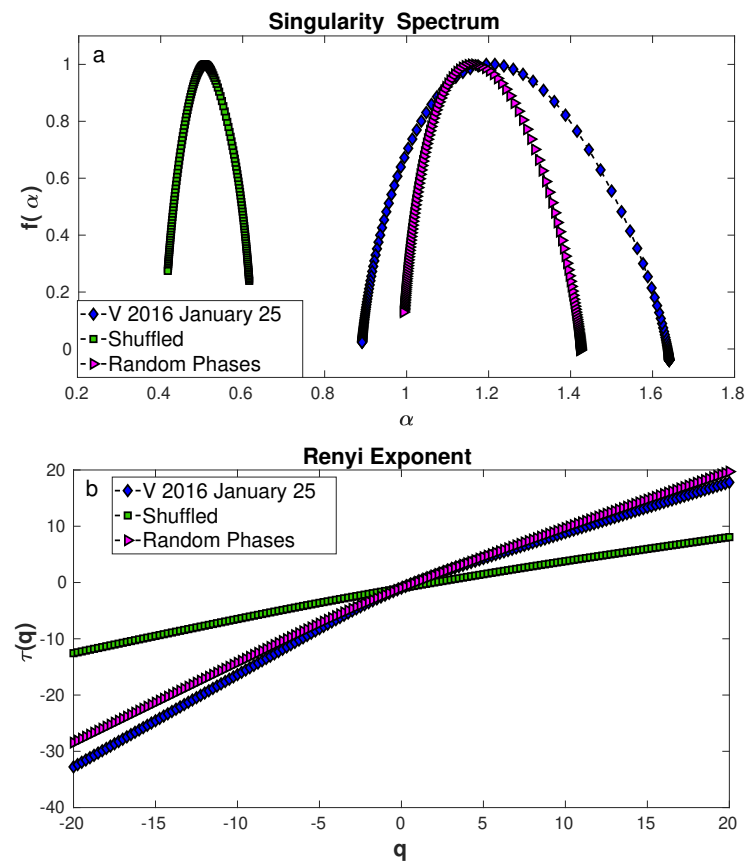
FIGURE 4.14 – (a) Multifractal spectrum for the volatility of 2016 January 25 (blue) and the respective surrogates: shuffled (green), and random phases (magenta). (b) Renyi exponents for the volatility of 2016 January 25 (blue) and the respective surrogates: shuffled (green), and random phases (magenta). Source: (BATISTA *et al.*, 2022)

4.2.2.5 Tables

A quantitative comparison of all the results for the $|B|$ time series and volatility time series of March 9 and January 25 is provided by Tables 4.1 and Fig. 4.15 to 4.3 and

Fig. 4.17. Table 4.1 and Figure 4.15 show R^2 for the Renyi exponent of $|B|$ and its volatility for March 9 and January 25; Table 4.2 and Figure 4.16 show the width of the multifractal spectra, $\Delta\alpha$; Table 4.3 and Figure 4.17 show the asymmetry of the spectra, A. In general, all spectra for January 25 are right-asymmetric due to the importance of small scale fluctuations; for March 9, some spectra are left-asymmetric due to the importance of large-scale fluctuations, but the random phases show right asymmetry, since in the random phases surrogate the effects of non-Gaussianity are destroyed.

TABLE 4.1 – R^2 of the Renyi exponent for magnetic field and volatilities of 2008 March 9 and 2016 January 25. Source: (BATISTA *et al.*, 2022)

| | March 9 (**CS**) | | January 25 | |
	$|B|$	Volatility	$|B|$	Volatility
Original	0.80413	0.97464	0.98597	0.98125
Shuffle	0.97505	0.96748	0.99537	0.99573
Random Phases	0.98185	0.99637	0.99601	0.99424
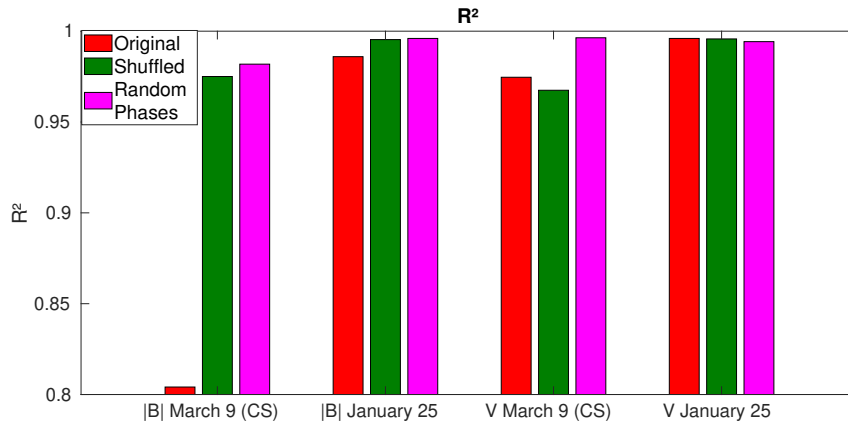
FIGURE 4.15 – Coefficient of Determination, R^2, of the Renyi exponent for magnetic field and volatilities from 9th March, 2008, 25th January, 2016, and its surrogates.

TABLE 4.2 – Width of α, $\Delta\alpha$, for magnetic field and volatilities of 2008 March 9 and 2016 January 25. Source: (BATISTA *et al.*, 2022)

| | March 9 (**CS**) | | January 25 | |
	$|B|$	Volatility	$|B|$	Volatility
Original	0.54112	0.94134	0.55568	0.74921
Shuffle	0.36663	0.40332	0.19468	0.19873
Random Phases	0.21802	0.39299	0.32181	0.43088
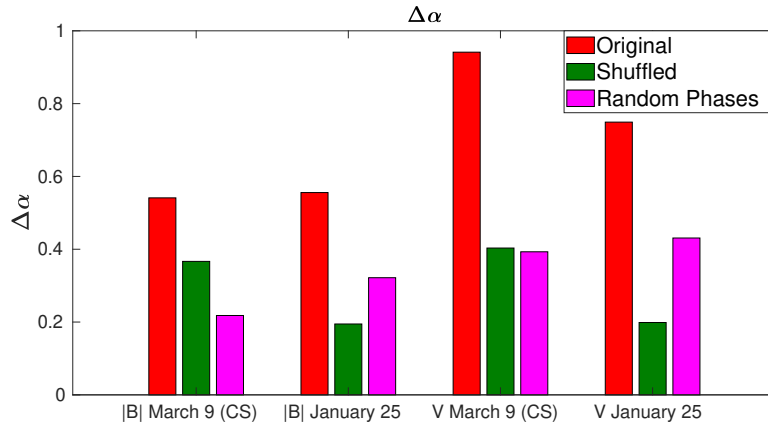
FIGURE 4.16 – Width of α, $\Delta\alpha$, for magnetic field and volatilities from 9th March, 2008, 25th January, 2016, and its surrogates.

TABLE 4.3 – Spectrum Asymmetry, A, for magnetic field and volatilities of 2008 March 9 and 2016 January 25. Source: (BATISTA $et~al.$, 2022)

	March 9 (**CS**)		January 25	
	$|B|$	Volatility	$|B|$	Volatility
Original	0.49873	0.63885	1.10709	1.31215
Shuffle	0.51279	0.53342	1.30854	1.18283
Random Phases	1.33583	1.41817	1.45999	1.47002
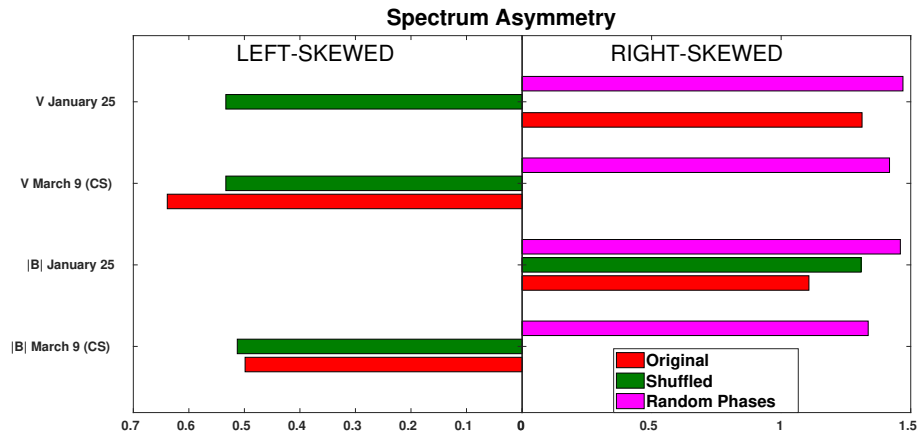
FIGURE 4.17 – Spectrum Asymmetry, A, for magnetic field and volatilities from 9th March, 2008, 25th January, 2016, and its surrogates.

4.2.3   Zeta Function

In Fig. 4.18, the linear K41 theoretical zeta scaling exponent function is shown by the black dashed line while the IK scaling exponent is denoted by a dotted line. The top

panel (a) also shows the zeta scaling exponent computed from the time series of $|B|$ for the intermittent series of March 09 (red line with circles) and for the current sheet-free series of January 25 (blue line with diamonds). The zeta function for the March 09 series clearly departs from the linear behavior, as expected for multifractal intermittent series, but, surprisingly, the zeta function exhibits an almost linear relation with p in the case of January 25, despite the fact that both series have multifractal spectra with similar widths (see Fig. 4.5). Thus, one should be cautious before using the behavior of the scaling exponent as a definite measure of multifractality, although it is a good measure of intermittency. To confirm this result, Fig. 4.18 (left panel) compares the zeta scaling exponents of the March 09 $|B|$ series (red line with circles) with the zeta scaling exponents of its random phases series (magenta line with triangles). Since the random phases series has a Gaussian PDF, it removes from the original series the intermittent extreme events responsible for the fat-tailed PDF and the zeta scaling exponent becomes linear, following the K41 line.
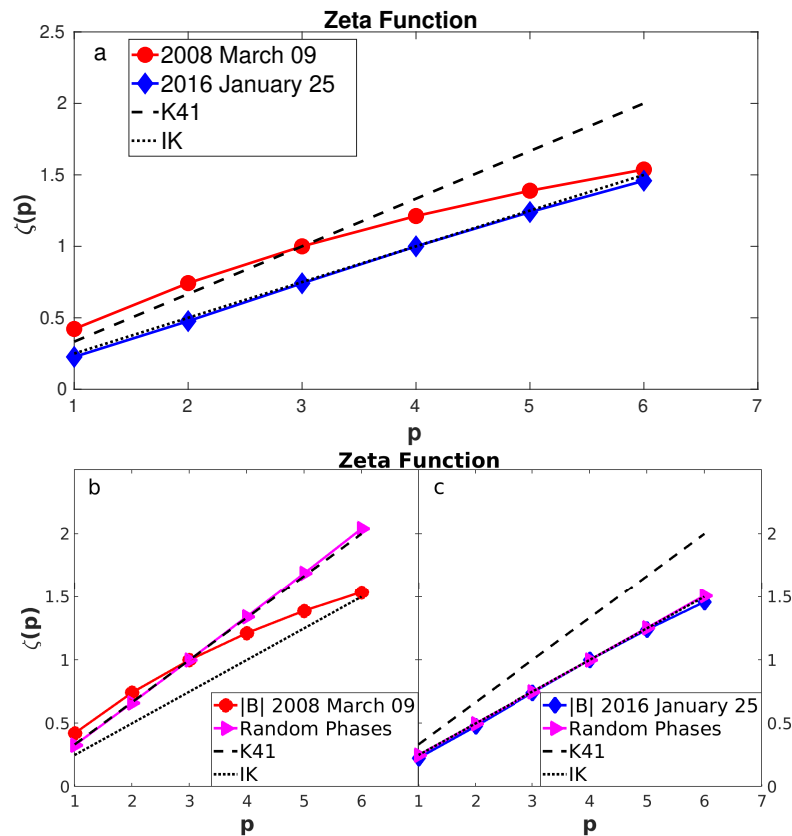
FIGURE 4.18 – (a) Zeta functions for the magnetic field time series for 2008 March 9 (red circles) and 2016 January 25 (blue diamonds). (b) Left: Zeta functions $|B|$ 2008 March 9 and its Random Phases (magenta triangles). (c) Right: Zeta functions for $|B|$ 2016 January 25 and its Random Phases (magenta triangles). The dashed lines represent the Kolmogorov K41 scaling and the dotted line, IK. Source: (BATISTA *et al.*, 2022)

This result confirms the importance of the contribution from a fat-tailed PDF to the multifractality of the March 09 series. In Fig. 4.18 (right panel), the same analysis is

done for the January 25 series, where both the original series and its random phases show an IK linear behavior, since none of the series has fat-tailed PDF, although they have multifractal spectra (see the blue and magenta spectra in Fig. 4.9). We conclude from this that the ζ-function is a good measure of multifractality due to PDF, but misses the contribution of long-range correlations to the multifractality.

4.2.4 p-model

Figure 4.19 shows the MF-DFA multifractal spectra for the volatility series of March 9th (red circle) and January 25th (blue diamond). The $p-$model fits obtained from Eqs. (3.36) and (3.37) in Section 3.7 are also shown (black line with dots). The values of p_1, dp and l_1 were obtained with a Monte Carlo method that minimized the mean squared error between the original and fitted spectra. For March 9th, we obtained $p_1 = 0.71$, $dp = 0.17$ and $l_1 = 0.68$. For January 25th, we obtained $p_1 = 0.51$, $dp = 0.11$ and $l_1 = 0.66$. The agreement between the observational and theoretical curves confirms that the solar wind multifractal spectra can be obtained from a turbulence cascade process.
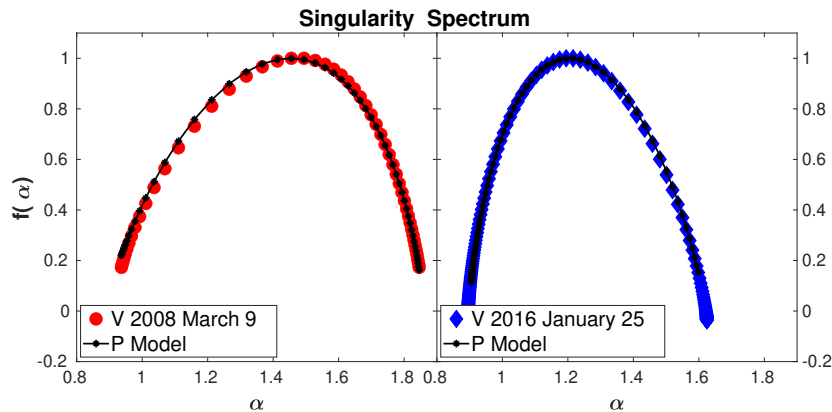
FIGURE 4.19 – Left: Multifractal spectrum for the volatility of 2008 March 9 (red circle) and its $p-$model fit (black line with dots). Right: Multifractal spectrum for the volatility of 2016 January 25 (blue diamond) and its $p-$model fit (black line with dots). Source: (BATISTA *et al.*, 2022)

This is a remarkable result, since the $p-$model was specifically elaborated to represent turbulent cascade processes, and will usually not be able to approximate the multifractal spectra of purely stochastic processes in general.

TABLE 4.4 – p-model fit values (p_1, l_1 and dp) for volatilities from 9th March, 2008 and 25th January, 2016

Volatility	March 9 (**CS**)	January 25
p_1	0.71	0.51
l_1	0.68	0.66
dp	0.17	0.11
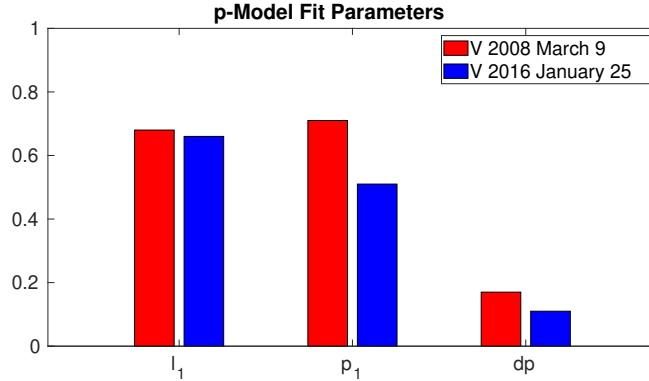
FIGURE 4.20 – p-model fit values (p_1, l_1 and dp) for volatilities from 9th March, 2008 and 25th January, 2016

Figure 4.21 presents a comparative analysis between the solar wind volatility time series and the $p-$model time series. The upper panels display the solar wind series for March 9 (a) along with its corresponding $p-$model representation (b), while the lower panels showcase the solar wind series for January 25 (c) and its corresponding $p-$model depiction (d). In both instances, a noticeable qualitative resemblance is observed between the observational and $p-$model time series.
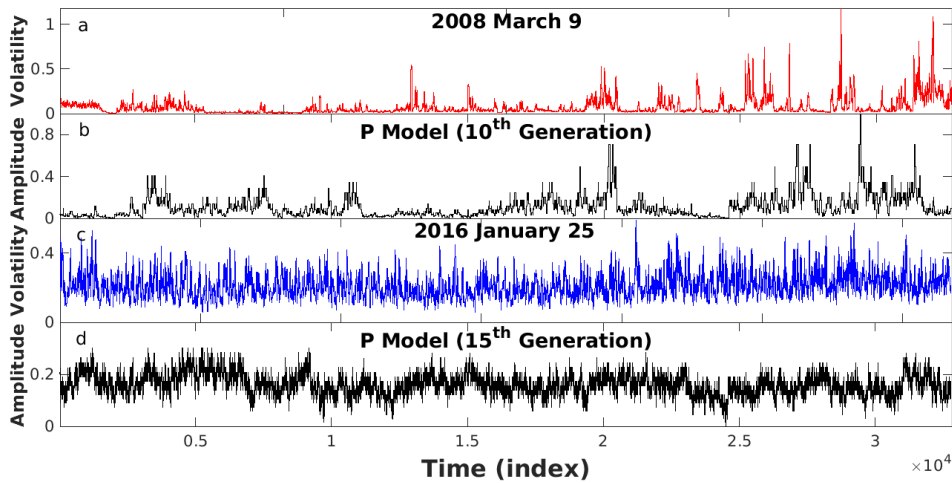
FIGURE 4.21 – (a) Volatility time series for 2008 March 9 (red) and (b) generated $p-$model time series (black) by 10th iteration. (c) Volatility time series for 2016 January 25 (blue) and (d) generated $p-$model time series (black) by 15th iteration. Source: (BATISTA *et al.*, 2022)

Afterward, we proceed to compare the Power Spectral Densities (PSDs) obtained from $p-$model turbulent time series and the observational solar wind volatility time. Fig. 4.22 displays a comparative analysis between observed and simulated Power Spectral Densities (PSDs). The upper panels of Fig. 4.22 exhibit the PSDs for the volatility time series of March 9, 2008 (left) and January 25, 2016 (right). The blue region delimited by vertical dashed lines corresponds to the inertial range, while the red line represents the linear regression with slope $-5/3$ for the March 9 series and $-3/2$ for the January 25 series. Consequently, the March 9 series, characterized by its high intermittency and presence of current sheets, exhibits a K41 scaling. In contrast, the January 25 series, which lacks current sheets, displays an IK scaling. These findings were previously established by LI *et al.* (2011) and confirmed by GOMES *et al.* (2019) through PSDs computed from the time series of $|B|$.
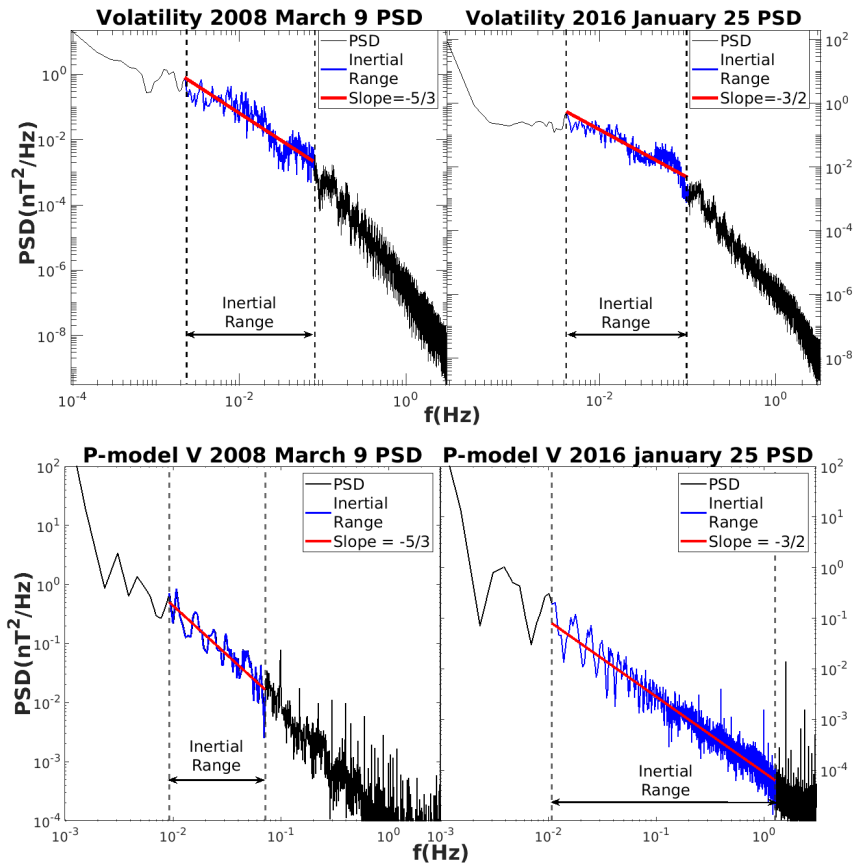
FIGURE 4.22 – (a) Left: Power spectral density for 2008 March 9 volatility. (a) Right: Power spectral density for 2016 January 25 volatility. (b) Left: Power spectral density for generated $p-$model time series from 2008 March 9 volatility. (b) Right: Power spectral density for generated $p-$model time series from 2016 January 25 volatility. The blue regions mark the inertial range and the red lines are the linear fits for those intervals. Source: (BATISTA *et al.*, 2022)

It is important to note that in both cases, the inertial range extends almost throughout the entire PSDs, primarily due to the small dissipation term of $p-$model. From our analysis, we can confidently conclude that a K41 intermittent turbulence cascade is the

driving mechanism behind the multifractality observed in the current sheet-filled time series on March 9, while an IK turbulence cascade is responsible for the multifractality observed in the January 25 series. This finding aligns with our previous investigations of other time series, demonstrating that current sheets are responsible for K41 turbulence multifractality, whereas the absence of current sheets leads to IK turbulence multifractality in the solar wind (refer to Table 4 in (GOMES *et al.*, 2019)).

4.3 Active Region Data

4.3.1 AR 11158

In this second problem, we focus on observation of a specific active region. The AR 11158, observed by the *Solar Dynamics Observatory* (SDO) spacecraft, presents a substantial flare activity, with emphasis on the presence of a X-class flare. The vector magnetograms have been obtained by *Space-Weather Helioseismic* and *Magnetic Imager* (HMI) *Active Region Patches* (SHARP) (SCHERRER *et al.*, 2012), with a pixel resolution of 0.5″ ($\approx$ 360 km) and a time resolution of 12 minutes (Figure 4.23(a,b,c)). As cited before, the AR 11158 is know by its intense flare activity and because of this, has been continuously studied through the years (TORIUMI *et al.*, 2014; GEORGOULIS, 2013; LI; LIU, 2015; SORRISO-VALVO *et al.*, 2015). This active region started its development on February 9th 2011 with a lifetime about 11 days in the solar southern hemisphere. During this period, it was possible to detect about ten C-class, five M-class, and one X-class flare, which is the first one of Solar Cycle 24 (SCHRIJVER *et al.*, 2011). All these events are directly related to the quadrupole (N1-P1 and N2-P2, Fig.4.23) system which evolves thought the days generating a large number of *Emerging Flux Regions* (EFR). Based on these informations, we defined a 150 hours interval of observation time for this region, representing about 750 SHARP magnetogram data frames (Figure 4.23). By setting the initial measurement time at February 9th at 22:00:00 UT, we can follow the most important flare events, in particular for this work, two M-class flares (first at February 13th 17:28:00 UT and the second one at February 16th at 7:35:00 UT) and in the X-class flare (February 15th at 1:44:00 UT).

For these two-dimensional structures we have applied the 2-D MFDMA method (section 3.4.1) with the following parameters: $n_i = 10$ and $n_f = N/2$, where N is the length of the smallest size axis; q varies between -5 and 5 with an increment of $\Delta q = 0.25$, and $\theta = 0$ (BMA) (Figure 4.23(d)). From this point, it was possible to obtain the Renyi exponent and the singularity spectrum from each magnetogram and at last generate different time series of multifractal parameters as A, $\Delta \alpha$ and R^2 with respect the the active region's progress (BATISTA *et al.*, 2022).

4.4   Active Region Results

4.4.1   Multifractal Analysis of AR 11158

Figure 4.24 shows the time evolution of the multifractal parameters of AR 11158 magnetograms. As we can see in Figure 4.24(a), the multifractal strength parameter $\Delta\alpha$ grows, especially in the first 38 hours, following the appearance and growth of the active region. After this first continuous increase, it is possible to see a slight decay until $\approx$ 58 hours (just 5 hours before the flaring activity begins). Subsequently, we see a growth recovery that goes through the first M-class flare (M6.6) and it has a new decay between the second M-class (M2.2) flare and the X-flare (X2.2) in February 15 (100 hours later). Afterwards, we detect a small decline in the $\Delta\alpha$ value, but remaining in a plateau interval varying from $\approx 1.7 - 2.1$. Now, for the R^2 parameter, we known from Eq. (3.12) that when the values are moving away from 1 the structure is more multifractal. In Figure 4.24(c) it is observed a significant reduction of R^2 parameter until 38 hours of active region evolution. In general, the R^2 parameter behavior follows the same mode pattern noted for $\Delta\alpha$ data, but due to its smoother behavior, it is possible to see a slight multifractal decrease in relation with time.
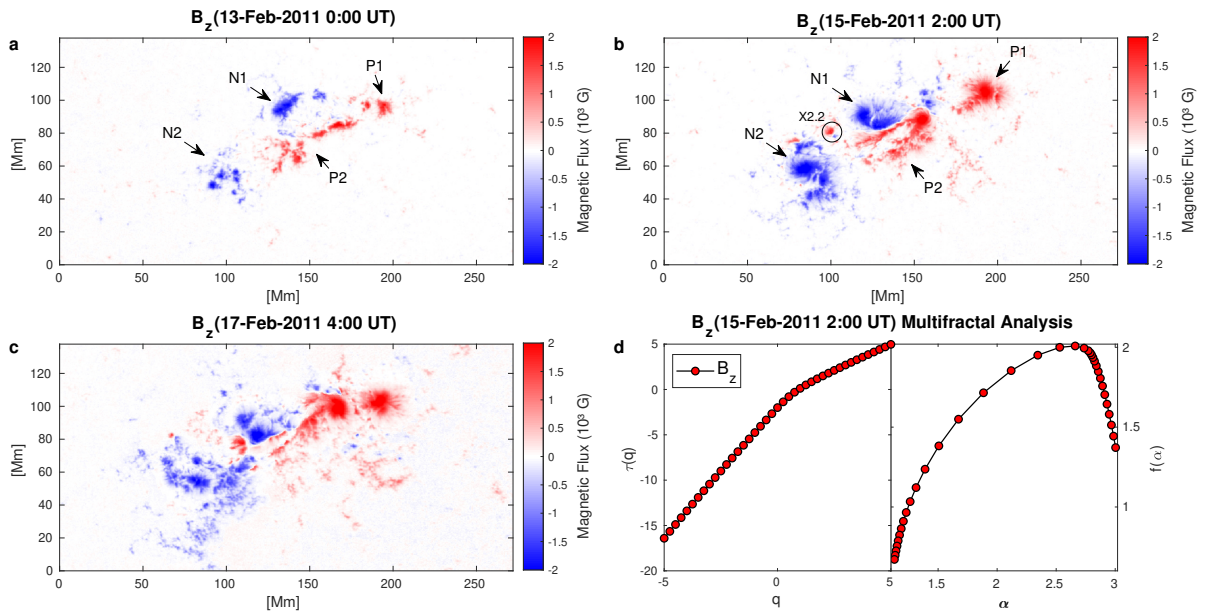
FIGURE 4.23 – (a, b, c) Spatial distribution of the vertical component of the magnetic field (B_z) for AR 11158 at three different times and (d) the multifractal parameters (Renyi Exponent and Singularity Spectrum) for the X-class flare instant (15-Feb-2011 2:00 UT). N1, N2, P1, P2 are the negative and positive polarities respectively of AR and the black contour points the region of the X2.2 flare event.

Another important parameter obtained from the multifractal spectrum is the asymmetry A (Eq. (3.11)). In this case, the first point observed in Figure 4.24(b) that needs to be emphasized is the range where the parameter is kept. All values are lower than 1,

i.e., all singularity spectra are left-skewed asymmetric. This left asymmetry points to a larger contribution of large fluctuations to multifractality of all B_z frames. Low A values denote a high left asymmetry. In the first 20 hours ($\approx$ 11-Feb-2011 18:00 UT) we see a maximum asymmetry and after that, the spectra continuously become less asymmetric if compared with the initial activity. Skipping the first M-class flare, we also see minor variations nearby the flares, e.g. M2.2 and X2.2-class flares.
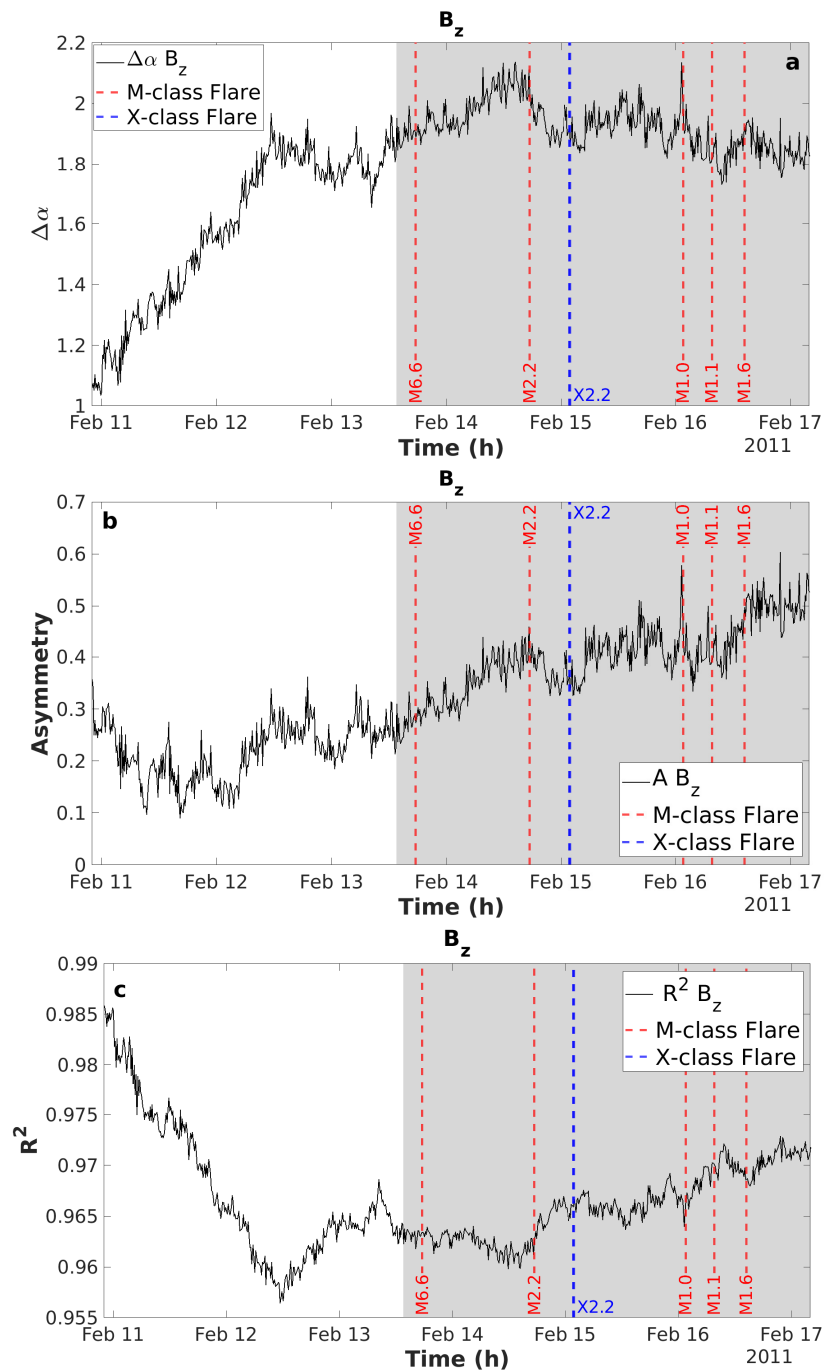
FIGURE 4.24 – Multifractal parameters (Renyi Exponent and Multifractal Spectrum) evolution for Magnetic field (B_z) of AR 11158. (a) and (b) represent the $\Delta\alpha$ variation and the $alpha$ asymmetry respectively (both obtained from singularity spectrum); (c) is the R^2 variation from Renyi exponent. The gray area refers to flare activity interval, the red (M-class) and blue (X-class) dashed lines show the flare moments.

4.4.2 Vortex Detection in AR 11158

The detection of photospheric Lagrangian coherent structures is primary to understand the evolution of its magnetic field. In 2018, SILVA *et al.* proposed the use of the *lagrangian averaged vorticity deviation* (LAVD) method to detect persistent objective velocity field vortices on the quiet Sun photosphere. Later, CHIAN *et al.* (2019) kept the study by linking with attracting/repelling LCS. So, CHIAN *et al.* (2023), also detected objective magnetic vortices on the quiet Sun region, but through the z component of the current. This work presents the first objective magnetic vortex detection by applying the IACD method in the AR photosphere. We compute the *Integrated Averaged Current Deviation* (IACD) to AR 11158 interval SHARP data using the horizontal components of the magnetic fields (Figure 4.25).
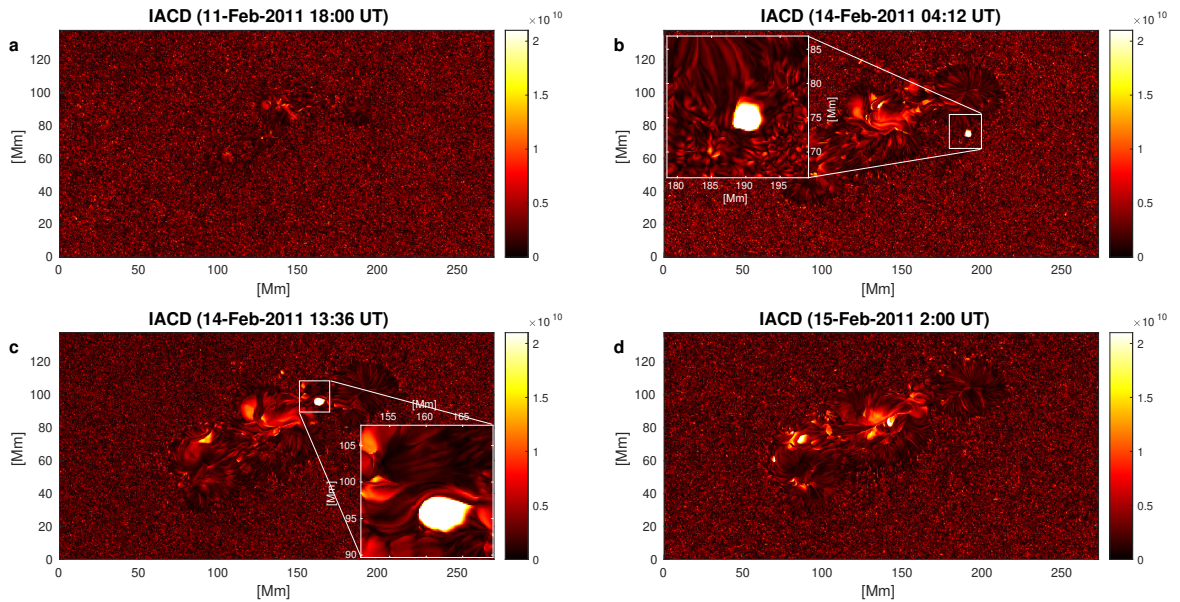
FIGURE 4.25 – Spatial distribution of IACD for AR 11158 in different times. (b) Presents the first magnetic vortex V_M in a 22×22 Mm window and (c) shows a second active vortex V_X in a 18×18 Mm window.

In addition to the primary goal of vorticiy detection, our intent, after obtaining the IACD fields from the AR 11148, was also analyzing the multifractality of theses fields in the same way as previously done for the B_z frames. We detected persistent objective vortices in particular regions and time intervals of the data, as shown in the Figure 4.25. So, from now on, the analysis of these vortical patterns becomes our main focus.

A first objective magnetic vortex V_M was detected at about 2011 February 13 22:48 UT in the region shown in Fig. 4.25(b), nearby a region formed by two merging magnetic structures. Figure 4.26 shows the time evolution of this 4 Mm vortex during its almost 18 hours lifetime through a 179-200 Mm (x axis) $\times$ 66-87 Mm (2 axis) zoom region. This persistent objective vortex oscillates across the AR 11158 for 12 hours and then

lowers the intensity for about 3 hours, until it regains the strength for a few hours before completely disappearing at 2011 February 14 17:24 UT. In addition to the evidence of vortex detection, another intriguing observation can be pointed out. The instant at which the vortex disappears matches with the M2.2-class flare beginning (2011 February 14 17:20 UT). This observation suggests that these phenomena are inextricably linked, and that the processes which generated the appearance of the M-class flare effectively caused the destruction of the vortex, i.e., the disappearance of a persistent objective vortex can be an indication of the formation of a flare of a higher intensity.
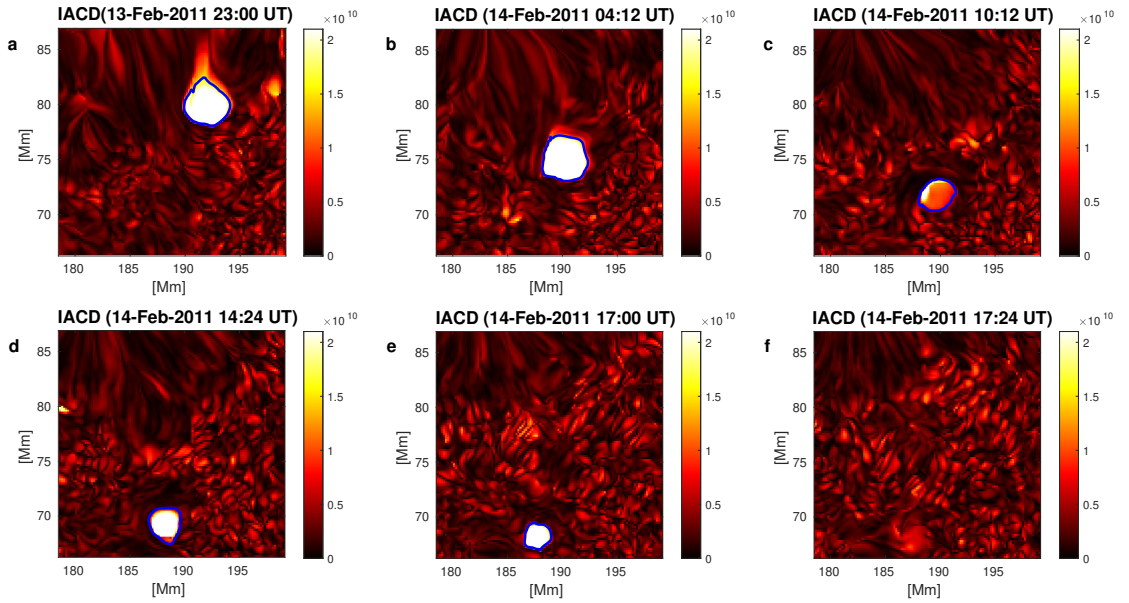
FIGURE 4.26 – Spatial distribution of the IACD around the vortex V_M region (179-200 Mm $\times$ 66-87 Mm) for different times. The first frame (a) marks the beginning of the vortex formation and the last one (f) its end. The blue contours denote the objective vortex boundary.

We also found a second objective vortex V_X formed at $\approx$ 2011 February 14 10:00 UT in the region shown in Fig. 4.25(c). Figure 4.27 shows the 16 hours lifetime of this second magnetic vortex with $\approx$ 6 Mm of diameter observed in a (151-169 (x axis) $\times$ 90-108 Mm (y axis)) window. Unlike the first one, the IACD intensity of this vortex doesn't vary as much over time, at least for the first 14 hours. Then, for the next 2 hours, this coherent structure significantly reduces its intensity reaching a total vanishing at 2011 February 15 2:00 UT. Following the same pattern as V_M, the point of extinction of this vortex coincides with the moment of an X-class flare emergence (2011 February 15 1:44 UT).
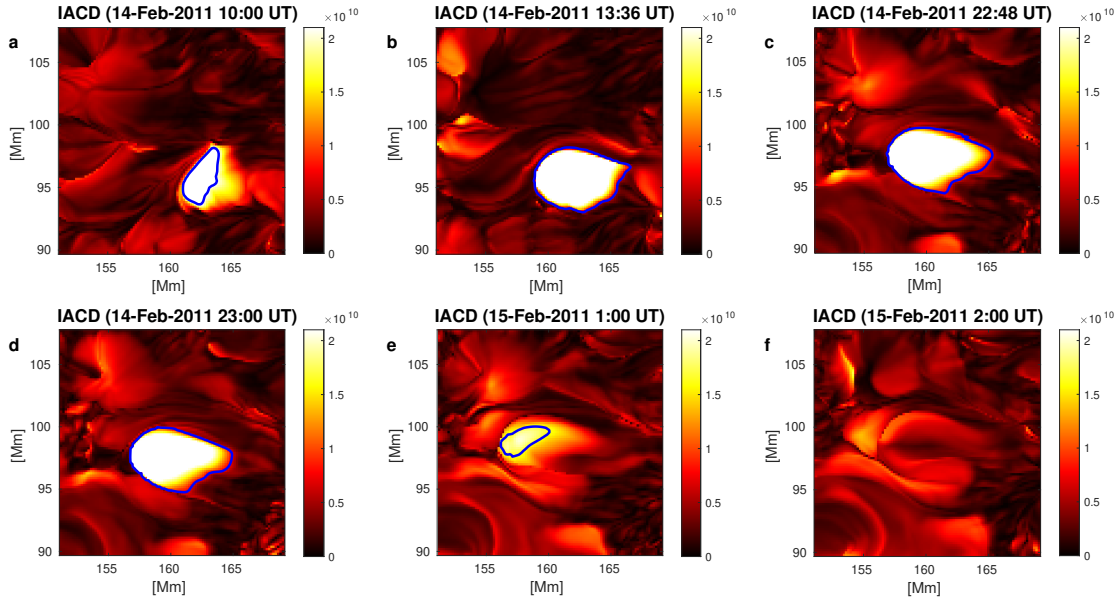
FIGURE 4.27 – Spatial distribution of IACD for the magnetic vortex V_X region (151-169 × 90-108 Mm) at different times. The first frame (a) marks the beginning of the vortex formation and the last one (f) its end. The blue contours denote the objective vortex boundary.

When we analyze the region of Lagrangian vortex formation V_X under the magnetic field perspective, it is possible to see the evolution of the fast rotating sunspot related to it. As already observed in JIANG *et al.*; SONG *et al.* (2011,2013), this negative polarity structure evolves in the P2 region direction until it hits it at the exact moment of the X2.2 flare event, Figure 4.28. The SONG *et al.* (2013) study also related the acceleration of a southwest rotating sunspot and reaching positive polarities near the N2 region (Figure 1.2). However, our results lead to the objective vortex V_M, which is placed in a different region of the AR, just above the region P1. The observation of magnetic field evolution in the vortical zoom region also suggests an interaction of the related fast rotating sunspot and the P2 region, as we can see in Figure 4.29.
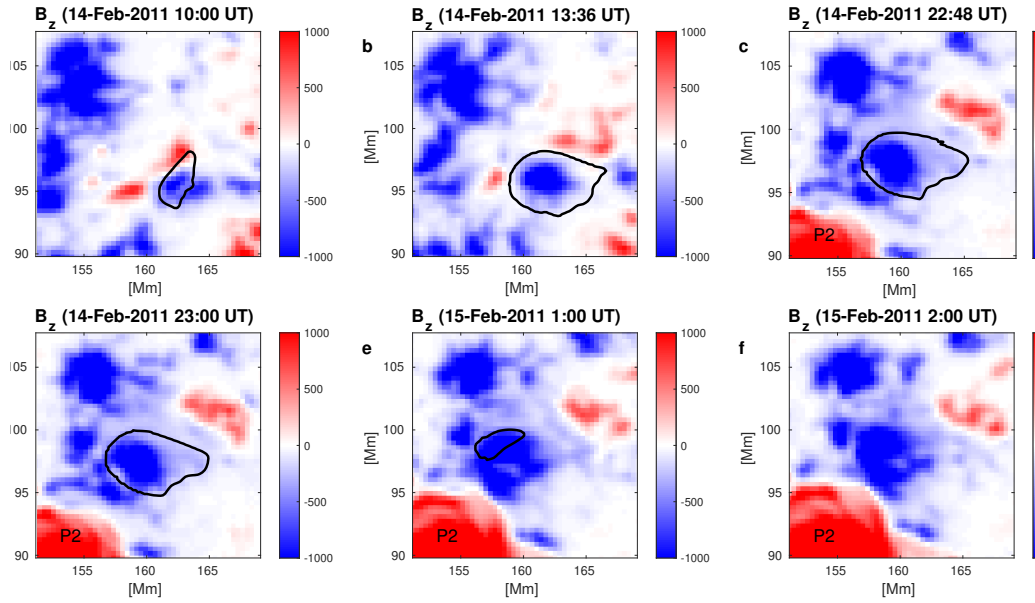
FIGURE 4.28 – B_z component of the magnetic field for the region of active vortex V_X (151-169 × 90-108 Mm) at different times. The black contours denote the objective vortex.

These observations confirm the results from SONG *et al.* (2013) which tracked the evolution of all polar structures of AR 11158. That work proposed a relation between a negative polarity region (clockwise rotating sunspot) and P2 at the moment they are getting near the X2.2 flare (Figure 1.2). Our detection of the objective vortex confirms the idea proposed by JIANG *et al.* (2011) that suggests that the cancellation and the collision of these opposite polarity structures are the trigger for an energy releasing of major flare.
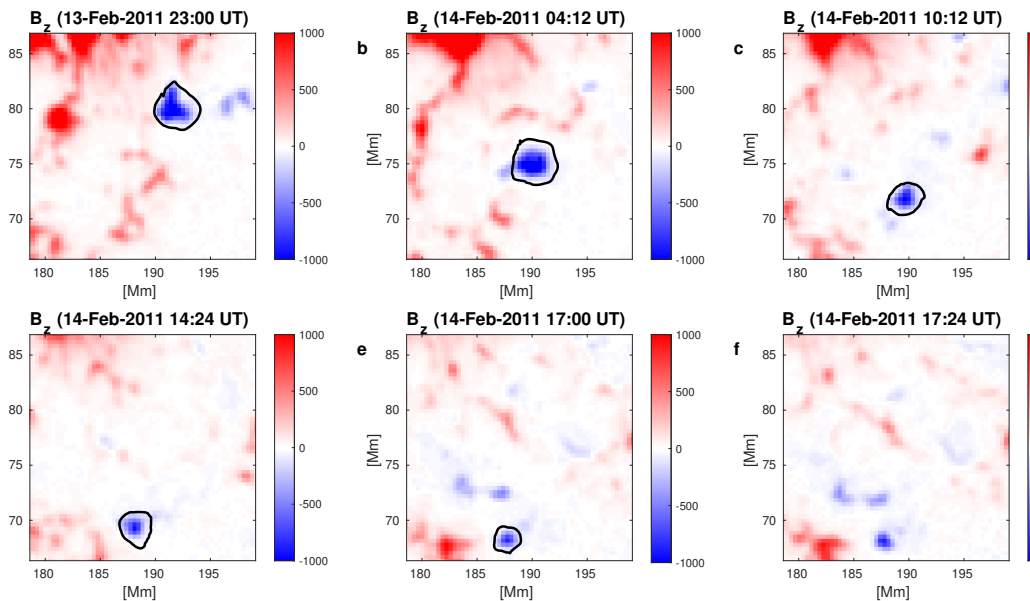
FIGURE 4.29 – B_z component of the magnetic field for the region of active vortex V_M (179-200 Mm × 66-87) at different times. The black contours denote the objective vortex.

Given the intensity of the X-class flare, we concentrate our interest on time evolution of

the objective vortex V_X, associated with such powerful event (JIANG *et al.*, 2011; SUN *et al.*, 2012). With that being said, we analyzed the multiscale behavior of the region containing the related vortex by applying the same methodology proposed in section 4.4.1, using the two dimensional MFDMA method (section 3.4.1, (GU; ZHOU, 2010)) over a 25 hours observation which involves the 16 h lifetime flare. We select the same window size region (151-169 × 90-108 Mm) for the 126 frames of the IACD field. For this new window, we set the scale parameters ($n_i = 5$ and $n_f = N/2$; $-5 \leq q \leq 5$ with $\Delta q = 0.25$ increment, and $\theta = 0$ (BMA)).
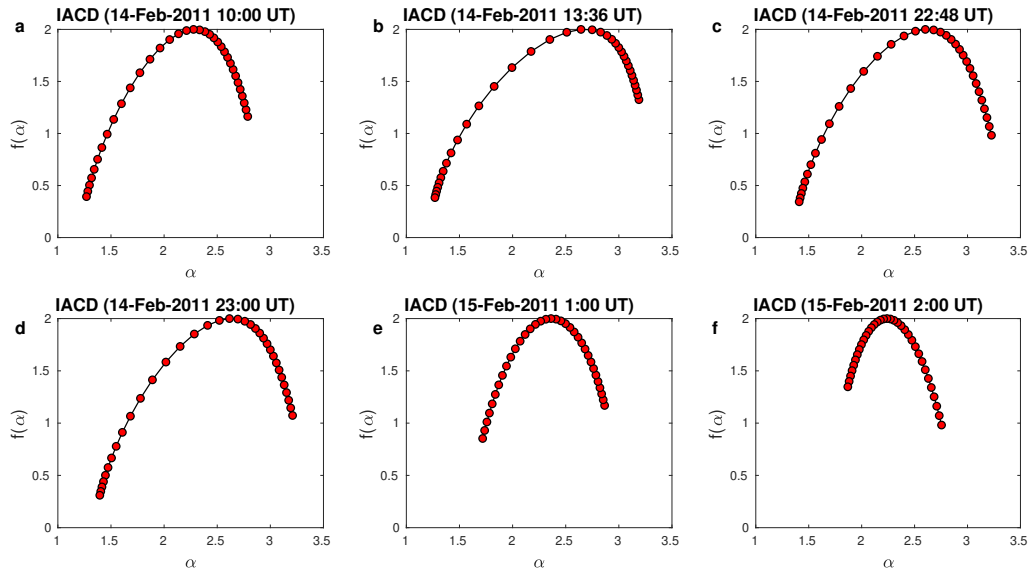
FIGURE 4.30 – Time evolution of multifractal spectrum of IACD field for active vortex V_X region (151-169 × 90-108 Mm). The first frame (a) marks the beginning of the vortex formation and the last one (f) its end.

Figure 4.30 shows the evolution of the multifractal spectrum calculated inside the V_X vortex window. As we can see, the multifractal spectrum remains left asymmetric, i.e., a bigger contribution of large fluctuations for the image multifractality, over all vortex lifetime; but it turns right-skewed, i.e., with a larger contribution to multifractality coming from small fluctuations, just after the vortex vanishing (see, also, Fig. 4.31b). Another important point observed in Figs. 4.30 and 4.31a is the $\Delta\alpha$ size variation through time. Figure 4.31 brings out more precisely the parameters variations observed in the multifractal spectrum (Fig. 4.30) and Renyi exponent. Both $\Delta\alpha$ and R^2 evolution highlight the multifractality growth following the vortex emergence, the first one through the value increase and R^2 via value reduction. For Fig. 4.31a, it is possible to see significant oscillation of $\Delta\alpha$ values before the vortex beginning of ≈ 1.1. However, this value grows to 1.5 at 2011 February 14 10:00 UT and continues to rise for the next 5 hours until it reaches values around 1.8. After that, we see a small decrease (1.4), but followed by a substantial recovery for 6 hours later, with ≈ 1.9 values. Figure 4.31a even shows the intensity

reduction 2 h before the vortex extinction observed at Fig. 4.27 and for Fig. 4.31b, a left-asymmetry reduction until it reaches a transition region with right-asymmetric spectra. These results enhance the idea that such coherent structure contributes to multifractality increase in this region.
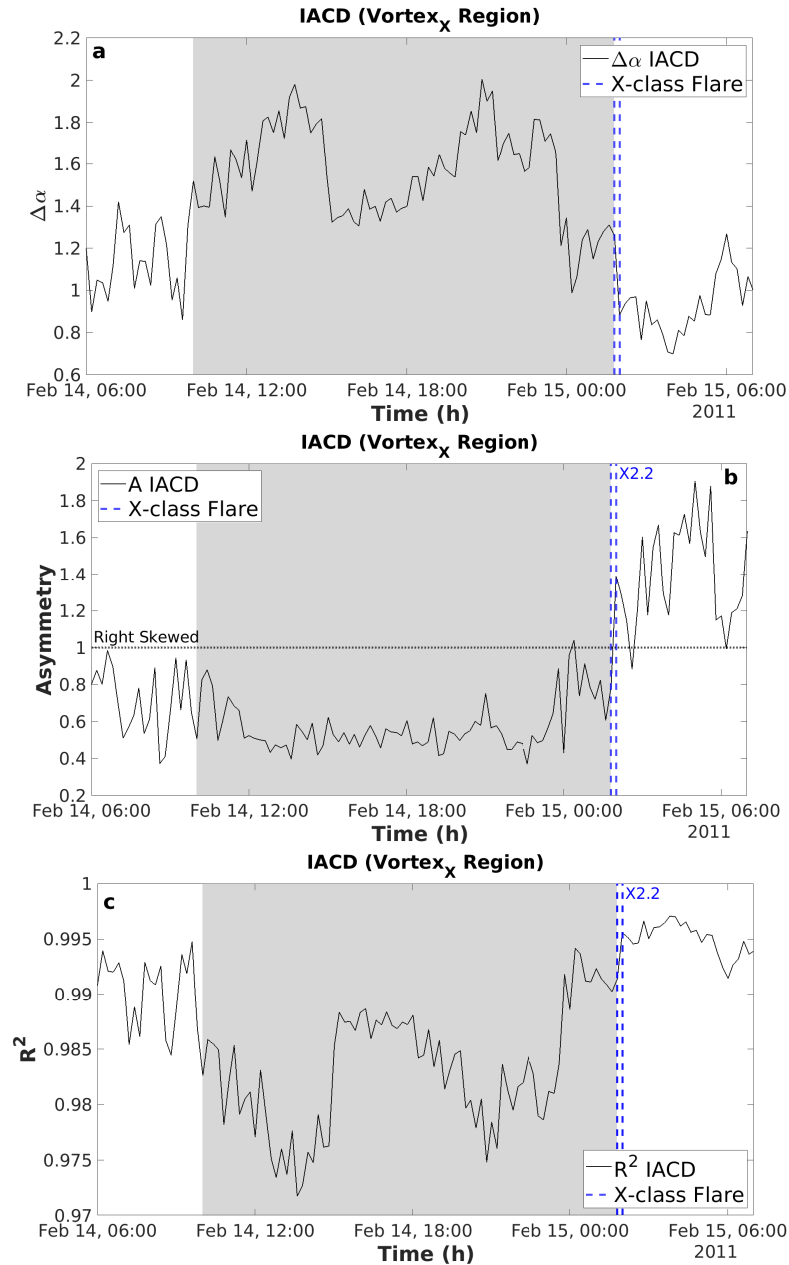
FIGURE 4.31 – Multifractal parameters (Renyi Exponent and Multifractal Spectrum) evolution for IACD field of the vortex V_X region (137-192 × 73-128 Mm) during its activity interval. (a) and (b) represent the $\Delta\alpha$ variation and the α asymmetry respectively (both obtained from singularity spectrum); (c) is the R^2 variation from Renyi exponent. The blue dashed line refers to X2.2-class flare. The gray region represents the vortex lifetime.

Next, we compare the result for $\Delta\alpha$ value evolution over a 25 hours interval with other IACD vortex parameters. Fig. 4.32 shows the temporal evolution of the vortex area, the IACD maximum value ($IACD_{max}$) obtained inside the vortex boundary, and the total

IACD ($IACD_{total}$) (black line) value inside the boundary (blue contour in Fig. 4.27) at each frame. As demonstrated by Fig. 4.32, all three parameters follow the global behavior of $\Delta\alpha$ (red line) during the entire existence of the vortex. In particular, $IACD_{max}$ and $IACD_{total}$ present a noticeable proximity to $\Delta\alpha$ variations, even the intensity reduction at 2011 February 14 14:48 UT. This correlation with the multifractal intensity value suggests that multifractality of each frame is sensitive not only to the vortex dimensions, but also to local intensity of IACD inside the vortex.
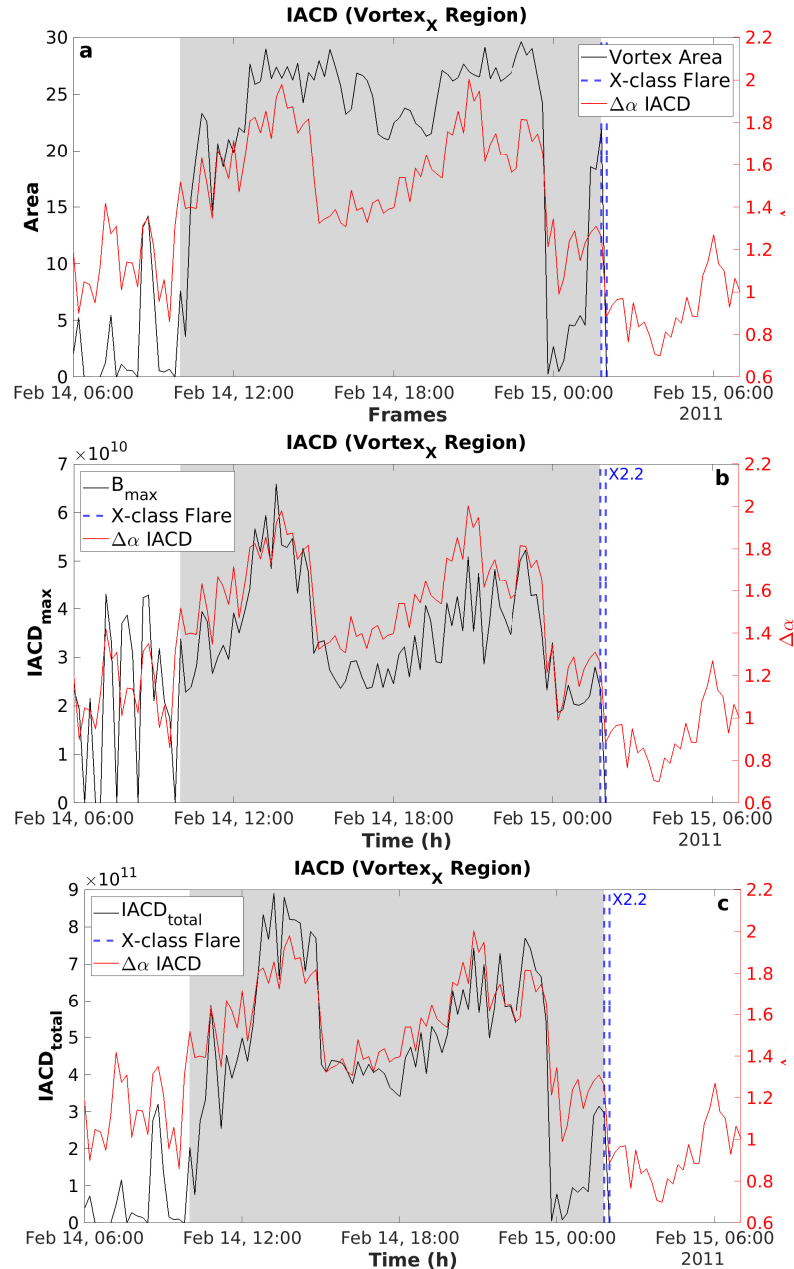
FIGURE 4.32 – Temporal evolution of parameters related to boundary of the objective vortex V_X in the region (137-192 × 73-128 Mm) during the its activity interval. (a) represent the area of the vortex, (b) is the maximum IACD value inside the vortex, and (c) shows the total IACD contained in boundary contour. The red line refers to $\Delta\alpha$ evolution and blue dashed line refers to X2.2-class flare. The gray region represents the vortex lifetime.

5 Conclusion

We have presented a new methodologies for multifractal analysis of solar wind and photospheric magnetic field data. For the solar wind, we employed the MF-DFA, volatility and surrogate time series. The MF-DFA provides a standard way to generate the singularity spectrum and the Renyi exponent; the volatility enhances the extreme events, stressing the differences between series with current sheets and series without current sheets; the surrogate time series provide a way to infer the origin of multifractality (BATISTA *et al.*, 2022). Additionally, the p-model was used to reproduce the multifractal behavior of the solar wind series, indicating that a nonlinear turbulence energy cascade process is behind the observed dynamics. A similar framework for multifractal analysis, but without the volatility and the p-model, was used by CHATTOPADHYAY *et al.* (2018) in the analysis of CME linear speed data in the solar wind.

Just like in GOMES *et al.* (2019), we found the volatility to be very useful to highlight the role of current sheets. In our case, they increase the signature of multifractality due to PDF in the singularity spectra. The surrogate analysis of both original and volatility series shows that for time series with current sheets, multifractality is due to both intermittency and nonlinear correlations; for time series without current sheets, it is predominantly produced by the long-range correlations. The $p-$model analysis reveals that those are mainly nonlinear correlations, since the process behind the statistics is a nonlinear turbulent energy cascade. So, turbulence is the common source of the multifractality, but current sheets are the source of the left asymmetry of the singularity spectrum, as well as the nonlinear scaling exponent for the structure functions. In the absence of current sheets, the small-amplitude fluctuations are the main source of the right asymmetry of the singularity spectrum. It is important to stress that despite being a multifractal process, the current sheet-free series exhibits an almost linear scaling exponent for the structure functions, which is sometimes confused with a monofractal process in the literature. Our results indicate that the Renyi exponent is more sensitive to multifractality due to correlations than the structure function scaling exponent (zeta function).

In dealing with separate cases where the presence or absence of current sheets is considered, we are attacking one of the "nine outstanding questions of solar wind physics", related by VAILL; BOROVSKY (2020), namely, the origin and evolution of the mesoscale

(timescales in the range of minutes up to a few hours) plasma and magnetic-field structure of the solar wind. These current sheets have been associated with the border between adjacent flux tubes (BRUNO, 2019), while also being related to nonlinear turbulent interactions rather than the presence of advected pre-existing flux-tube structures (BOWEN *et al.*, 2018). In the present work, we did not focus on the origin of those coherent structures, but measured their weight on the statistics of solar wind fluctuations. We did this not only through Fourier spectral indices and the scaling of structure functions, as in SALEM *et al.* (2009) , but their contribution to multifractality was explored in depth through the MF-DFA, volatility and surrogate techniques. As we said, our results reveal that although the scaling of the structure functions may be almost linear for series without current sheets, the singularity spectra may still display broad parabolas, the signature of highly multifractal signals. Thus, the scaling exponent of structure functions is adequate to measure multifractality due to PDFs, but not for multifractality due to long-range correlations, where the Renyi exponent and singularity spectra should be adopted.

Considering the results obtained from AR 11158, we once again presented an unprecedented methodology to active regions research. The previous works usually used restricted methods, e.g., WTMM method (MCATEER *et al.*, 2007), and fractal dimension (GEORGOULIS, 2005) to see any possible multifractal behavior in these turbulent regions. The use of the MF-DMA method to process and measure the complexity of active regions brings a new perspective over a possible prediction when linked with LCSs analysis. The results related with multifractal parameters of the magnetograms leads to growth of the multifractality tracking the active region progression. Therefore, our results agree with the results presented at ABRAMENKO; ABRAMENKO (2005). Now, considering the level of self-similarity for pre-flare and post-flare events, e.g. M6.6 and X2.2 flare (GEORGOULIS, 2005; GEORGOULIS, 2013), until the present moment it is not possible to differ both moments. However, if we compare with the region before the flaring activity Fig. 1(4.24), there is a significant variation of parameters.

Furthermore, the results obtained from the IACD method confirm the concepts defined at ZHANG *et al.*; JIANG *et al.*; SONG *et al.* (2007, 2011, 2013). As the papers suggest, the rotation evolution of a negative sunspot deeply relates to objective vortex formation and M2.2 flare formation and fast rotation of the sunspot related to P2 linked to X2.2 flare event. So, we consider that the fast sunspot rotation is responsible for magnetic vortex formation, injecting helicity and shearing in the magnetic fields and giving the needed energy to an extreme flare eruption. As an extra analysis, we observed how the two-dimensional MFDMA is an effective tool to analyse vortical structures and its link with the measurements of intensity of the inner boundary regions of the magnetic vortex.

In conclusion, the apllication of *Integrated Averaged Current Deviation* (IACD) defined by REMPEL *et al.*; REMPEL *et al.* (2016) provides an efficient tool not only for quiet Sun

regimes (CHIAN *et al.*, 2020) but also to active regions, reinforcing the relation of turbulent flows present at the photosphere and lagrangian coherent structures.

Still regarding the multifractal analysis of active regions, it is important to emphasize that we are in the first steps of this exploration. An important improvement to our work would be a comparative analysis with the magnetograms of different AR with high and low levels of magnetic activity and flares. This study would provide a robust confirmation of our preliminary results. Alongside this approach, we are currently applying other nonlinear data analysis methods, such as the *Complex Entropic Form* (ROSA *et al.*, 2000; RAMOS *et al.*, 2000), which measures the disorder in amplitude and phase related to magnetic field components. Finally, we plan to perform a more careful examination of AR 11158 in terms of objective vortex detection and a possible relation with other flare events, e.g. M2.2, M1.0, and M1.6. Positive results would provide strong evidence for the influence of intense sunspot rotation on eruptions.

Bibliography

ABRAMENKO, V. Relationship between magnetic power spectrum and flare productivity in solar active regions. **The Astrophysical Journal**, v. 629, n. 2, p. 1141, 2005.

ABRAMENKO, V. I. Multifractal analysis of solar magnetograms. **Solar Physics**, v. 228, n. 1-2, p. 29–42, 2005.

ABRAMENKO, V. I. *et al.* Scaling behavior of structure functions of the longitudinal magnetic field in active regions on the sun. **The Astrophysical Journal**, v. 577, n. 1, p. 487–495, sep 2002.

ALESSIO, E. *et al.* Second-order moving average and scaling of stochastic time series. **The European Physical Journal B-Condensed Matter and Complex Systems**, v. 27, n. 2, p. 197–200, 2002.

ALVAREZ-RAMIREZ, J.; RODRIGUEZ, E.; ECHEVERRíA, J. C. Detrending fluctuation analysis based on moving average filtering. **Physica A: Statistical Mechanics and its Applications**, v. 354, p. 199–219, 2005. ISSN 0378-4371.

ATTIE, R.; INNES, D.; POTTS, H. Evidence of photospheric vortex flows at supergranular junctions observed by fg/sot (hinode). **Astronomy & Astrophysics**, v. 493, n. 2, p. L13–L16, 2009.

BAI, T.; STURROCK, P. A. Classification of solar flares. **Annual review of astronomy and astrophysics**, v. 27, n. 1, p. 421–467, 1989.

BARRETT, J. P. The coefficient of determination: sme limitations. **The American Statistician**, v. 28, n. 1, p. 19–20, 1974.

BARUNIK, J. *et al.* Understanding the source of multifractality in financial markets. **Physica A**, v. 391, p. 4234–4251, 2012.

BATISTA, L. F. G. *et al.* Origin of multifractality in solar wind turbulence: the role of current sheets. **Monthly Notices of the Royal Astronomical Society**, v. 519, n. 3, p. 3623–3634, 12 2022.

BISKAMP, D. **Magnetohydrodynamic turbulence**. Cambridge: Cambridge University Press, 2003.

BOLZAN, M. J. A.; ROSA, R. R. Multifractal analysis of interplanetary magnetic field obtained during cme events. **Annales Geophysicae**, v. 30, p. 1107, 2012.

BOWEN, T. A. *et al.* Impact of residual energy on solar wind turbulent spectra. **ApJ**, v. 865, p. 45, 2018.

BRANDENBURG, A.; NORDLUND, Å. Astrophysical turbulence modeling. **Reports on Progress in Physics**, v. 74, n. 4, p. 046901, 2011.

BRANDT, P. *et al.* Vortex flow in the solar photosphere. **Nature**, v. 335, n. 6187, p. 238–240, 1988.

BRUNO, R. Intermittency in solar wind turbulence from fluid to kinetic scales. **Earth and Space Science**, v. 6, p. 656, 2019.

BRUNO, R.; CARBONE, V. The solar wind as a turbulence laboratory. **Living Reviews in Solar Physics**, v. 4, 01 2005.

BURLAGA, L. F. Lognormal and multifractal distributions of the heliospheric magnetic field. **Journal of Geophysical Research**, v. 106, p. 15,917, 2001.

CADAVID, A. *et al.* Multifractal models of small-scale solar magnetic fields. **The Astrophysical Journal**, v. 429, p. 391–399, 1994.

CANTOR, G. Ueber unendliche, lineare punktmannigfaltigkeiten. **Mathematische Annalen**, v. 21, p. 545, 1883.

CARBONE, A.; CASTELLI, G.; STANLEY, H. Analysis of clusters formed by the moving average of a long-range correlated time series. **Physical Review E**, v. 69, n. 2, p. 026105, 2004.

CARBONE, V. *et al.* Scaling laws in plasma turbulence. **Rivista del Nuovo Cimento**, v. 27, p. 1–108, 2004.

CARRINGTON, R. C. Description of a singular appearance seen in the sun on september 1, 1859. **Monthly Notices of the Royal Astronomical Society**, v. 20, p. 13–15, 1859.

CHATTOPADHYAY, A.; KHONDEKAR, M. H.; BHATTACHARJEE, A. K. Fractality and singularity in cme linear speed signal: Cycle 23. **Chaos, Solitons and Fractals**, v. 114, p. 542, 2018.

CHIAN, A. C. *et al.* Supergranular turbulence in the quiet sun: Lagrangian coherent structures. **Monthly Notices of the Royal Astronomical Society**, Oxford University Press, v. 488, n. 3, p. 3076–3088, 2019.

CHIAN, A. C. *et al.* Intensification of magnetic field in merging magnetic flux tubes driven by supergranular vortical flows. **Monthly Notices of the Royal Astronomical Society**, Oxford University Press, v. 518, n. 4, p. 4930–4942, 2023.

CHIAN, A. C.-L.; MIRANDA, R. A. Cluster and ace observations of phase synchronization in intermittent magnetic field turbulence: a comparative study of shocked and unshocked solar wind. **Annales Geophysicae**, v. 27, p. 1789–1801, 2009.

CHIAN, A. C.-L. *et al.* Lagrangian chaotic saddles and objective vortices in solar plasmas. **Physical Review E**, APS, v. 102, n. 6, p. 060201, 2020.

CONLON, P. A.; GALLAGHER, P. T. *et al.* Multifractal properties of evolving active regions. v. 248, p. 297–309, 2008.

DONG, Q.; WANG, Y.; LI, P. Multifractal behavior of an air pollutant time series and the relevance to the predictability. **Environmental Pollution**, v. 222, p. 444, 2017.

DUTTA, S.; GHOSH, D.; CHATTERJEE, S. Multifractal detrended fluctuation analysis of human gate deseases. **Frontiers in Physiology**, v. 4, p. 274, 2013.

EKE, A. *et al.* Fractal characterization of complexity in temporal physiological signals. **Physiological measurement**, v. 23, n. 1, p. R1, 2002.

ERMOLLI, I. *et al.* Fractal and multifractal properties of active regions as flare precursors: a case study based on soho/mdi and sdo/hmi observations. **Solar Physics**, v. 289, p. 2525–2545, 2014.

FEDER, J. **Fractals**. [*S.l.*]: Plenum Press, 1988. (Physics of solids and liquids).

FREITAS, D. B. de *et al.* New suns in the cosmos. III. multifractal signature analysis. **The Astrophysical Journal**, v. 831, p. 87, 2016.

FRISCH, U. **Turbulence: The Legacy of A.N. Kolmogorov**. Cambridge: Cambridge University Press, 1995.

GEORGOULIS, M. K. Turbulence in the solar atmosphere: Manifestations and diagnostics via solar image processing. **Solar Physics**, v. 228, p. 5–27, 2005.

GEORGOULIS, M. K. Are solar active regions with major flares more fractal, multifractal, or turbulent than others? **Solar Physics**, v. 276, p. 161–181, 2012.

GEORGOULIS, M. K. Toward an efficient prediction of solar flares: Which parameters, and how? **Entropy**, v. 15, n. 11, p. 5022–5052, 2013.

GOLUB, L.; PASACHOFF, J. M. **Nearest Star: The Surprising Science of our Sun**. 2. ed. [*S.l.*]: Cambridge University Press, 2014.

GOMES, T. F. P. **Eventos Extremos E Estruturas Coerentes Na Turbulência: Estudo De Caso Para O Vento Solar**. Thesis (Doutorado em Geofísica Espacial/Ciências do Ambiente Solar-Terrestre) — Instituto Nacional de Pesquisas Espaciais, Sao Jose dos Campos, 2018.

GOMES, T. F. P. *et al.* Extreme value theory in the solar wind: the role of current sheets. **Monthly Notices of the Royal Astronomical Society**, v. 490, p. 1879, 2019.

GOPINATH, S. Multifractal features of magnetospheric dynamics and their dependence on solar activity. **Astrophysics and Space Science**, v. 361, p. 290, 2016.

GOS, M. *et al.* Dynamics of meteorological time series on the base of ground measurements and retrospective data from merra-2 for poland. **International Journal of Climatology**, v. 41, p. E1531, 2021.

GRIMES, R.; PINTÉR, B. Sunspot rotation in high-and low-flaring active regions. **Solar Physics**, v. 297, n. 8, p. 109, 2022.

GRIMES, R.; PINTÉR, B.; MORGAN, H. Observation of differential rotation within a sunspot umbra during an x-class flare. **Solar Physics**, v. 295, n. 6, p. 87, 2020.

GU, G.-F.; ZHOU, W.-X. Detrending moving average algorithm for multifractals. **Phys. Rev. E**, v. 82, p. 011136, Jul 2010.

GUTBERLET, P. R. M. **Edge structures and turbulence in space plasmas**. Thesis (Post Graduation Course applied in Space Geophysics) — Instituto Nacional de Pesquisas Espaciais, Sao Jose dos Campos, 2011.

HALLER, G. *et al.* Defining coherent vortices objectively from the vorticity. **Journal of Fluid Mechanics**, v. 795, p. 136–173, 2016.

HALSEY, T. C. *et al.* Fractal measures and their singularities: The characterization of strange sets. **Phys. Rev. A**, v. 33, p. 1141, 1986.

HEWETT, R. *et al.* Multiscale analysis of active region evolution. **Solar Physics**, v. 248, p. 311–322, 2008.

HODGSON, R. On a curious appearance seen in the sun. **Monthly Notices of the Royal Astronomical Society**, v. 20, p. 15–16, 1859.

HURST, H.; BLACK, R.; SIMAIKA, Y. **Long-term Storage: An Experimental Study**. London: Constable, 1965.

HURST, H. E. Methods of using long-term storage in reservoirs. **Proceedings of the institution of civil engineers**, v. 5, n. 5, p. 519–543, 1956.

IHLEN, E. Introduction to multifractal detrended fluctuation analysis in matlab. **Frontiers in Physiology**, v. 3, p. 141, 2012.

INNES, D. *et al.* Quiet sun mini-coronal mass ejections activated by supergranular flows. **Astronomy & Astrophysics**, v. 495, n. 1, p. 319–323, 2009.

INOUE, S. *et al.* Magnetic structure producing x-and m-class solar flares in solar active region 11158. **The Astrophysical Journal**, v. 770, n. 1, p. 79, 2013.

IROSHNIKOV, P. Turbulence of a conducting fluid in a strong magnetic field. **Soviet Astronomy**, v. 7, p. 566, 1964.

JIANG, Y. *et al.* Rapid sunspot rotation associated with the x2. 2 flare on 2011 february 15. v. 744, n. 1, p. 50, 2011.

KANTELHARDT, J.; ZSCHIEGNER, S.; KOSCIELNY-BUNDE, E.; BUNDE, A.; HAVLIN, S.; STANLEY, E. Multifractal detrended fluctuation analysis of nonstationary time series. **Physica A**, v. 316, p. 87–114, 2002.

KANTELHARDT, J. W. Fractal and multifractal time series. *In*: MEYERS, R. A. (Ed.). **Mathematics of Complexity and Dynamical Systems**. New York: Springer, 2008. p. 463–487.

KIRAN, K. *et al.* Nonlinear analysis of radial evolution of solar wind in the inner heliosphere. **Solar Physics**, v. 296, p. 23, 2021.

KOGA, D. *et al.* Experimental evidence of phase coherence of magnetohydrodynamic turbulence in the solar wind: Geotail satellite data. **Philosophical Transactions of the Royal Society A: Mathematical, Physical and Engineering Sciences**, v. 366, n. 1864, p. 447–457, 2008.

KOLMOGOROV, A. The local structure of turbulence in incompressible viscous fluid for very large reynolds' numbers. **Akademiia Nauk SSSR Doklady**, v. 30, p. 301, jan. 1941.

KRAICHNAN, R. H. Turbulence of a conducting fluid in a strong magnetic field. **Phys. Fluids**, v. 8, p. 1385, 1965.

LANCASTER, G. *et al.* Surrogate data for hypothesis testing of physical systems. **Physics Reports**, v. 748, p. 1–60, 2018.

LEADBETTER, M. R. Extremes and local dependence in stationary sequences. **Zeitschrift für Wahrscheinlichkeitstheorie und Verwandte Gebiete**, v. 65, p. 291–306, 1983.

LI, A.; LIU, Y. Sunspot rotation and the m-class flare in solar active region noaa 11158. **Solar Physics**, v. 290, p. 2199–2209, 2015.

LI, G. Identifying current-sheet-like structures in the solar wind. **The Astrophysical Journal**, American Astronomical Society, v. 672, n. 1, p. L65–L68, nov 2007.

LI, G. *et al.* Effect of current sheets on the solar wind magnetic field power spectrum from the ulysses observation: From kraichnan to kolmogorov scaling. **Physical Review Letters**, v. 106, n. 12, p. 125001, 2011.

LIU, Y.; CIZEAU, P.; MEYER, M.; PENG, C.-K.; STANLEY, H. E. Correlations in economic time series. **Physica A: Statistical Mechanics and its Applications**, Elsevier BV, v. 245, n. 3-4, p. 437–440, nov 1997.

MACEK, W. M. Multifractality and intermittency in the solar wind. **Nonlinear Processes in Geophysics**, v. 14, p. 695, 2007.

MADANCHI, A. *et al.* Strong short-term non-linearity of solar irradiance fluctuations. **Solar Energy**, v. 144, p. 1, 2017.

MAIWALD, T. *et al.* Surrogate data: a qualitative and quantitative analysis. *In*: DAHLHAUS, R. *et al.* (Ed.). **Mathematical methods in signal processing and digital image analysis**. Berlin: Springer, 2008. p. 41–74.

MANDELBROT, B.; FREEMAN, W. H.; COMPANY. **The Fractal Geometry of Nature**. New York: Henry Holt and Company, 1983. ISBN 9780716711865.

MANDELBROT, B. *et al.* **Multifractals and 1/f Noise: Wild Self-Affinity in Physics (1963–1976)**. New York: Springer, 2014. ISBN 9781461274346.

MANDELBROT, B. B.; NESS, J. W. V. Fractional brownian motions, fractional noises and applications. **SIAM review**, v. 10, n. 4, p. 422–437, 1968.

MANDELBROT, B. B.; WALLIS, J. R. Some long-run properties of geophysical records. **Water resources research**, v. 5, n. 2, p. 321–340, 1969.

MARSCH, E.; TU, C.-Y. Intermittency, non-gaussian statistics and fractal scaling of mhd fluctuations in the solar wind. **Nonlinear Processes in Geophysics**, v. 4, p. 101, 1998.

MCATEER, R. J.; GALLAGHER, P. T.; IRELAND, J. Statistics of active region complexity: A large-scale fractal dimension survey. **The Astrophysical Journal**, v. 631, n. 1, p. 628, 2005.

MCATEER, R. J. *et al.* The bursty nature of solar flare x-ray emission. **The Astrophysical Journal**, v. 662, n. 1, p. 691, 2007.

MENEVEAU, C.; SREENIVASAN, K. R. Simple multifractal cascade model for fully developed turbulence. **Phys. Rev. Lett.**, American Physical Society, v. 59, p. 1424–1427, Sep 1987.

NASA'S SDO Shows Images of Significant Solar Flare. NASA/SDO, 2014. Available at: https://flickr.com/photos/24662369@N07/12771341343. Accessed on: 05/05/2023.

NEELAKSHI, J. **Multifractal analysis and modeling of time series for characterizing nonhomogeneous turbulence in space physics**. Thesis (Doutorado) — Instituto Nacional de Pesquisas Espaciais, Sao Jose dos Campos, 2020.

NEELAKSHI, J. *et al.* Structural characterization of the equatorial f region plasma irregularities in the multifractal context. v. 38, n. 2, p. 445–456, 2020.

NEELAKSHI, J. *et al.* Multifractal characteristics of the low latitude equatorial ionospheric e–f valley region irregularities. **Chaos, Solitons and Fractals**, v. 156, p. 111808, 2022.

NEPOMUCENO, M. M. F. **Natureza fractal e multifractal da onda gravitacional GW150914 detectada pelo LIGO**. Thesis (Doutorado em Física) — Universidade Federal do Rio Grande do Norte, Natal, 2016.

NOROUZZADEH, P.; DULLAERT, W.; RAHMANI, B. Anti-correlation and multifractal features of spain electricity spot market. **Physica A**, v. 380, p. 333, 2007.

OGUNJO, S. T. *et al.* Evolution of dynamical complexities in geospace as captured by dst over four solar cycles 1964–2008. **Journal of Geophysical Research: Space Physics**, v. 126, p. e2020JA027873, 2021.

PARKER, E. N. **Cosmical magnetic fields: Their origin and their activity**. Oxford: Oxford university press, 2019.

PENG, C.-K. *et al.* Mosaic organization of dna nucleotides. **Phys. Rev. E**, v. 49, p. 1685–1689, Feb 1994.

POON, S.-H. **A practical guide to forecasting financial market volatility**. Hoboken: John Wiley & Sons, 2005.

RAMOS, F. M. *et al.* Generalized complex entropic form for gradient pattern analysis of spatio-temporal dynamics. **Physica A: Statistical Mechanics and its Applications**, v. 283, n. 1, p. 171–174, 2000. ISSN 0378-4371.

REMPEL, E. L. *et al.* Objective vortex detection in an astrophysical dynamo. **Monthly Notices of the Royal Astronomical Society: Letters**, v. 466, n. 1, p. L108–L112, 12 2016. ISSN 1745-3925.

REMPEL, E. L. *et al.* Objective magnetic vortex detection. **Phys. Rev. E**, v. 99, p. 043206, Apr 2019.

RENYI, A. **Selected papers of Alfred Renyi**. Budapest: Akademiai Kiado, 1976.

RICHARDSON, L. F. **Weather prediction by numerical process**. Cambridge: University Press, 1922.

ROSA, R. *et al.* Gradient pattern analysis of swift–hohenberg dynamics: phase disorder characterization. **Physica A: Statistical Mechanics and its Applications**, v. 283, n. 1, p. 156–159, 2000. ISSN 0378-4371.

SALAT, H.; MURCIO, R.; ARCAUTE, E. Multifractal methodology. **Physica A**, v. 473, p. 467, 2017.

SALEM, C. *et al.* Solar wind magnetohydrodynamics turbulence: Anomalous scaling and role of intermittency. **The Astrophysical Journal**, v. 702, p. 537, 2009.

SANTOS, A. *et al.* Propriedades multifractais da temperatura do ar diária no nordeste do brasil. **Revista Brasileira de Meteorologia**, v. 34, p. 23–31, 05 2019.

SARKER, A.; MALI, P. Detrended multifractal characterization of indian rainfall records. **Chaos, Solitons and Fractals**, v. 151, p. 111297, 2021.

SCHERRER, P. H. *et al.* The helioseismic and magnetic imager (hmi) investigation for the solar dynamics observatory (sdo). **Solar Physics**, v. 275, p. 207–227, 2012.

SCHRIJVER, C. J. *et al.* Nonlinear force-free field modeling of a solar active region around the time of a major flare and coronal mass ejection. **The Astrophysical Journal**, v. 675, n. 2, p. 1637, 2008.

SCHRIJVER, C. J. *et al.* The 2011 february 15 x2 flare, ribbons, coronal front, and mass ejection: Interpreting the three-dimensional views from the solar dynamics observatory and stereo guided by magnetohydrodynamic flux-rope modeling. **The Astrophysical Journal**, v. 738, 2011.

SEURONT, L. **Fractals and Multifractals in Ecology and Aquatic Science**. Boca Raton: CRC Press/Taylor & Francis, 2010. ISBN 9780429124082.

SHIBATA, K.; MAGARA, T. Solar flares: magnetohydrodynamic processes. **Living Reviews in Solar Physics**, v. 8, p. 1–99, 2011.

SHIMIZU, Y.; THURNER, S.; EHRENBERGER, K. Multifractal spectra as a measure of complexity in human posture. **Fractals**, v. 10, p. 103, 2002.

SILVA, S. S. *et al.* Objective lagrangian vortex detection in the solar photosphere. **The Astrophysical Journal Letters**, v. 863, n. 1, p. L2, aug 2018.

SILVA, S. S. *et al.* Solar vortex tubes: vortex dynamics in the solar atmosphere. **The Astrophysical Journal**, v. 898, n. 2, p. 137, 2020.

SILVA, S. S. *et al.* Solar vortex tubes. ii. on the origin of magnetic vortices. **The Astrophysical Journal**, v. 915, n. 1, p. 24, 2021.

SONG, Q. *et al.* Flares and non-potentiality of ar 11158. **Proceedings of the International Astronomical Union**, v. 8, n. S294, p. 573–574, 2012.

SONG, Q. *et al.* Flares and magnetic non-potentiality of noaa ar 11158. **Research in Astronomy and Astrophysics**, v. 13, n. 2, p. 226, 2013.

SONSRETTEE, W. *et al.* Magnetic field line random walk in isotropic turbulence with zero mean field. **The Astrophysical Journal**, v. 798, n. 1, p. 59, dec 2014.

SORRISO-VALVO, L. *et al.* Sign singularity and flares in solar active region noaa 11158. **The Astrophysical Journal**, v. 801, n. 1, p. 36, 2015.

SUN. NASA/Goddard, 2013. Available at: https://www.nasa.gov/mission_pages/sunearth/science/Sunlayers.html. Accessed on: 05/05/2023.

SUN, X. *et al.* Evolution of magnetic field and energy in a major eruptive active region based on sdo/hmi observation. **The Astrophysical Journal**, v. 748, n. 2, p. 77, 2012.

THEILER, J. *et al.* Testing for nonlinearity in time series: the method of surrogate data. **Physica D: Nonlinear Phenomena**, v. 58, n. 1-4, p. 77–94, 1992.

TORIUMI, S. *et al.* Formation of a flare-productive active region: observation and numerical simulation of noaa ar 11158. **Solar Physics**, v. 289, p. 3351–3369, 2014.

TRUESDELL, C.; NOLL, W.; ANTMAN, S. **The Non-Linear Field Theories of Mechanics**. Berlin: Springer, 2004. (The non-linear field theories of mechanics, v. 3). ISBN 9783540027799.

TSAY, R. **Analysis of Financial Time Series**. Hoboken: Wiley, 2010.

VAILL, N. M.; BOROVSKY, J. E. Nine outstanding questions of solar wind physics. **JGR Space Phys.**, v. 125, p. e2018JA026005, 2020.

VANDEWALLE, N.; AUSLOOS, M. Crossing of two mobile averages: A method for measuring the roughness exponent. **Phys. Rev. E**, v. 58, p. 6832–6834, Nov 1998.

VELTRI, P. Mhd turbulence in the solar wind: self-similarity, intermittency and coherent structures. **Plasma Physics and Controlled Fusion**, v. 41, n. 3A, p. A787, 1999.

VERMA, M. K. Taylor's frozen-in hypothesis for magnetohydrodynamic turbulence and solar wind. **arXiv preprint**, arXiv:2204.12790, 2022.

WAWRZASZEK, A.; ECHIM, M.; BRUNO, R. Multifractal analysis of heliospheric magnetic field fluctuations observed by ulysses. **The Astrophysical Journal**, v. 876, p. 153, 2019.

WIRSING, K.; MILI, L. Multifractal analysis of geomagnetically induced currents using wavelet leaders. **Journal of Applied Geophysics**, v. 173, p. 103920, 2020.

WU, L. *et al.* Testing for the source of multifractality in water level records. **Physica A**, v. 508, p. 824–839, 2018.

XU, L. *et al.* Quantifying signals with power-law correlations: A comparative study of detrended fluctuation analysis and detrended moving average techniques. **Phys. Rev. E**, v. 71, p. 051101, May 2005.

YAN, X.-L.; QU, Z.-Q.; KONG, D.-F. Relationship between rotating sunspots and flare productivity. **Monthly Notices of the Royal Astronomical Society**, v. 391, n. 4, p. 1887–1892, 2008.

YANG, D.; ZHANG, C.; LIU, Y. Multifractal characteristic analysis of near-fault earthquake ground motions. **Soil Dynamics and Earthquake Engineering**, v. 72, p. 12, 2015.

ZHANG, J.; LI, L.; SONG, Q. Interaction between a fast rotating sunspot and ephemeral regions as the origin of the major solar event on 2006 december 13. **The Astrophysical Journal**, v. 662, n. 1, p. L35, 2007.

Annex A - Article

A.1 Article: Origin of multifractality in solar wind turbulence: the role of current sheets

This annex contains the article originally published in the Monthly Notices of the Royal Astronomical Society journal.

Origin of multifractality in solar wind turbulence: the role of current sheets

Leonardo F. Gomes,[1] Tiago F. P. Gomes,[1] Erico L. Rempel[1,2]★ and Sílvio Gama[3]

[1]*Aeronautics Institute of Technology (ITA), São José dos Campos 12228-900, SP, Brazil*
[2]*National Institute for Space Research (INPE), PO Box 515, São José dos Campos 12227-010, SP, Brazil*
[3]*Mathematics Center of the Porto University (CMUP), Mathematics Department, Faculty of Sciences, University of Porto, R. Campo Alegre s/n, P-4169-007 Porto, Portugal*

ABSTRACT

In this work, a multifractal framework is proposed to investigate the effects of current sheets in solar wind turbulence. By using multifractal detrended fluctuation analysis coupled with surrogate methods and volatility, two solar wind magnetic field time series are investigated, one with current sheets and one without current sheets. Despite the lack of extreme-events intermittent bursts in the current sheet-free series, both series are shown to be strongly multifractal, although the current sheet-free series displays an almost linear behaviour for the scaling exponent of structure functions. Long-range correlations are shown to be the main source of multifractality for the series without current sheets, while a combination of heavy-tail distribution and non-linear correlations is responsible for multifractality in the series with current sheets. The multifractality in both time series is formally shown to be associated with an energy-cascade process using the *p*-model.

Key words: turbulence – methods: data analysis – methods: statistical – solar wind.

1 INTRODUCTION

Fractals have been widely employed in non-linear analysis along the past decades as a form of representing the complex topological structures produced by dynamical systems. These topological structures are subsets of the phase space that may represent chaotic attractors, stable or unstable manifolds, boundaries between basins of attraction, etc. Thus, when dynamical systems are investigated through non-linear time series analysis, the fractal indices computed from the time series somehow represent the complexity of the structure of an underlying set on which the solution lies. Additionally, the dynamical structure could be represented by either a monofractal or a multifractal process. A monofractal process has a scaling law for a fluctuation function that is a linear function of statistical moments with a single scaling exponent. A multifractal process has a power-law scaling that is a non-linear function of statistical moments with a range of scaling exponents (Salat, Murcio & Arcaute [2017]). A monofractal scaling is to be expected from dynamical processes behind perfectly self-similar fractal sets, like deterministically generated Cantor sets (Cantor [1883]), or even from white noise time series (Ihlen [2012]); multifractals, on the other hand, are observed in inhomogeneous systems, such as strongly intermittent turbulence, where the presence of strong fluctuations related to coherent structures localized in space generates a departure from Gaussianity in probability distribution functions (PDFs) of small-scale structure functions (Carbone et al. [2004]), as seen in several analyses of observational magnetohydrodynamic (MHD)

data [see e.g. Marsch & Tu ([1998]), Burlaga ([2001]), and Bruno ([2019]) for reviews on turbulence, intermittency, and multifractal scalings in the solar wind].

A series of recent works have confirmed the complex and multifractal nature of solar wind fluctuations. Chang, Tam & Wu ([2004]) studied the origin of complexity in space plasmas using MHD simulations, dynamic renormalization group, and wavelet analysis, arguing that the turbulent plasmas in the solar wind and auroral regions are dominated by a combination of propagating modes and non-propagating intermittent non-linear structures, whose interactions with charged particles may lead to the energization of plasma populations such as auroral ions. Macek ([2007]) employed Voyager magnetic field data in the outer heliosphere and Helios plasma data in the inner heliosphere to show that multifractal spectra of intermittent solar wind fluctuations are consistent with those of the generalized two-scale weighted Cantor set. Bolzan & Rosa ([2012]) analysed magnetic field data from the *ACE* satellite and conjectured that the presence of large-scale coherent structures during coronal mass ejections (CMEs) decreases the multifractality, when compared with periods after the CME events. Wavelet-leader multifractal analysis of magnetospheric dissipations, as measured by the AL index, reveals that the magnetosphere is a multiscale, complex, turbulent system, driven into a non-equilibrium self-organized state, which may explain the observations of repeatable and coherent substorm phenomena with underlying complex multifractal behaviour in the plasma sheet (Valdivia et al. [2013]). The interaction of the solar wind with the Earth's magnetosphere also contributes for multifractality in measurements of the geomagnetic activity, such as the geomagnetic induced current (Wirsing & Mili [2020]) and the Dst index (Ogunjo et al. [2021]), although internal sources of multifractality must also

★ E-mail: erico_rempel@yahoo.com.br

be considered, as Gopinath (2016) suggests that multifractality of the auroral electrojet index is fairly independent of the solar activity cycle. Wawrzaszek, Echim & Bruno (2019) characterized multifractality in intermittent turbulence of heliospheric magnetic field fluctuations from the *Ulysses* spacecraft, concluding that intermittency/multifractality decreases with heliospheric distance, a result that was confirmed by Kiran et al. (2021). Recent analysis of electron density fluctuations in the E–F valley region of the ionosphere performed with the multifractal detrended fluctuation analysis (MF-DFA) method showed that irregularities are multifractal, asymmetric, intermittent, and non-homogeneous (Neelakshi et al. 2022).

The direct link between intermittency and multifractality of magnetic and velocity field fluctuations in the solar wind was made clear in Salem et al. (2009). Using data from the *Wind* spacecraft, they applied the Haar wavelet transform to filter out intermittency from the time series and showed that the scaling exponents for the structure functions behave as a linear function of statistical moments, as in monofractal processes, therefore attributing multifractality in the solar wind to intermittency. Gomes et al. (2019) obtained a similar linear scaling after filtering out the current sheets from Cluster-1 intermittent magnetic field data, suggesting that the current sheets are the coherent structures responsible for the non-linear scaling of the structure functions in the solar wind. This was confirmed after inspection of time series of days when current sheets were absent, which also showed a linear scaling.

A question remained on whether the linear scalings found by Salem et al. (2009) and Gomes et al. (2019) indeed imply that the filtered time series are monofractal or not; i.e. is the non-linearity of the distribution of scaling exponents of structure functions a general measure of multifractality or is it just an indication of intermittency, one among different possible sources of multifractality? One of the goals of the current work is to answer this question. In this sense, it is important to stress that the origin of multifractality is not always related to fat-tailed PDFs, as it may also be caused by different correlations in small and large fluctuations, such as linear or non-linear correlations (Kantelhardt et al. 2002; Wu et al. 2018). The source of multifractality can be investigated by producing surrogates from the original time series. Two types of surrogates are useful in this context (Theiler et al. 1992; Lancaster et al. 2018). First, shuffling the amplitudes of the original signal breaks all long-range correlations, while keeping the PDF unchanged. Therefore, if the multifractality is due to fat-tailed PDFs, it cannot be removed by shuffling the series. If it is due, solely, to time correlations, the corresponding shuffled series will be monofractal. If both fat-tailed PDF and linear/non-linear correlations are present, the multifractality of the shuffled series should be smaller than that of the original series (Barunik et al. 2012). The second type of surrogate is produced by randomizing the phases of the Fourier modes of the original time series, producing a new series with Gaussian PDF, but preserving the linear correlations of the original series. If the random phase time series becomes monofractal, then non-linear correlations and/or non-Gaussian PDFs are the source of multifractality. If the multifractality is preserved in the random phase time series, then linear correlations are its source.

Studies of surrogate time series have been conducted to probe the origin of multifractality in a wide range of contexts, including financial markets (Barunik et al. 2012), human gate diseases (Dutta, Ghosh & Chatterjee 2013), near-fault earthquake ground motions (Yang, Zhang & Liu 2015), solar irradiance fluctuations (Madanchi et al. 2017), air pollutants (Dong, Wang & Li 2017), meteorological time series of air pressure, air temperature and wind speed (Gos et al. 2021), and rainfall records (Sarker & Mali 2021). The surrogate

method was also employed in time series of CME linear speed during solar cycle 23 to conclude that the multifractality is due to both the broad PDF and long-range time correlations (Chattopadhyay, Khondekar & Bhattacharjee 2018). In this paper, we use the method to reveal the role of current sheets in the origin of multifractality in the solar wind. By analysing two qualitatively different magnetic field time series from Cluster-1, one filled with current sheets and another one void of current sheets, we develop a non-linear methodology based on the MF-DFA method coupled with the volatility and surrogate time series. Thus, the contribution of small- and large-scale magnetic fluctuations can be quantified in different types of multifractal solar wind series. It is revealed that when the multifractality is not mainly due to the PDF, the scaling exponents display an almost linear behaviour as a function of the moments of the structure function, despite the presence of strong multifractality in the series. In addition, we employ the *p*-model (Halsey et al. 1986; Meneveau & Sreenivasan 1987) to confirm that the multifractality in both types of solar wind time series can be attributed to a turbulent energy-cascade process.

This paper is organized as follows: In Section 2, the MF-DFA methodology is briefly described; in Section 3, the multifractal analysis of two solar wind time series is conducted, including their volatility time series; Section 4 analyses the surrogate of the original and volatility time series, to determine whether the source of the multifractality in the solar wind is due to PDF or correlations; Section 5 presents the scaling exponent analysis of the original and surrogate times series; and Section 6 describes the *p*-model analysis. Finally, Section 7 presents the conclusions.

2 MF-DFA

The MF-DFA method is a generalization of the DFA method for quantifying long-range correlations in non-stationary time series (Kantelhardt et al. 2002). The method identifies the scaling of *q*th-order moments of the time series (Norouzzadeh, Dullaert & Rahmani 2007). The MF-DFA method consists of the following five steps:

(i) The time series x_k ($k = 1, 2, ..., N$) is integrated:

$$Y(i) = \sum_{k=1}^{i} [x_k - \langle x \rangle], \qquad i = 1, ..., N, \tag{1}$$

where $\langle x \rangle$ is the average value of the data set.

(ii) The series $Y(i)$ is divided into $N_s \equiv \mathrm{int}(N/s)$ non-overlapping segments with equal lengths s. Since N is usually not a multiple of s, some of the data points in the time series may be left out of the last segment. To fix this, the procedure is repeated starting from the opposite end of the time series and going backwards. Consequently, $2N_s$ segments are obtained.

(iii) The local trend for each of the $2N_s$ segments is calculated. Then, the variance is given by

$$F^2(s, \nu) = \frac{1}{s} \sum_{i=1}^{s} \left\{ Y\left[(\nu - 1)\, s + i \right] - y_\nu(i) \right\}^2, \tag{2}$$

for each segment indexed by $\nu = 1, \ldots, N_s$ and

$$F^2(s, \nu) = \frac{1}{s} \sum_{i=1}^{s} \left\{ Y\left[N - (\nu - N_s)\, s + i \right] - y_\nu(i) \right\}^2 \tag{3}$$

for $\nu = N_s + 1, \ldots, 2N_s$, where y_ν is the *m*-th degree fitting polynomial of each segment ν. This polynomial detrending of order *m* in the *Y* profile eliminates trends up to order $m - 1$ in the original time series and specifies the type of MF-DFA applied.

(iv) The average over all segments is calculated to obtain the qth-order fluctuation function:

$$F_q(s) = \left\{ \frac{1}{2N_s} \sum_{v=1}^{2N_s} [F^2(s,v)]^{\frac{q}{2}} \right\}^{\frac{1}{q}}, \qquad (4)$$

where, in general, the q parameter can take any real value except zero. For $q = 2$, the equation returns the DFA method. Steps 2–4 are repeated for different time-scales s.

(v) The scaling behaviour of the fluctuation function is defined by the log–log plot of $F_q(s) \times s$ for each value of q. If x_i have long-range correlations, for large values of s, $F_q(s)$ increases as a power law,

$$F_q(s) \sim s^{h(q)}. \qquad (5)$$

The scaling exponents $h(q)$ are the generalized Hurst exponents, defined as the slope of the $\log F_q(s) \times \log(s)$ graph, where for $h(2)$ we have the standard Hurst Exponent (Hurst, Black & Simaika 1965). For positive values of q, $h(q)$ describes the scaling behaviour of segments with large fluctuations and for negative values of q, $h(q)$ describes the scaling behaviour of segments with small fluctuations. For monofractal series, $h(q)$ is independent of q, but for multifractal series $h(q)$ depends on q. The generalized Hurst exponent is directly related to the Renyi exponent (Renyi 1976) $\tau(q)$ by

$$\tau(q) = q\, h(q) - 1. \qquad (6)$$

Besides $h(q)$, another way to characterize the multifractality of a time series is by the singularity spectrum $f(\alpha)$, which is related to $\tau(q)$ via a Legendre transform,

$$\alpha = \tau'(q) \quad \text{and} \quad f(\alpha) = q\,\alpha - \tau(q), \qquad (7)$$

where α is the singularity exponent. This $f(\alpha) \times \alpha$ relation represents the multifractal spectrum and has a concave parabolic shape.

From the multifractal spectrum, it is possible to obtain a set of parameters to characterize each series: (i) the α value where $f(\alpha)$ is maximum, α_0; (ii) the α width, $\Delta\alpha = \alpha_{max} - \alpha_{min}$, where α_{min} and α_{max} are, respectively, the minimum and maximum values of α that mark the base of the concave parable in the multifractal spectrum ($\Delta\alpha$ is a measure of multifractal strength); and (iii) the asymmetry parameter:

$$A = \frac{\alpha_{max} - \alpha_0}{\alpha_0 - \alpha_{min}}, \qquad (8)$$

where $A = 1$ means that the spectrum is symmetric, for $A > 1$ the spectrum is right-skewed asymmetric, and for $A < 1$ the spectrum is left-skewed asymmetric (Shimizu, Thurner & Ehrenberger 2002; de Freitas et al. 2016). A multifractal spectrum with a long right tail has a greater contribution from small fluctuations. By contrast, a multifractal spectrum with left asymmetry has a greater influence by local fluctuations with large values (Ihlen 2012).

Another useful multifractal parameter can be extracted from the $\tau(q) \times q$ relation. As can be seen from equation (6), $\tau(q)$ has a linear dependence with q for monofractal series, where $h(q)$ is constant. In contrast, for multifractal series, this dependence is non-linear. The q dependence of the Renyi exponent can be quantified by the coefficient of determination, R^2. R^2 measures the proportion of the variance for a dependent variable that is predictable by an independent variable in a linear regression model (Barrett 1974). The coefficient of determination is given by

$$R^2 = 1 - \frac{\sum_{i=1}^{n}(\tau_i - \hat{\tau}_i)^2}{\sum_{i=1}^{n}(\tau_i - \bar{\tau})^2}, \qquad (9)$$

where $\tau_i = \tau(q_i)$ is the observed dependent variable, $\hat{\tau}_i$ is the corresponding predicted value, and $\bar{\tau}$ is the mean of the observed data. R^2 varies from 0 to 1, where in our case 1 represents a perfect fit to the linear dependence model. In other words, the measure of R^2 for the $\tau(q) \times q$ relation will be closer to 0 for multifractal series and closer to 1 for monofractal series.

The MF-DFA method has best results if the time series are reasonably stationary, i.e. if they have a noise-like structure. As suggested by Eke et al. (2002), it is possible to determine whether the time series have noise-like structure by computing a monofractal DFA prior to conducting the MF-DFA analysis. Time series are noise like if their Hurst exponent $h(2)$ is between 0 and 1, and they are random walk like (non-stationary) if $h(2)$ is above 1. Ihlen (2012) suggests that time series with $h(2)$ above 1.2 should be differentiated before application of the MF-DFA analysis.

3 MULTIFRACTAL ANALYSIS OF SOLAR WIND DATA

We analyse solar wind magnetic field data detected with the Fluxgate Magnetometer onboard Cluster-1, with 22 Hz sampling frequency. Two time series with 24 hours are investigated, one from 2008 March 9 and one from 2016 January 25. To reduce the computational time of the analysis, the data length has been reduced by using a decimation process. The low-pass Chebychev Type I infinite impulse response filter was used with a reduction factor $M = 10$, order 8, and 0.8/M cut-off frequency. This decimation process is described in Gomes et al. (2019).

After decimating the time series, we apply the MF-DFA method with four input parameters: minimum scale s_i, maximum scale s_f, order of fluctuation function q, and polynomial order m. The scale refers to multiple segment sizes of the cumulative series and varies from a minimum segment size s_i to a maximum s_f. In this work, we use $s_i = 10$ and $s_f = N$, where N is the length of the time series; q varies between -20 and 20 with an increment of $\Delta q = 0.25$, and $m = 3$. This choice of parameters was supported by several tests. The recommendation for large time series is to use a polynomial trend order around $m = 3$; $s_f = N$ was chosen to avoid deformations in the shape of the multifractal spectra. Meanwhile, for the q parameter the use of values larger than 20 does not change the shape of the spectra significantly.

3.1 MF-DFA analysis of the |B| time series

Fig. 1 shows the solar wind magnetic field time series studied in this section for days 2008 March 9 and 2016 January 25. In the upper panel, the time series for 2008 March 9 (red) and its first-order differencing (black) are shown. As it was explained in the previous section, time differencing is necessary in this case due to the high non-stationarity of this series [$h(2) = 1.23$]. Throughout the remaining of this section, only the differenced time series will be used for March 9. This time series was characterized by Gomes et al. (2019) as being permeated by large-scale current sheets. The green regions in the original time series denote current sheets found with Li's method (Li 2008). The lower panel shows the time series for 2016 January 25, which is characterized by a higher degree of stationarity and the absence of current sheets (Gomes et al. 2019). Due to its higher stationarity [$h(2) = 0.96$], there is no need to perform a differencing in this series.

Fig. 2 shows different multifractal measures of the two magnetic field time series. Fig. 2(a) shows the multifractal spectra, which reveal a left asymmetry for the March 9 time series (red) and a
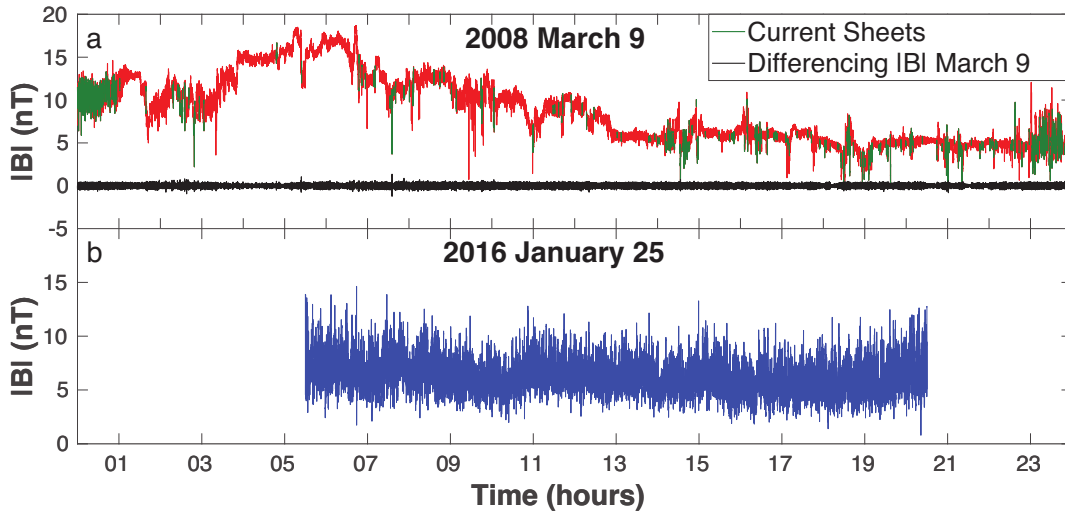
Figure 1. Solar wind time series of |***B***| measured by Cluster-1: (a) for 2008 March 9 (red), containing current sheets (green), and its first-order differencing (black); and (b) for time series of |***B***| for 2016 January 25 (blue), without current sheets.
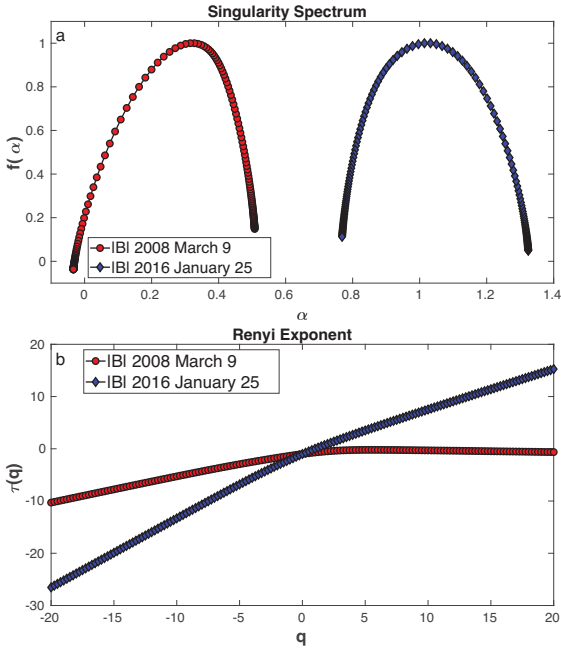

Figure 2. (a) Multifractal spectrum of |***B***| for 2008 March 9 (red) and 2016 January 25 (blue). (b) Renyi exponents for 2008 March 9 (red) and 2016 January 25 (blue).

right asymmetry for the January 25 series (blue). The left asymmetry indicates the stronger contribution to multifractality coming from large fluctuations associated with values of $q > 0$ in the intermittent time series of the current sheet-filled time series of March 9; the right asymmetry found for the current sheet-free time series of January 25 points to the greater contribution of small fluctuations to the multifractality (Ihlen 2012). The width of the spectrum can be used as a measure of the degree of multifractality of the series (Shimizu et al. 2002). Comparing both spectra, it can be seen that they have almost the same width ($\Delta\alpha \approx 0.541$ for March 9 and $\Delta\alpha \approx 0.555$ for January 25), which may be surprising, since the time series of March 9 is visibly more intermittent, with strong bursts randomly

interspersed in time. In this case, the difference in multifractality can be better quantified by the Renyi exponent $\tau(q)$, shown in Fig. 2(b). It reveals a non-linear behaviour for both series, but with $R^2 \approx 0.804$ for March 9 and $R^2 \approx 0.986$ for January 25; thus, March 9 displays higher multifractality.

3.2 MF-DFA analysis of the volatility time series

In the previous section, the degree of multifractality, as provided by the width of the multifractal spectra, could not properly distinguish between the two time series under investigation, which is unexpected, given that the original series are not only visually very different, but one of them is known to be permeated by coherent structures (current sheets) and the other is not. This is probably because although the differenced time series of 2008 March 9 is apparently more intermittent than the series of 2016 January 25, most of the abrupt changes in |***B***| caused by the current sheets in the March 9 series have a small amplitude and, therefore, do not produce strong bursts in the time-differenced series. Such abrupt changes in |***B***| can be enhanced by employing the volatility, thus providing a way to investigate the role of current sheets in the multifractality. In the present section, we employ the volatility to enhance the distinct features of each series due to current sheets before repeating the MF-DFA analysis.

The magnetic volatility, $\mathrm{vol}_{\mathrm{mag}}$, can be calculated from the standard deviations of the log magnetic return $\Delta r_{\mathrm{mag}}(t)$ in a moving window of length ω along N sample points (Tsay 2010)

$$\Delta r_{\mathrm{mag}}(t) = \log\left(\frac{|\mathbf{B}(t+\tau)|}{|\mathbf{B}(t)|}\right), \tag{10}$$

$$\mathrm{vol}_{\mathrm{mag}}(j) = \sqrt{\frac{1}{\omega-1}\sum_{i=j}^{\omega+j-1}(\Delta r_{\mathrm{mag}}(i) - \mu(j))^2}, \tag{11}$$

where τ is a time lag, $j = 1, \ldots, N - \omega + 1$, and $\mu(j)$ is the mean Δr_{mag} inside the window (Gomes et al. 2019). Note that since Δr_{mag} involves computing a time difference with lag τ, there is no need to difference the original time series to remove non-stationarities prior to computation of the volatility. The ω and τ values are estimated from the power spectrum density (PSD). Fig. 3(a) shows the PSD for the March 9 time series, where the inertial range is the blue region between the dashed lines. This region was chosen as the
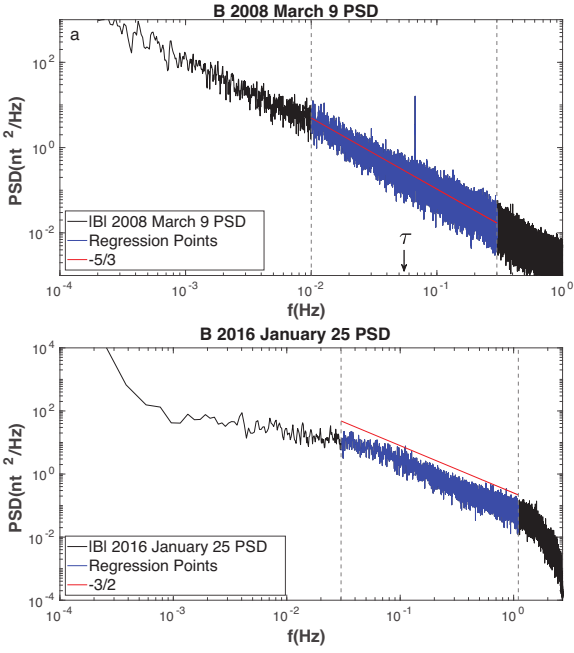
Figure 3. Power spectral density for solar wind magnetic field of (a) 2008 March 9 and (b) 2016 January 25. The blue region is the inertial range and the red line is the linear fit for this interval, with a slope equal to $-5/3$ for March 9 and slope $-3/2$ for January 25.
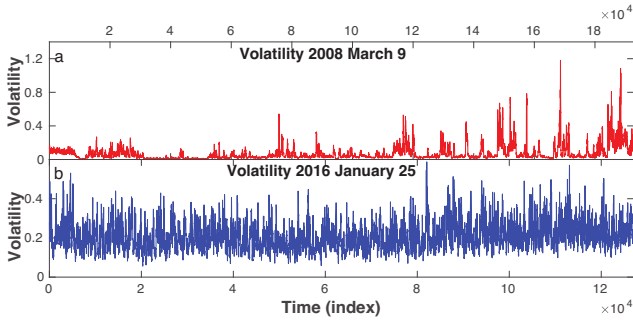

Figure 4. Volatility of solar wind magnetic field time series for (a) 2008 March 9 and (b) 2016 January 25.

frequency interval where the slope of the fitted line is $-5/3$, following Kolmogorov's K41 theory (Kolmogorov 1941) for fully developed turbulence (Frisch 1995). The frequency in the middle of the inertial range marks the scale used to define both τ and ω. It is also the scale used in Li's method to detect the current sheets, shown in Fig. 1. In this way, we define $\tau = \omega = 50 s$. Fig. 3(b) shows the PSD for the January 25 series.

Fig. 4 exhibits the volatility time series for 2008 March 9 (upper panel, red) and for 2016 January 25 (lower panel, blue) from the decimated magnetic field data. Recall that the upper series has many current sheets, while the lower one has none. Note that, unlike the January 25 series, the March 9 volatility series has several extreme events. Most of these high peaks are due to the abrupt changes in the magnetic field that take place when the satellite crosses a current sheet in the solar wind, as evidenced by the coincidence between extreme events in the volatility and current sheets detected by Li's method (see figs 2a and b in Gomes et al. 2019). As a consequence, the multifractal spectra obtained from the volatility of both series are very different, as seen in Fig. 5(a). Now, the spectrum of the intermittent time series of
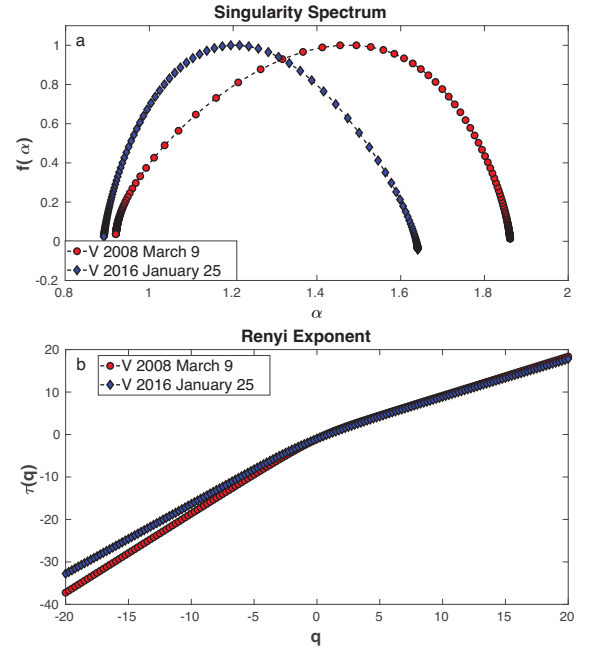
Figure 5. (a) Multifractal spectra for the volatility in 2008 March 9 (red) and 2016 January 25 (blue). (b) Renyi exponents for the volatility in 2008 March 9 (red) and 2016 January 25 (blue).

March 9 is much broader than the one from January 25. The α width is $\Delta\alpha = 0.941\,34$ for March 9 and $\Delta\alpha = 0.749\,21$ for January 25. The volatility has enhanced the contribution of the extreme events due to current sheets, thus showing the signature of coherent structures present in the solar wind that were partially hidden in the multifractal analysis of the original time series. The Renyi exponents are shown in Fig. 5(b); once again, the curve for March 9 is more concave than for January 25, reflecting its higher level of multifractality. The coefficient of determination for the Renyi exponents is $R^2 = 0.974\,64$ for the volatility of March 9 and $R^2 = 0.981\,25$ for the volatility of January 25. It is clear that the volatility has highlighted the role of current sheets in the multifractal singularity spectrum.

4 MF-DFA OF SURROGATE TIME SERIES

According to Madanchi et al. (2017), there are two features in a time series that can lead to its multifractality: (i) the presence of heavy-tailed PDFs, as in highly intermittent series, and (ii) the existence of linear and non-linear correlations. In this section, we try to identify the origin of the multifractality in the solar wind by means of two surrogate time series derived from the original $|B|$ data. As mentioned in the introduction, the shuffled time series is a random permutation of the original time series in the real space that destroys all temporal correlations, while keeping the same PDF for the amplitudes of $|B|$. On the other hand, the random phase surrogate is generated from the Fourier transform of the original $|B|$ series. A new Fourier series is generated by shuffling the phases of the Fourier modes while keeping their power spectrum (Maiwald et al. 2008). The inverse Fourier transform of this new frequency spectrum is the random phase surrogate, which keeps the power spectrum and linear autocorrelation of the original series, but has a Gaussian PDF and breaks the non-linear correlations. After generating these two surrogates, we repeat the multifractal analysis described in the previous section; if the shuffled surrogate has a multifractal spectrum that is considerably

Figure 6. Differenced time series for 2008 March 9 (red) and the respective surrogates: shuffled (green) and random phases (magenta).

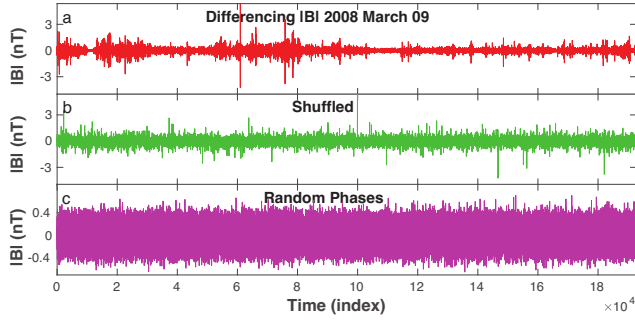narrower than the spectrum of the original series, it means that time correlations are an important source of multifractality in the original time series. If the random phase surrogate has a multifractal spectrum that is considerably narrower than the spectrum of the original series, it means that fat-tailed PDFs and/or non-linear correlations are important for the multifractality. Note that both kinds of multifractality mentioned above can be simultaneously present in a time series (Norouzzadeh et al. 2007; Madanchi et al. 2017). If both the shuffled and random phase surrogates produce monofractal spectra, then non-linear correlations (but not fat-tailed PDFs) are the source of multifractality. In the following subsections, we perform this analysis for both the |$\boldsymbol{B}$| and volatility time series of 2008 March 9 and 2016 January 25.

4.1 Magnetic field time series, 2008 March 9

Fig. 6 shows the differenced time series of |$\boldsymbol{B}$| for March 9 (red) with its shuffled (green) and random phase (magenta) surrogates. Clearly, the shuffled surrogate keeps the extreme events of the differenced |$\boldsymbol{B}$| series, but the same events are absent from the random phase surrogate.

Fig. 7(a) displays the multifractal spectra for the March 9 original and surrogate time series. For the shuffled spectrum (green), we see a small reduction in the width when compared with the original one (red). This means that there is a contribution from correlations to multifractality, along with the contribution of the PDF. Considering the random phase spectrum (magenta), its width reduces drastically (the $\Delta\alpha$ variation is about 0.32), which points to a significant contribution to multifractality coming from a non-Gaussian DF and/or non-linear correlations. The conclusion from both spectra is that the PDF has the strongest contribution to multifractality. The contribution of the PDF is due to the presence of strong intermittent bursts (extreme events) in the March 9 time series. Since these bursts have been shown to be related to large current sheets (see Gomes et al. 2019), the current sheets can be seen as the origin of most of the multifractality in this time series. Fig. 7(b) confirms this conclusion by showing the Renyi exponent as a function of q, where the random phase surrogate has a smaller concavity than the shuffled surrogate.

4.2 Magnetic field time series, 2016 January 25

Fig. 8 shows the time series for January 25 (blue) with its shuffled (green) and random phase (magenta) surrogates. Fig. 9(a) shows a significant width reduction in both surrogate spectra in comparison with the original volatility spectrum (blue). The spectrum of the shuffled series (green) has a width $\Delta\alpha = 0.194$, indicating a difference of 0.36 with the spectrum of |$\boldsymbol{B}$|. Similarly, the spectrum

Figure 7. (a) Multifractal spectrum of |$\boldsymbol{B}$| for 2008 March 9 (red) and the respective surrogates: shuffled (green) and random phases (magenta). (b) Renyi exponents for 2008 March 9 (red) and the respective surrogates: shuffled (green) and random phases (magenta).

Figure 8. Time series for 2016 January 25 (blue) and the respective surrogates: shuffled (green) and random phases (magenta).

for the random phase series has a small width, about $\Delta\alpha = 0.32$, a difference of 0.23 with the spectrum of |$\boldsymbol{B}$|. So, there is strong influence from long-range correlations as well as non-Gaussianity on the January 25 magnetic field multifractality, but the contribution of the correlations is preponderant, since the shuffled spectrum is considerably narrower than the random phase spectrum.

4.3 Volatility time series, 2008 March 9

We proceed with the analysis of the origin of the multifractality for March 9 using the volatility, as shown in Fig. 10 for the original (red), shuffled (green), and random phase (magenta) time series. The corresponding multifractal spectra in Fig. 11(a) show a wide parabola for the original volatility series (red) and two narrower parabolas related to its shuffled (green) and random phase (magenta) series. The random phase spectrum has a width of about $\Delta\alpha = 0.39$ and the shuffled spectrum has a width of $\Delta\alpha = 0.35$. Since both spectra have approximately the same width, it shows an important

Figure 9. (a) Multifractal spectrum for 2016 January 25 (blue) and the respective surrogates: shuffled (green) and random phases (blue). (b) Renyi exponents for 2016 January 25 (blue) and the respective surrogates: shuffled (green) and random phases (magenta).

Figure 10. Time series volatility for 2008 March 9 (red) and the respective surrogates: shuffled (green) and random phases (blue).
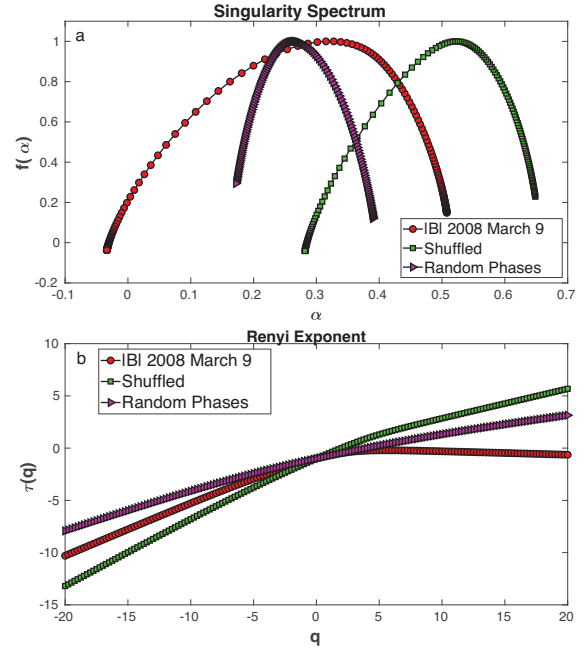

Figure 11. (a) Multifractal spectrum for the volatility of 2008 March 9 (red) and the respective surrogates: shuffled (green) and random phases (magenta). (b) Renyi exponents for the volatility of 2008 March 9 (red) and the respective surrogates: shuffled (green) and random phases (magenta).
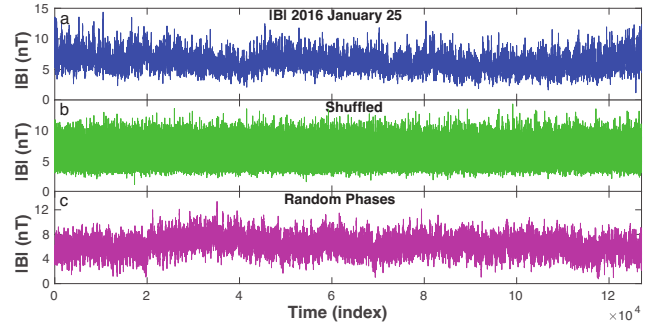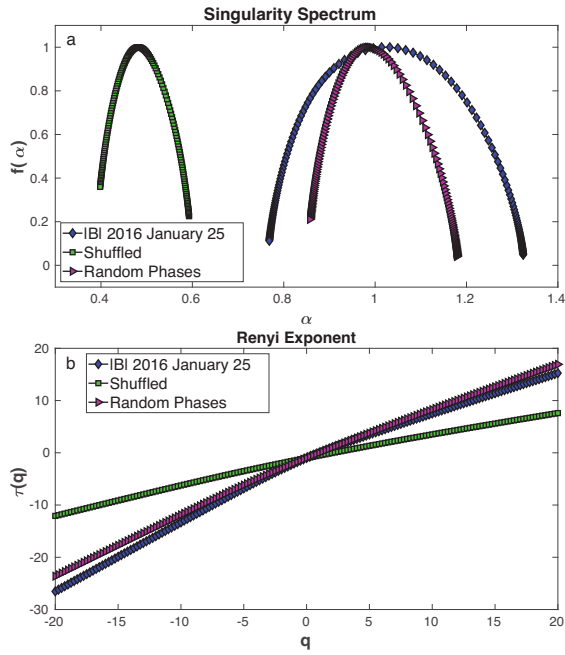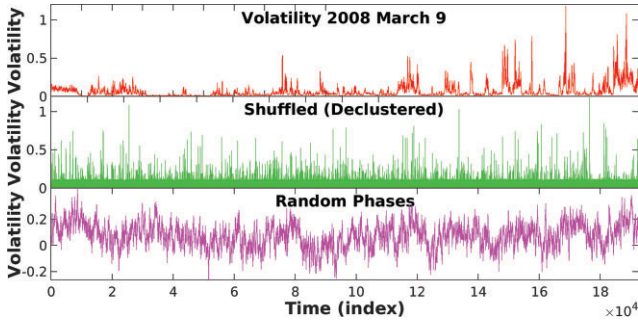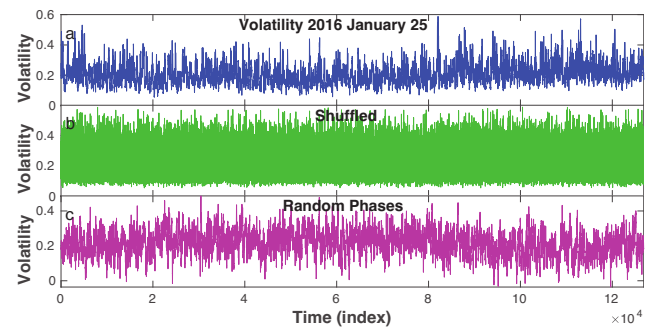

Figure 12. Time series of the volatility for 2016 January 25 (blue) and the respective surrogates: shuffled (green) and random phases (magenta).

feature that was not so clear from the multifractal spectra of the $|\mathbf{B}|$ surrogate series (Fig. 7), that is, the importance of the non-linear correlations, which play a key role, together with the PDF, in the origin of the multifractality for the March 9 series. Since the volatility is computed with a lag time of $\tau = 50s$, it is better suited for measuring the relevance of long-range non-linear correlations than the time-differenced $|\mathbf{B}|$ series. Fig. 11(b) confirms that the shuffled and random phase series have almost linear Renyi exponents; thus, the series are closer to monofractal.

4.4 Volatility time series, 2016 January 25

Fig. 12 shows the volatility time series of the January 25 time series (blue) and its shuffled (green) and random phase (magenta) surrogates. Fig. 13(a) shows the corresponding multifractal spectra. Once again, the reduction in the width for both surrogate spectra means that a mutual contribution to multifractality coming from long-range correlations and non-Gaussianity is present, with a

clear predominance of the long-range correlations effects, since the shuffled spectrum is much narrower than the random phase spectrum.

A quantitative comparison of all the results for the $|\mathbf{B}|$ time series and volatility time series of March 9 and January 25 is provided by Tables 1–3. Table 1 shows R^2 for the Renyi exponent of $|\mathbf{B}|$ and its volatility for March 9 and January 25; Table 2 shows the width of the multifractal spectra, $\Delta\alpha$; Table 3 shows the asymmetry of the spectra, A. In general, all spectra for January 25 are right-asymmetric due to the importance of small-scale fluctuations; for March 9, some spectra are left-asymmetric due to the importance of large-scale fluctuations, but the random phases show right asymmetry, since in the random phase surrogate the effects of non-Gaussian PDFs are destroyed.

5 ZETA FUNCTION

Another function typically employed in multifractal analyses of time series is the zeta function. Consider the structure function for $|\mathbf{B}|$
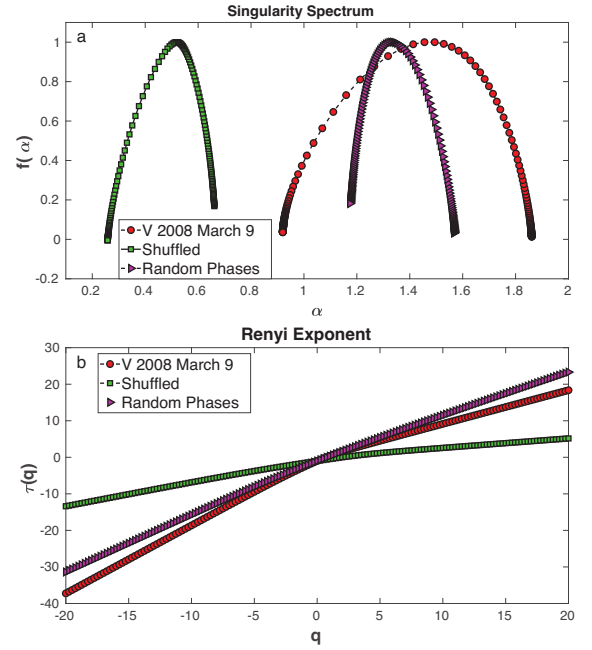
Figure 13. (a) Multifractal spectrum for the volatility of 2016 January 25 (blue) and the respective surrogates: shuffled (green) and random phases (magenta). (b) Renyi exponents for the volatility of 2016 January 25 (blue) and the respective surrogates: shuffled (green) and random phases (magenta).
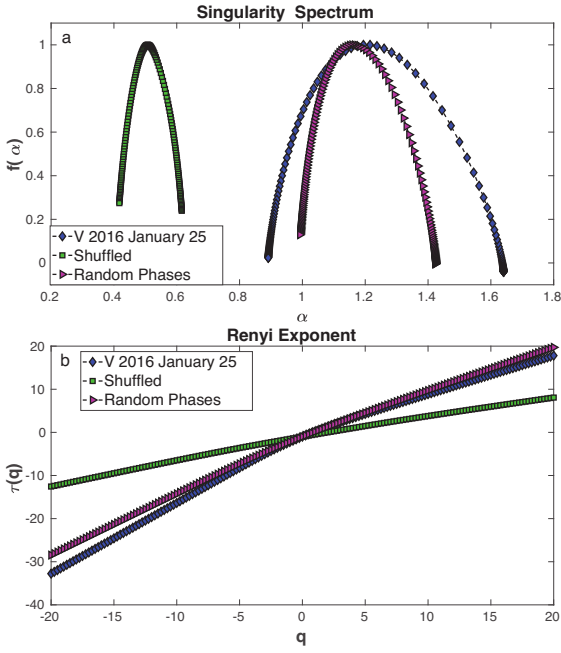
Table 1. R^2 of the Renyi exponent for magnetic field and volatilities of 2008 March 9 and 2016 January 25.

	March 9		January 25	
	$|\boldsymbol{B}|$	Volatility	$|\boldsymbol{B}|$	Volatility
Original	0.804 13	0.974 64	0.985 97	0.981 25
Shuffle	0.975 05	0.967 48	0.995 37	0.995 73
Random phases	0.981 85	0.996 37	0.996 01	0.994 24

Table 2. Width of α, $\Delta\alpha$, for magnetic field and volatilities of 2008 March 9 and 2016 January 25.

	March 9		January 25	
	$|\boldsymbol{B}|$	Volatility	$|\boldsymbol{B}|$	Volatility
Original	0.541 12	0.941 34	0.555 68	0.749 21
Shuffle	0.366 63	0.403 32	0.194 68	0.198 73
Random phases	0.218 02	0.392 99	0.321 81	0.430 88

Table 3. Spectrum asymmetry, A, for magnetic field and volatilities of 2008 March 9 and 2016 January 25.

	March 9		January 25	
	$|\boldsymbol{B}|$	Volatility	$|\boldsymbol{B}|$	Volatility
Original	0.498 73	0.638 85	1.107 09	1.312 15
Shuffle	0.512 79	0.533 42	1.308 54	1.182 83
Random phases	1.335 83	1.418 17	1.459 99	1.470 02

(Frisch 1995):

$$S_p(\tau) = \langle [|\boldsymbol{B}(t + \tau)| - |\boldsymbol{B}(t)|]^p \rangle, \tag{12}$$

where $\langle \cdot \rangle$ is the time average, τ is the time lag, and p are the statistical moments for the time series of $\boldsymbol{B}$. Assuming scale invariance inside
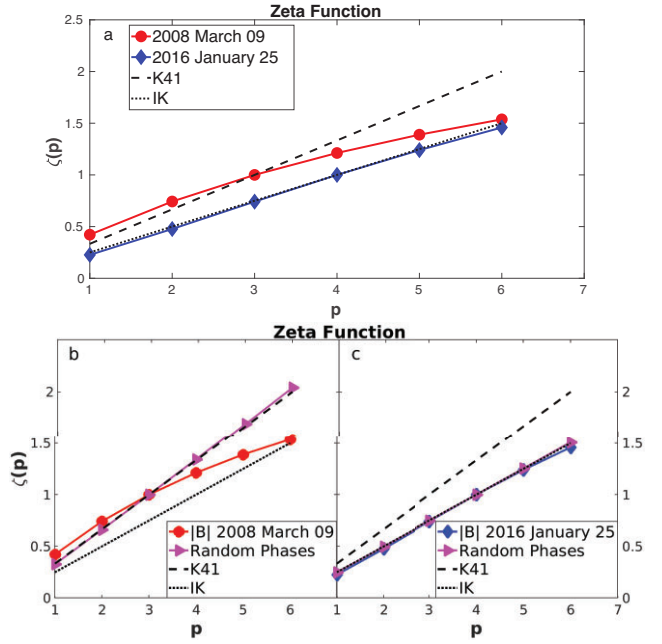
Figure 14. (a) Zeta functions for the magnetic field time series for 2008 March 9 (red circles) and 2016 January 25 (blue diamonds). (b) Zeta functions for $|\boldsymbol{B}|$ 2008 March 9 (red circles) and its random phases (magenta triangles). (c) Zeta functions for $|\boldsymbol{B}|$ 2016 January 25 (blue diamonds) and its random phases (magenta triangles). The dashed lines represent the K41 scaling and the dotted lines represent the IK scaling.

the inertial range, S_p follows a power law

$$S_p(\tau) \sim \tau^{\zeta(p)}, \tag{13}$$

where $\zeta(\cdot)$ is the zeta function or scaling exponent of the structure function. So, $\zeta(p)$ is obtained by the slope of the $\log S_p(\tau) \times \log \tau$ plot. The importance of this parameter comes from Kolmogorov's K41 theory (Kolmogorov 1941) and the Iroshnikov–Kraichnan (IK) theory (Iroshnikov 1964; Kraichnan 1965) of self-similarity and scale invariance inside the inertial range for a homogeneous and isotropic turbulence, where the ζ function was shown to be a linear function of p, with $\zeta(p) = p/3$ for K41 and $\zeta(p) = p/4$ for IK.

In Fig. 14(a), the linear K41 theoretical zeta scaling exponent function is shown by the black dashed line, while the IK scaling exponent is denoted by a dotted line. The top panel (a) also shows the zeta scaling exponent computed from the time series of $|\boldsymbol{B}|$ for the intermittent series of March 9 (red line with circles) and for the current sheet-free series of January 25 (blue line with diamonds). The zeta function for the March 9 series clearly departs from the linear behaviour, as expected for multifractal intermittent series, but, surprisingly, the zeta function exhibits an almost linear relation with p in the case of January 25, despite the fact that both series have multifractal spectra with similar widths (see Fig. 2a). Thus, one should be cautious before using the behaviour of the scaling exponent as a definite measure of multifractality, although it is a good measure of intermittency. To confirm this result, Fig. 14(b) compares the zeta scaling exponents of the March 9 $|\boldsymbol{B}|$ series (red line with circles) with the zeta scaling exponents of its random phase series (magenta line with triangles). Since the random phase series has a Gaussian PDF, it removes from the original series the intermittent extreme events responsible for the fat-tailed PDF and the zeta scaling exponent becomes linear, following the K41 line. This result confirms the importance of the contribution from a

fat-tailed PDF to the multifractality of the March 9 series. In Fig. 14(c), the same analysis is done for the January 25 series, where both the original series and its random phases show an IK linear behaviour, since none of the series has a fat-tailed PDF, although they have multifractal spectra (see the blue and magenta spectra in Fig. 9a). We conclude from this that the ζ function is a good measure of multifractality due to PDF, but misses the contribution of long-range correlations to the multifractality.

6 *p*-MODEL

In Section 4, we showed that the multifractal spectra of the volatility of the solar wind are predominantly due to non-linear and linear correlations in the time series of January 25 and due to PDF and non-linear correlations for the March 9 time series. The presence of long-range non-linear correlations in both series is the signature of a non-linear dynamical system (possibly with some stochastic component) governing the behaviour of both series. In the present section, we employ the *p*-model (Halsey et al. 1986; Meneveau & Sreenivasan 1987) to show that both the correlations and the extreme events mentioned above are actually a consequence of turbulent energy-cascade processes with different scaling laws that depend on the presence or absence of current sheets in the original time series.

The *p*-model is a model for non-homogeneous energy-cascading process in the inertial range of fully developed turbulence based on the generalized Cantor set. Consider that the flux of kinetic energy from eddies of size L to smaller eddies is represented by a dissipation E_L. In the one-dimensional version of the *p*-model, L is the length of an interval. Suppose that an eddy of size L is unequally divided into two smaller eddies (i.e. two subintervals) of sizes $l_1 L$ and $l_2 L$, where $0 < l_1 < l_2 < 1$ are the size factors, with the energy flux E_L being distributed unto these subeddies with different probabilities p_1 and p_2; i.e. the new dissipation values are $p_1 E_L$ and $p_2 E_L$. In practice, one can start the process with $L = E_L = 1$. Then, each new eddy is further subdivided into two smaller eddies with the same size factors l_1 and l_2 and probabilities p_1 and p_2. This process may be repeated until the subintervals reach the Kolmogorov dissipation scale. At each cascading step n, there will be $\binom{n}{m}$ segments with length $l_1^m l_2^{n-m} L$ and dissipation $p_1^m p_2^{n-m} E_L$, for $m = 0, 1, \ldots, n$. As shown by Halsey et al. (1986) for the general two-scale Cantor set, it is possible to obtain the analytical expressions for the singularity exponent α and the singularity spectrum f as

$$\alpha = \frac{\ln p_1 + (n/m - 1) \ln p_2}{\ln l_1 + (n/m - 1) \ln l_2}, \tag{14}$$

$$f = \frac{(n/m - 1) \ln (n/m - 1) - (n/m) \ln (n/m)}{\ln l_1 + (n/m - 1) \ln l_2}. \tag{15}$$

For each n and given values of l_1, l_2, p_1, and p_2, the variation of m will provide the different values of α and f for the singularity spectrum. Since $0 \le m \le n$ and m is an integer, larger values of n provide a better definition of the spectrum. For a cascading process with direct energy dissipation in the inertial range, we have $p_1 + p_2 < 1$ (Meneveau & Sreenivasan 1987). This means that a new dp dissipation parameter must be included, where $dp = 1 - p_1 - p_2$. Thus, we define $p_2 = 1 - p_1 - dp$, as well as $l_2 = 1 - l_1$, in equations (14) and (15).

Fig. 15 shows the MF-DFA multifractal spectra for the volatility series of March 9 (red circles) and January 25 (blue diamonds). The *p*-model fits obtained from equations (14) and (15) are also shown (black line with dots). The values of p_1, dp, and l_1 were obtained with a Monte Carlo method that minimized the mean squared error between the original and fitted spectra. For March
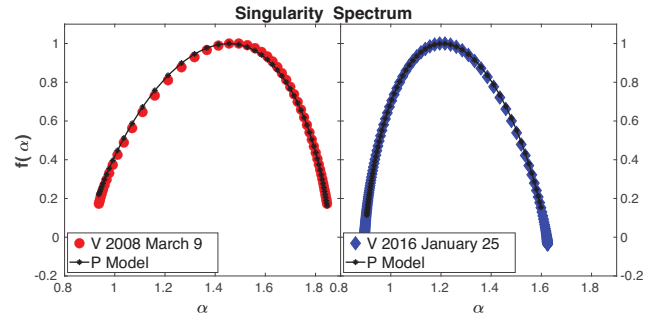
Figure 15. Left: Multifractal spectrum for the volatility of 2008 March 9 (red circle) and its *p*-model fit (black line with dots). Right: Multifractal spectrum for the volatility of 2016 January 25 (blue diamond) and its *p*-model fit (black line with dots).
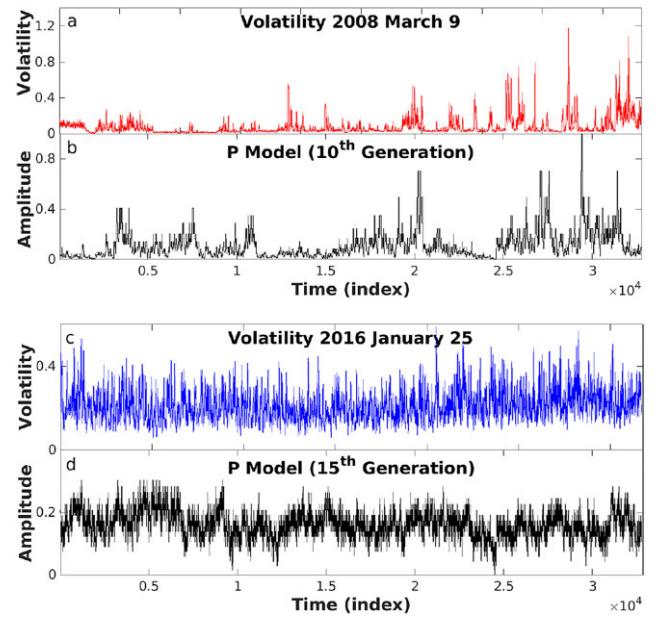
Figure 16. (a) Volatility time series for 2008 March 9 (red) and (b) generated *p*-model time series (black) by 10th interation. (c) Volatility time series for 2016 January 25 (blue) and (d) generated *p*-model time series (black) by 15th interation.

9, we obtained $p_1 = 0.71$, $dp = 0.17$, and $l_1 = 0.68$. For January 25, we obtained $p_1 = 0.51$, $dp = 0.11$, and $l_1 = 0.66$. The agreement between the observational and theoretical curves confirms that the solar wind multifractal spectra can be obtained from a turbulence cascade process. This is a remarkable result, since the *p*-model was specifically elaborated to represent turbulent cascade processes, and will usually not be able to approximate the spectra of other processes.

Next, we compare the turbulent time series behind the *p*-model spectra with the observational solar wind volatility time series in terms of their PSDs. To obtain the *p*-model PSDs, we use the probabilities and size factors previously obtained with the Monte Carlo method. By iterating the generalized two-scale Cantor set model, we produce two *p*-model time series. Fig. 16 shows a comparison of the solar wind volatility time series with the *p*-model time series. The two upper panels depict the solar wind series for March 9 (a) and the corresponding *p*-model (b); the two lower panels depict the solar wind series for January 25 (a) and the corresponding *p*-model (b). The qualitative similarity between observational and *p*-model time series is apparent in both cases.
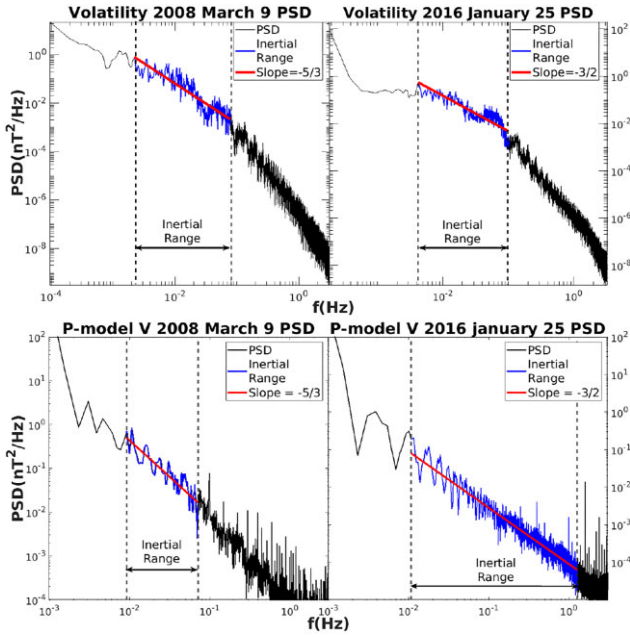
Figure 17. (a) Left: power spectral density for 2008 March 9 volatility. Right: power spectral density for 2016 January 25 volatility. (b) Left: power spectral density for generated *p*-model time series from 2008 March 9 volatility. Right: power spectral density for generated *p*-model time series from 2016 January 25 volatility. The blue regions mark the inertial range and the red lines are the linear fits for those intervals.

A comparison of observed and simulated PSDs is shown in Fig. 17. Fig. 17 (upper panels) shows the PSDs for the volatility time series of 2008 March 9 (left) and 2016 January 25 (right). The blue region between the vertical dashed lines represents the inertial range and the red line is the linear regression with a slope of $-5/3$ for the March 9 series and $-3/2$ for the January 25 series. Thus, the highly intermittent series of March 9 (with current sheets) exhibits a K41 scaling, whereas the January 25 series (without current sheets) shows an IK scaling. This fact had been previously established by Li et al. (2011) and confirmed by Gomes et al. (2019) using PSDs computed from the time series of $|\boldsymbol{B}|$. The PSDs computed from the *p*-model time series are shown in Fig. 17 (lower panels), and they reveal K41 scaling for the March 9 series and IK scaling for the January 25 series, just like in the original solar wind series. Note that in both cases the inertial range can be extended almost throughout the whole PSDs shown, since our *p*-model has small dissipation. We conclude that a K41 intermittent turbulence cascade is behind the multifractality of the current sheet-filled time series of March 9 and an IK turbulence cascade is the origin of the multifractality of the January 25 series. This result is consistent with other time series analysed by us, which show that current sheets are responsible for the K41 turbulence multifractality and the absence of current sheets results in an IK turbulence multifractality in the solar wind (see table 4 in Gomes et al. 2019).

7 CONCLUSIONS

We have presented a new methodology for multifractal analysis of solar wind magnetic field data, based on MF-DFA, volatility, and surrogate time series. The MF-DFA provides a standard way to generate the singularity spectrum and the Renyi exponent; the volatility enhances the extreme events, stressing the differences between series with current sheets and series without current sheets; the surrogate

time series provide a way to infer the origin of multifractality. Additionally, the *p*-model was used to reproduce the multifractal behaviour of the solar wind series, indicating that a non-linear turbulence energy-cascade dynamical system is behind the observed dynamics. A similar framework for multifractal analysis, but without the volatility and the *p*-model, was used by Chattopadhyay et al. (2018) in the analysis of CME linear speed data in the solar wind. In order to keep the paper reasonably short, we have limited our presentation to only two time series, but we have tested our techniques in other series and found that the conclusions presented are robust. An example of analysis with two other time series is included in the supplementary material (online). Further exploration of the methodology is left for future works.

Just like in Gomes et al. (2019), we found the volatility to be very useful to highlight the role of current sheets. In our case, they increase the signature of multifractality due to PDF in the singularity spectra. The surrogate analysis of both original and volatility series shows that for time series with current sheets, multifractality is due to both intermittency and non-linear correlations; for time series without current sheets, it is predominantly produced by the long-range correlations. The *p*-model analysis reveals that those are mainly non-linear correlations, since the process behind the statistics is a non-linear turbulent energy cascade. So, turbulence is the common source of the multifractality, but current sheets are the source of the left asymmetry of the singularity spectrum, as well as the non-linear scaling exponent for the structure functions. In the absence of current sheets, the small-amplitude fluctuations are the main source of the right asymmetry of the singularity spectrum. It is important to stress that despite being a multifractal process, the current sheet-free series exhibits an almost linear scaling exponent for the structure functions, which is sometimes confused with a monofractal process in the literature. Our results indicate that the Renyi exponent is more sensitive to multifractality due to correlations than the structure function scaling exponent (zeta function).

In dealing with separate cases where the presence or absence of current sheets is considered, we are attacking one of the 'nine outstanding questions of solar wind physics', related by Vaill & Borovsky (2020), namely the origin and evolution of the mesoscale (time-scales in the range of minutes up to a few hours) plasma and magnetic field structure of the solar wind. These current sheets have been associated with the border between adjacent flux tubes (Bruno 2019), while also being related to non-linear turbulent interactions rather than the presence of advected pre-existing flux-tube structures (Bowen et al. 2018). In this work, we do not focus on the origin of those coherent structures, but measure their weight on the statistics of solar wind fluctuations. We do this not only through Fourier spectral indices and the scaling of structure functions, as in Salem et al. (2009), but their contribution to multifractality is explored in depth through the MF-DFA, volatility, and surrogate techniques. As we said, our results reveal that although the scaling of the structure functions may be almost linear for series without current sheets, the singularity spectra may still display broad parabolas, the signature of highly multifractal signals. Thus, the scaling exponent of structure functions is adequate to measure multifractality due to PDFs, but not for multifractality due to long-range correlations, where the Renyi exponent and singularity spectra should be adopted. Multifractal series with nearly linear behaviour of the scaling exponents were also reported in Tam et al. (2010) (see their fig. 4), where the rank-order multifractal analysis is employed in the description of auroral zone electric field fluctuations.

In conclusion, the basic question related to mesoscale plasma turbulence in the solar wind is not whether it is monofractal or

multifractal, but whether the source of the ubiquitous multifractality is the PDF or the long-range correlations. The short answer is that in the presence of current sheets, the PDF has a strong contribution for multifractality, but in their absence, it is mainly due to correlations. It would be interesting to check whether the monoscaling of the structure functions reported in previous solar wind time series, as in Kiyani et al. (2009, 2013) and Bruno (2019) for turbulence at kinetic scales, indeed reveals monofractality or whether they indicate, in fact, multifractal series due to correlations and not due to intermittency.

DATA AVAILABILITY

The data used for this analysis can be obtained from European Space Agency (ESA) at the Cluster Science Archive: https://csa.esac.esa.int/csa-web/ (last access: 2020 December 2, ITA, 2020).

REFERENCES

Barrett J. P., 1974, Am. Stat., 28, 19
Barunik J., Aste T., Di Matteo T., Liu R., 2012, Physica A, 391, 4234
Bolzan M. J. A., Rosa R. R., 2012, Ann. Geophys., 30, 1107
Bowen T. A., Mallet A., Bonnell J. W., Bale S. D., 2018, ApJ, 865, 45
Bruno R., 2019, Earth Space Sci., 6, 656
Burlaga L. F., 2001, J. Geophys. Res., 106, 15917
Cantor G., 1883, Math. Ann., 21, 545
Carbone V., Lepreti F., Sorriso-Valvo L., Veltri P., Antoni V., Bruno R., 2004, Riv. Nuovo Cimento, 27, 1
Chang T., Tam S. W. Y., Wu C.-C., 2004, Phys. Plasmas, 11, 1287
Chattopadhyay A., Khondekar M. H., Bhattacharjee A. K., 2018, Chaos Solitons Fractals, 114, 542
de Freitas D. B. et al., 2016, ApJ, 831, 87
Dong Q., Wang Y., Li P., 2017, Environ. Pollut., 222, 444
Dutta S., Ghosh D., Chatterjee S., 2013, Frontiers Physiol., 4, 274
Eke A., Herman P., Kocsis L., Kozak L., 2002, Physiol. Meas., 23, 1
Frisch U., 1995, Turbulence: The Legacy of AN Kolmogorov. Cambridge Univ. Press, Cambridge
Gomes T. F. P., Rempel E. L., Ramos F. M., Silva S. S. A., Muñoz P. R., 2019, MNRAS, 490, 1879
Gopinath S., 2016, Ap&SS, 361, 290
Gos M., Baranowski P., Krzyszczak J., Kieliszek A., Siwek K., 2021, Int. J. Climatol., 41, E1531
Halsey T. C., Jensen M. H., Kadanoff L. P., Procaccia I., Shraiman B. I., 1986, Phys. Rev. A, 33, 1141
Hurst H., Black R., Simaika Y., 1965, Long-Term Storage: An Experimental Study. Constable, London
Ihlen E., 2012, Frontiers Physiol., 3, 141
Iroshnikov P., 1964, Sov. Astron., 7, 566
Kantelhardt J., Zschiegner S., Koscielny-Bunde E., Bunde A., Havlin S., Stanley E., 2002, Physica A, 316, 87

Kiran K., Ajithprasad1 K., Kumar V. A., Harikrishna K., 2021, Sol. Phys., 296, 23
Kiyani K. H., Chapman S. C., Khotyaintsev Y. V., Dunlop M. W., Sahraoui F., 2009, Phys. Rev. Lett., 103, 075006
Kiyani K. H., Chapman S. C., Sahraoui F., Hnat B., Fauvarque O., Khotyaintsev Y. V., 2013, ApJ, 763, 10
Kolmogorov A., 1941, Dokl. Akad. Nauk SSSR, 30, 301
Kraichnan R. H., 1965, Phys. Fluids, 8, 1385
Lancaster G., Iatsenko D., Pidde A., Ticcinelli V., Stefanovska A., 2018, Phys. Rep., 748, 1
Li G., 2008, ApJ, 672, L65
Li G., Miao L., Hu Q., Qin G., 2011, Phys. Rev. Lett., 106, 125001
Macek W. M., 2007, Nonlinear Process. Geophys., 14, 695
Madanchi A., Absalan M., Lohmann G., Anvari M., Reza Rahimi Tabar M., 2017, Sol. Energy, 144, 1
Maiwald T., Mammen E., Nandi S., Timmer J., 2008, Surrogate Data – A Qualitative and Quantitative Analysis. In: Dahlhaus R., Kurths J., Maass P., Timmer J. (eds), Mathematical Methods in Signal Processing and Digital Image Analysis. Understanding Complex Systems. Springer, Berlin, Heidelberg, doi:10.1007/978-3-540-75632-3_2
Marsch E., Tu C.-Y., 1998, Nonlinear Process. Geophys., 4, 101
Meneveau C., Sreenivasan K. R., 1987, Phys. Rev. Lett., 59, 1424
Neelakshi J., Rosa R. R., Savio S., Stephany S., de Meneses F. C., Kherani E. A., Muralikrishna P., 2022, Chaos Solitons Fractals, 156, 111808
Norouzzadeh P., Dullaert W., Rahmani B., 2007, Physica A, 380, 333
Ogunjo S. T., Rabiu A. B., Fuwape I. A., Obafaye A. A., 2021, J. Geophys. Res.: Space Phys., 126, e2020JA027873
Renyi A., 1976, Selected Papers of Alfred Renyi. Akademiai Kiado, Budapest
Salat H., Murcio R., Arcaute E., 2017, Physica A, 473, 467
Salem C., Mangeney A., Bale S. D., Veltri P., 2009, ApJ, 702, 537
Sarker A., Mali P., 2021, Chaos Solitons Fractals, 151, 111297
Shimizu Y., Thurner S., Ehrenberger K., 2002, Fractals, 10, 103
Tam S. W. Y., Chang T., Kintner P. M., Klatt E. M., 2010, Phys. Rev. E, 81, 036414
Theiler J., Eubank S., Longtin A., Galdrikian B., Doyne Farmer J., 1992, Physica D, 58, 77
Tsay R., 2010, Analysis of Financial Time Series. Wiley, New York
Vaill N. M., Borovsky J. E., 2020, JGR Space Phys., 125, e2018JA026005
Valdivia J. A., Rogan J., Muñoz V., Toledo B. A., Stepanova M., 2013, Adv. Space Res., 51, 1934
Wawrzaszek A., Echim M., Bruno R., 2019, ApJ, 876, 153
Wirsing K., Mili L., 2020, J. Appl. Geophys., 173, 103920
Wu L., Chen L., Ding Y., Zhao T., 2018, Physica A, 508, 824
Yang D., Zhang C., Liu Y., 2015, Soil Dyn. Earthq. Eng., 72, 12

SUPPORTING INFORMATION

Supplementary data are available at *MNRAS* online.

Figure S1. Solar wind time series of $|\boldsymbol{B}|$ (a) for 2009 February 24 (red), containing current sheets (black), and (b) for 2003 February 1 (blue), without current sheets.
Figure S2. Multifractal spectra of $|\boldsymbol{B}|$ for 2009 February 24 (red) and 2003 February 1 (blue).
Figure S3. Volatility of solar wind magnetic field time series for (a) 2009 February 24 (red) and (b) 2003 February 1 (blue).
Figure S4. Multifractal spectra for the volatility in 2009 February 24 (red) and 2003 February 1 (blue).
Figure S5. Multifractal spectra of $|\boldsymbol{B}|$ for 2009 February 24 (red) and the respective surrogates: shuffled (green) and random phases (magenta).
Figure S6. Multifractal spectra of $|\boldsymbol{B}|$ for 2003 February 1 (blue) and the respective surrogates: shuffled (green) and random phases (blue).

Figure S7. Multifractal spectra for the volatility of 2009 February 24 (red) and the respective surrogates: shuffled (green) and random phases (magenta).

Figure S8. Multifractal spectra for the volatility of 2003 February 1 (blue) and the respective surrogates: shuffled (green) and random phases (magenta).

Table S1. Width of α, $\Delta\alpha$, for magnetic field and volatilities of 2009 February 24 (CS) and 2003 February 1.

Table S2. Spectral asymmetry, *A*, for magnetic field and volatilities of 2009 February 24 (CS) and 2003 February 1.

Please note: Oxford University Press is not responsible for the content or functionality of any supporting materials supplied by the authors. Any queries (other than missing material) should be directed to the corresponding author for the article.

This paper has been typeset from a TeX/LaTeX file prepared by the author.

A.2 Supplementary Data: Origin of multifractality in solar wind turbulence: the role of current sheets

This annex contains supplementary data from the article originally published in the Monthly Notices of the Royal Astronomical Society journal.

Origin of Multifractality in Solar Wind Turbulence: the Role of Current Sheets Supplementary Material

November 22, 2022

1 Introduction

In order to confirm our results, in addition to the two time series analyzed in the paper, we show here the results for another pair of time series of solar wind magnetic field. We apply the same methodology described in the paper for the data of 2009 February 24 and 2003 February 1. The time series of February 24 is characterized by the presence of large-scale current sheets. Meanwhile, the time series for February 1 is characterized by the absence of current sheets.

Figure 1 shows the two new solar wind magnetic field time series, detected through the Fluxgate Magnetometer (FGM) onboard Cluster-1. The data have a length of 24 hours with a cadence of 22 Hz. Due to the high nonstationarity present in the two time series (the Hurst exponents are $h_{cs} = 1.277$ for February 24 and $h_{ncs} = 1.178$ for February 1), it was necessary to differentiate both of them before applying the MF-DFA method.
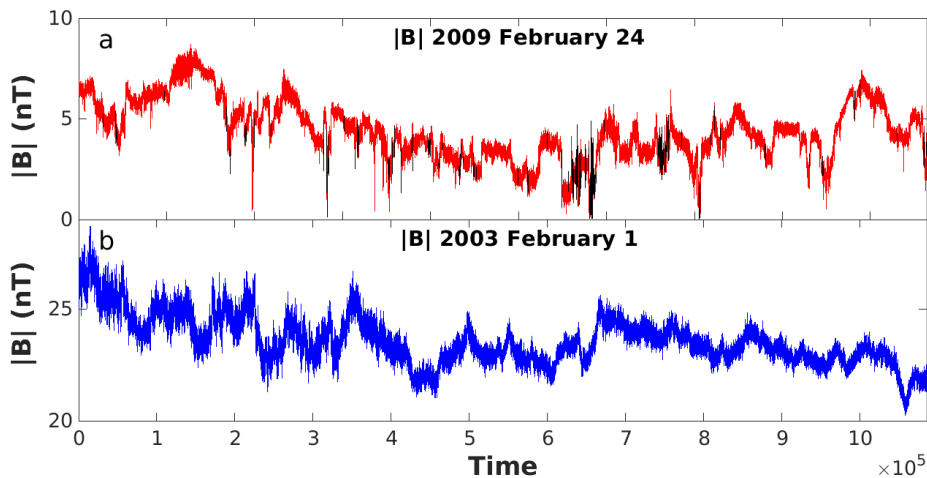

Figure 1: Solar wind time series of $|B|$ (a) for 2009 February 24 (red), containing current sheets (black) and (b) for 2003 February 1 (blue), without current sheets.

2 MF-DFA of the $|B|$ time series

Figure 2 shows the multifractal spectra for the time-differenced series of the two data sets shown in Fig. 1. Figure 2 evidence the left asymmetry for the multifractal spectrum of February 24 (with current sheets (**CS**)) (red), which indicates that multifractality is predominantly related to large-scale fluctuations. However, for February 1 (blue), a right asymmetry is observed, i.e., the multifractality is more related to the small-scale fluctuations. Now comparing the α width of both spectra, we can see a considerable difference between them ($\Delta\alpha_{cs} \approx 0.46$ for February 24(**CS**) and $\Delta\alpha_{ncs} \approx 0.35$ for February 1). Thus, the singularity spectrum is wider for the time series with current sheets.
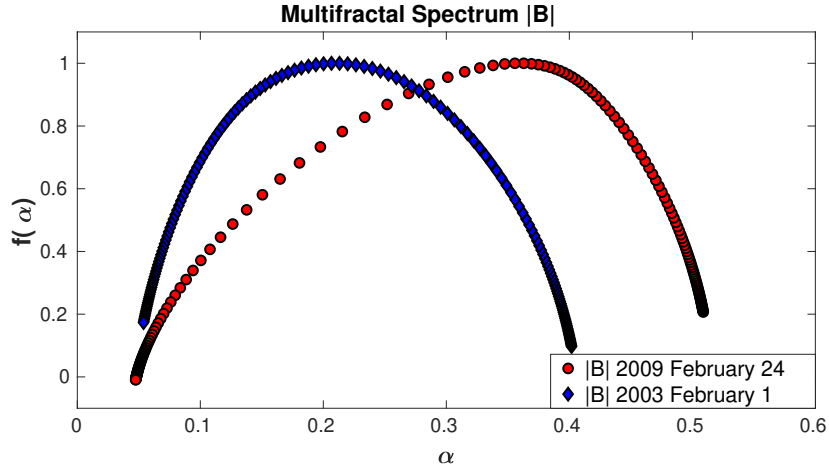
Figure 2: Multifractal spectra of $|B|$ for 2009 February 24 (red) and 2003 February 1 (blue).

3 MF-DFA of the Volatility time series

With the goal of enhancing the extreme events present in the series due to current sheets, we applied the volatility to the two data sets shown in Fig. 1. The results are depicted in Fig. 3. Figure 4 shows the corresponding multifractal spectra, with a significant difference of width between them. For February 24($\mathbf{CS}$), $\Delta\alpha_{cs} \approx 0.84$, while for February 1, $\Delta\alpha_{ncs} \approx 0.56$. Thus, the volatility has enhanced the difference between the spectra and highlighted the role of current sheets in multifractality.
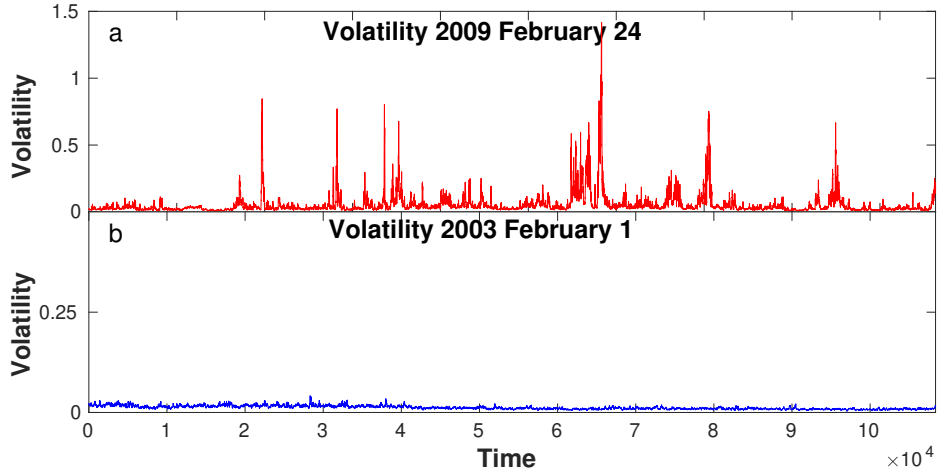

Figure 3: Volatility of solar wind magnetic field time series for (a) 2009 February 24 (red), and (b) 2003 February 1 (blue).
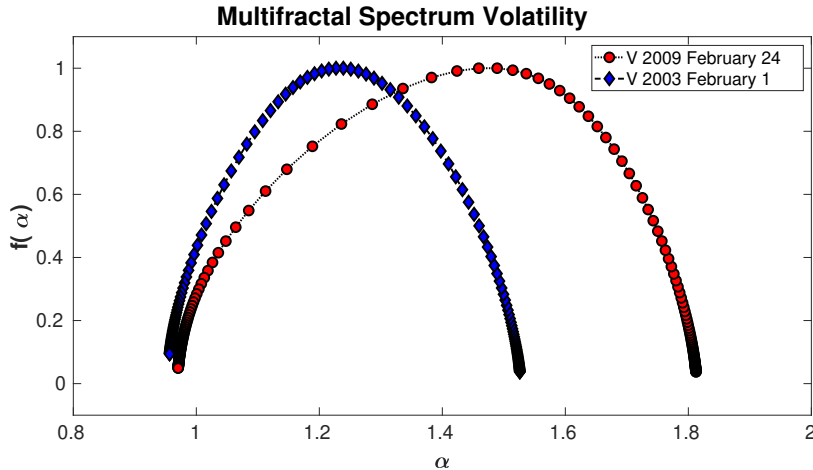
Figure 4: Multifractal spectra for the volatility in 2009 February 24 (red), and 2003 February 1 (blue).

4 MF-DFA OF SURROGATE TIME SERIES

In order to identify the origin of the multifractal behavior, we have applied the *surrogate method* for all $|B|$ and volatility time series. After obtaining the *shuffled* and the *random phases* time series for each data set we computed the multifractal spectra.

Figure 5 shows the multifractal spectra for February 24(**CS**) and its surrogates. Both surrogate spectra have a significant width reduction when compared with the original. However, the random phases multifractal spectrum has a stronger reduction. This behavior confirms the idea of a larger contribution of the PDF to this multifractal process, as a consequence of the current sheets.

Now, looking at the multifractal spectra of the solar wind magnetic field without current sheets (Fig. 6), we see a different behavior. Even though there is a width reduction in both surrogates spectra, we observe a larger decrease in the shuffled spectrum. That is, the contribution from long-range correlations to multifractality is more dominant in the time series without current sheets. This result is consistent with what is proposed in the main paper.
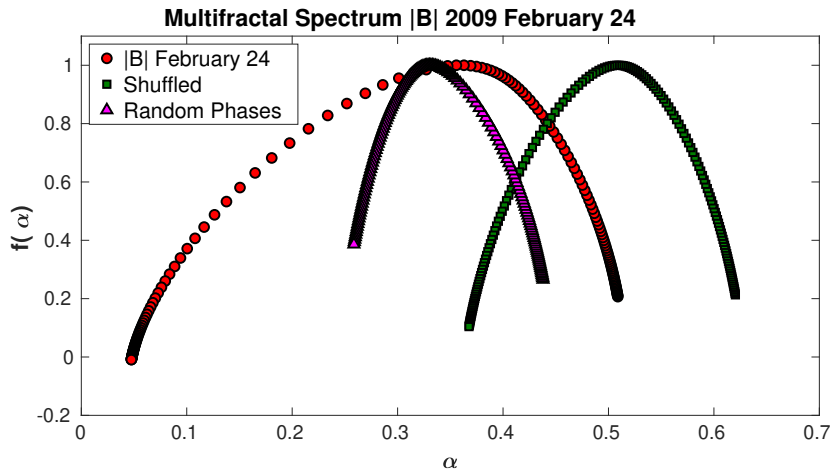

Figure 5: Multifractal spectra of $|B|$ for 2009 February 24 (red) and the respective surrogates: shuffled (green), and random phases (magenta).

As was done with the paper examples, we also applied the surrogate method to the volatility time series. As expected, the same general behavior is observed in the multifractal spectra.

Figure 7 confirms a major influence of extreme events to multifractality for February 24(**CS**), since $\Delta\alpha$ of the random phases surrogate has a smaller value than the one from the shuffled surrogate. Figure 8 exhibits the singularity spectra for the volatility time series of February 1. Unsurprisingly, these spectra also follow the same general behavior as the corresponding spectra obtained from the $|B|$ time series. As expected, the results from Fig.8 highlight the long-range correlations influence on the multifractality of the volatility time series.
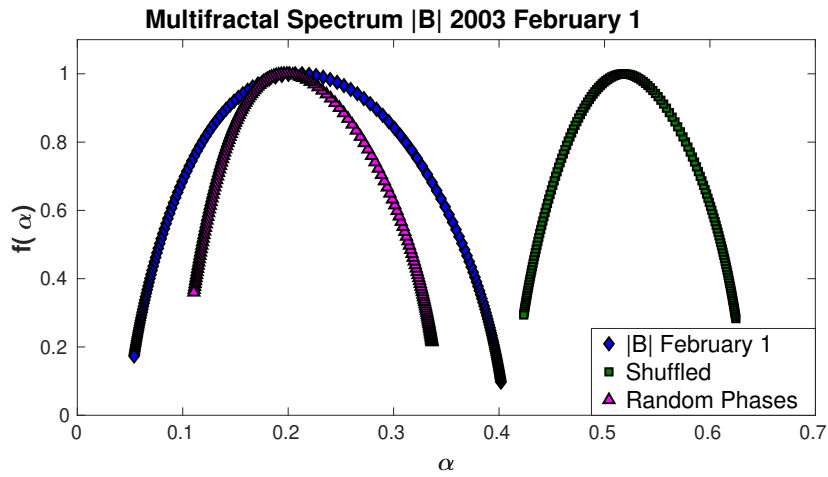
Figure 6: Multifractal spectra of $|B|$ for 2003 February 1 (blue) and the respective surrogates: shuffled (green), and random phases (blue).

Figure 7: Multifractal spectra for the volatility of 2009 February 24 (red) and the respective surrogates: shuffled (green), and random phases (magenta).
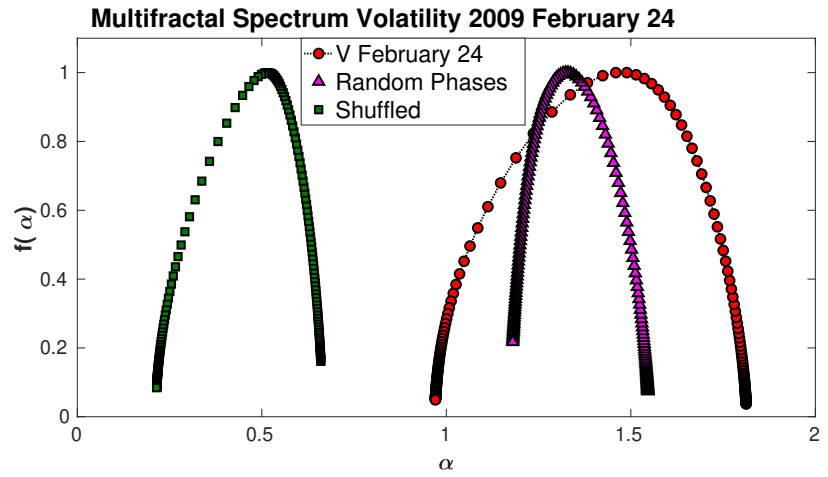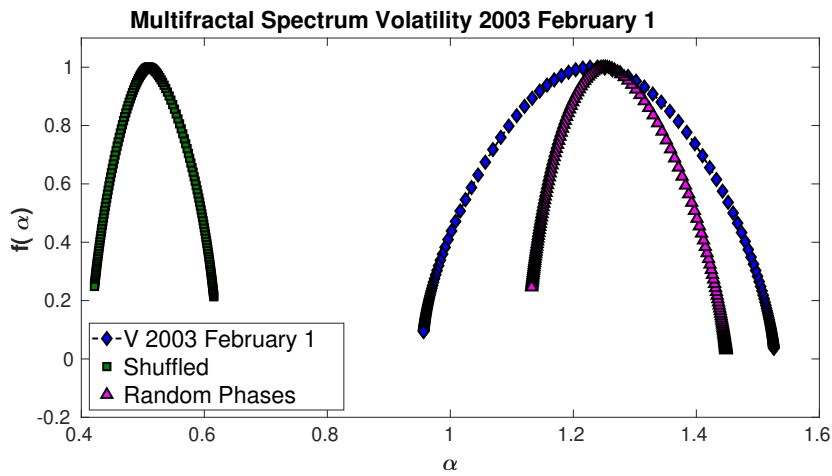

Figure 8: Multifractal spectra for the volatility of 2003 February 1 (blue) and the respective surrogates: shuffled (green), and random phases (magenta).

A summary of all values provided by the multifractal analysis can be found on Tables 1 and 2. Table 1 shows the variation of the α width, $\Delta\alpha$, while Table 2 emphasizes the spectral asymmetry.

Table 1: Width of α, $\Delta\alpha$, for magnetic field and volatilities of 2009 February 24 (**CS**) and 2003 February 1.

	February 24 (**CS**)		February 1	
	$|B|$	Volatility	$|B|$	Volatility
Original	0.4614	0.84202	0.3480	0.5695
Shuffle	0.2527	0.44506	0.20122	0.1941
Random Phases	0.17934	0.36611	0.2260	0.3161

Table 2: Spectral asymmetry, A, for magnetic field and volatilities of 2009 February 24 (**CS**) and 2003 February 1.

	February 24 (**CS**)		February 1	
	$|B|$	Volatility	$|B|$	Volatility
Original	0.4626	0.62344	1.18403	1.0156
Shuffle	0.7764	0.47176	1.1017	1.1842
Random Phases	1.4568	1.44489	1.5630	1.6386

In summary, in order to reinforce the conclusions of the main work we have applied the *MF-DFA method* on two new solar wind magnetic field time series. The new findings of this supplementary material confirm our theoretical conclusions described in the paper. In other words, the presence of current sheets indeed impacts the turbulent process of the solar wind and is responsible for the increase of multifractality due to PDFs. In the absence of current sheets, multifractality is mainly due to nonlinear correlations.

FOLHA DE REGISTRO DO DOCUMENTO

1. CLASSIFICAÇÃO/TIPO	2. DATA	3. REGISTRO N°	4. N° DE PÁGINAS
TD	08 de agosto de 2023	DCTA/ITA/TD-033/2023	118

5. TÍTULO E SUBTÍTULO:

Multifractal analysis of magnetic fields in the solar wind and solar photosphere.

6. AUTOR(ES):

Leonardo Fabrício Gomes Batista

7. INSTITUIÇÃO(ÕES)/ÓRGÃO(S) INTERNO(S)/DIVISÃO(ÕES):

Instituto Tecnológico de Aeronáutica – ITA

8. PALAVRAS-CHAVE SUGERIDAS PELO AUTOR:

Vento Solar; Região Ativa; Turbulência; Lâmina de Corrente; Séries Temporais; Detecção de Vórtices; Análise Multifractal; MFDFA; MFDMA; p-model; Fractais; Atmosfera Solar; Sistemas Dinâmicos; Estatística; Física.

9.PALAVRAS-CHAVE RESULTANTES DE INDEXAÇÃO:

Magnetohidrodinâmica; Campos magnéticos; Vento solar; Turbulência; Análise de séries temporais; Fractal; Atmosfera solar; Sistemas dinâmicos; Física.

10. APRESENTAÇÃO: **X Nacional   Internacional**

ITA, São José dos Campos. Curso de Doutorado. Programa de Pós-Graduação em Física. Área de Dinâmica Não-Linear e Sistemas Complexos. Orientador: Prof. Dr. Erico Luiz Rempel. Defesa em 13/07/2023. Publicada em 2023.

11. RESUMO:

In this work, we investigate the role of coherent structures in solar wind and solar photospheric turbulence through the multifractal perspective. By using the multifractal detrended fluctuation analysis method coupled with the volatility of the time series, two solar wind magnetic field time series are investigated, one with current sheets and one without current sheets. As expected, a stronger level of multifractality is found in the volatility of the series containing currents sheets when compared to the one without current sheets. To know the origin of the multifractal behavior, the surrogate method is applied to all time series. The results for the magnetic field time series reveal a major contribution from a heavy-tail distribution to the multifractality of the series with currents sheets but a stronger influence of long-range correlations for the series without current sheets. In the context of the photosphere, we propose a new multifractal analysis methodology for intense active regions. The results confirm the rise of multifractality following the growth and evolution of the active region. In addition, Lagrangian objective vortices were also detected at the photosphere, which are directly related to twisting and energy injection in the magnetic field, leading to intense solar flares.

12. GRAU DE SIGILO:

(X) OSTENSIVO   ( ) RESERVADO   ( ) SECRETO